

HOW WELL IS THE LINEAR
DISPERSION RELATION SATISFIED
FOR LABORATORY WAVES?

BY

TORE MAGNUS ARNESEN TAKLO

THESIS
for the degree of
MASTER OF SCIENCE

(Master in Applied Mathematics and Mechanics; Fluid Mechanics)



Faculty of Mathematics and Natural Sciences
University of Oslo

May 2012

Det matematisk- naturvitenskapelige fakultet
Universitetet i Oslo

HOW WELL IS THE LINEAR
DISPERSION RELATION SATISFIED
FOR LABORATORY WAVES?

by

Tore Magnus Arnesen Taklo

Abstract

The master thesis presents various (k, ω) -spectra which shows measured dispersion relations derived from various measured laboratory irregular long-crested wave fields. The measured dispersion relations are presented and compared with the linear dispersion relation and higher order dispersion shells. The experimental work includes the surface elevation and the current. Numerical simulations by Krogstad and Trulsen (2010) of the dynamic nonlinear evolution of unidirectional long-crested free waves using the nonlinear Schrödinger equation and its generalizations suggest that components above the spectral peak can have larger phase and group velocities than anticipated by linear theory. Moreover it has been suggested that the spectrum does not maintain a thin well-defined dispersion surface but rather develops into a continuous distribution in (k, ω) -space. The main purpose of the experimental work in the thesis has been to design high-resolution spatiotemporal laboratory measurements to investigate the above peak behaviour suggested from the numerical simulations. Moreover, underlying purposes has been to validate the linear dispersion relation and higher order dispersion shells and to fill the gap between unidirectional numerical simulations and low-resolution field data. The experimental results show that the spectrum does not maintain a thin well-defined surface. Close to the spectral peak the propagation of free waves has been validated to satisfy the linear dispersion relation. Spectral distributions caused by second and third order bounded waves have been identified. Moreover, it has only partly been validated that components above the spectral peak can have larger phase and group velocities than anticipated by linear theory, the main reason probably being caused by that the simultaneous coverage in space applied in the experiments is too short to allow significant dynamic nonlinear evolution.

Acknowledgement

First of all I would like to thank my main supervisor professor Karsten Trulsen for always being helpful with and enthusiastic about the thesis. With your supervising it has been interesting and challenging to work with the complicated nature of water surface elevation. Your supervising has been very gainful and I have been privileged to have a main supervisor who has motivated and showed interest and responsibility for the work. Thank you also for presenting the laboratory results for the scientific community at the EGU 2012 conference in Vienna.

I would like to thank my laboratory supervisor professor Atle Jensen who despite being a long way from Norway this year at the Cornell University in USA, has answered long e-mails and ordered excellent and expensive equipment for the laboratory work. Your presentation of the Hydrodynamic laboratory, in connection with a introduction course in fluid mechanics in the fourth semester of my Bachelors' degree, invoked an interest in me for water surface waves which led to a later project work in the laboratory.

I would like to thank the recently retired laboratory engineer Svein Vesterby for helping me with building modules for the array. I very much appreciate that you took your time to come to the laboratory and help me with the array installation. I would like to thank PhD student Jostein Kolås for always being helpful with technical problems in the laboratory. You helped me with a long sequence of problems of different kinds. A thank also goes to associate professor at the Universidad de Alcalá, Madrid, José Carlos Nieto Borge, who being my third supervisor has given me inspiration for the work.

I would like to thank my mother, Ingunn Arnesen, my stepfather Aksel Farstad, my father Terje Taklo and my stepmother Solveig Opsal who have encouraged me to continue with academic studies. I also like to thank the rest of my family.

I would very much like to thank my beloved Marije Rixt Bakker and her family in the Netherlands. You have supported and encouraged me with the work.

Oslo, Norway, May 2012

Tore Magnus Arnesen Taklo

Contents

1	Introduction	3
2	Theoretical framework	7
2.1	Linear wave theory	7
2.2	Nonlinearity	10
3	Experimental arrangements	12
3.1	Early stage experimental arrangement	12
3.2	Synthetic array design	14
3.3	Later stage experimental arrangement	15
4	Method of analysis	18
4.1	Discrete Fourier transform	18
5	Surface elevation	22
5.1	Interpolation	22
5.2	Filter	25
5.3	Startup effects	26
5.4	Repeatability	26
5.4.1	With absorbing beach	26
5.4.2	With reflecting wall	29
5.5	Time tapering	32
5.6	Space tapering	33
5.7	Frequency and wavenumber spectra	35
5.7.1	Frequency spectra	35
5.7.2	Bandwidth	36
5.7.3	Wavenumber spectra	38
5.8	Steepness	39
5.9	Sampling	40
6	Current	42
6.1	With absorbing beach	43
6.2	With reflecting wall	45
7	Measured dispersion relations	49
7.1	With absorbing beach	49
7.1.1	$L = 1.2$ m and $M = 24$	49
7.1.2	$L = 4.8$ m and $M = 96$	52
7.1.3	$L = 9.6$ m and $M = 192$	55
7.1.4	$L = 19.2$ m and $M = 128$	57
7.1.5	$L = 19.2$ m and $M = 256$	58
7.2	With reflecting beach and end wall	61
7.2.1	$L = 4.8$ m and $M = 96$	61
7.2.2	$L = 19.2$ m and $M = 256$	65
8	Numerical model	68
8.1	First order numerical model	68
8.2	Errors in Δx	69
9	Conclusion	73
9.1	Conclusions and discussions	73
9.2	Suggestions for further work	75

10	References	77
11	Appendix	79
A	Theoretical framework	79
A.1	Linear wave theory	79
A.1.1	Obtaining c_1 , c_2 , $f(z)$ and ϕ	79
A.1.2	Obtaining the linear dispersion relation equation	80
B	Experimental arrangements	80
B.1	Early stage experimental arrangement	80
B.1.1	Modification of original input files	80
B.1.2	Calibration	81
C	Method of analysis	82
C.1	Discrete Fourier transform	82
C.1.1	Obtaining the DFT $\hat{\eta}$	82
D	Surface elevation	83
D.1	Frequency spectra from series 1-6 on $h = 0.35$ m	83
D.2	Bandwidths from series 1-6 on $h = 0.35$ m	86
E	The measured dispersion relations	87
E.1	$L = 1.2$ m and $M = 24$	87
E.1.1	(k, ω) -spectra measured from series 2-6	87
E.1.2	The effect of space tapering in the (k, ω) -spectra	90
E.2	$L = 4.8$ m and $M = 96$	93
E.2.1	The entire (k, ω) -domain	93
E.2.2	The effect of time tapering in the (k, ω) -spectra	95
E.2.3	The effect of space tapering in the (k, ω) -spectra	96
E.3	$L = 19.2$ m and $M = 256$	99
E.3.1	The effect of a strong filter	99

1 Introduction

Linear wave theory is the leading order mathematical model for freely propagating water surface waves and for more than fifty years it has been a cornerstone in the development of ocean engineering, see (Newman 1977), (Goda 2000) and (Tucker and Pitt 2001) and the references therein. Linear wave theory assumes that the water surface is a random linear superposition of non-interacting regular waves and introduces the linear dispersion relation connecting wave angular frequencies (ω) and wavenumber vectors (\mathbf{k}), expressed in term of the wavelengths (λ). The linear dispersion relation is a widely used model for water surface wave propagation and in particular it shows that water surface waves on deep water are dispersive and propagate with wave phase speeds (c) proportional to the square root of the wavelengths (λ).

By considering straightforward perturbation expansions of the surface elevation, bound harmonics are added to the linear field. The bound harmonics are caused by bounded waves and the higher harmonic bounded waves are bounded to the freely propagating waves with integer multiple frequency and wavenumber components of the free waves.

The bound harmonics are referred to as static nonlinearities and leads to reconstruction of the freely propagating waves. The most prominent of the bounded wave interactions is the second order difference which appears below the spectral peak. The second order difference leads to significant reconstruction of the freely propagating waves in the form of a peaked crest and a flattened trough. The higher harmonics above the spectral peak contribute to smaller reconstructions of the crests and the troughs. For offshore engineering it has been of interest to determine higher harmonic wave forces and the effect of resonant build-up, Huseby and Grue (2000), and in ocean engineering the second order theory has become routine and even essential for many applications, Forristall (2000).

Nevertheless, it is well-known since the pioneering work of Tick (1959), Phillips (1960, 1961), Longuet-Higgins (1963), Hasselmann (1962, 1963a, 1963b) and Hasselmann et al. (1973) during the fifties, sixties and seventies that dynamic nonlinearities in the form of energy transfer between propagating waves in wave groups appear, which dissociate from the static nonlinearities. The first dynamic nonlinear correction to the linear spectrum was calculated by Tick (1959), and Phillips (1960, 1961) introduced the resonant quartet interaction theory which later was used by Hasselmann (1962, 1963a,b) and Hasselmann et al. (1973) to estimate the dynamic nonlinear energy transfer between spectral wave components.

During the seventies, the applicability of the linear dispersion relation was questioned and in the late seventies Lake and Yuen (1978) proposed a model for a single nonlinear wave train with a carrier frequency equal to the dominant frequency in the spectrum. Lake and Yuen (1978) also proposed that the most appropriate model for describing the dynamics of the dominant wave envelope, would be to use the nonlinear Schrödinger equation as a basis, with reference to Zakharov (1968) who derived the appropriate nonlinear Schrödinger equation for the complex wave envelope. Results from laboratory experiments performed by the authors and Ramamonjjarisoa and Coantic (1976) supported evidence for the applicability of the model. It was reported that spectral components above the spectral peak had phase velocities close to that of the spectral peak and it was suggested that the energy was essentially propagating with the group velocity of the spectral peak.

A striking result from the laboratory observations, based on the correlation between pairs of wave staffs, by Lake and Yuen (1978) and Ramamonjjarisoa and Coantic (1976), was that the apparent phase speed of wave components above the spectral peak were nearly independent of frequency and thus appeared to be non-dispersive. These results were quite curious and inconsistent with linear wave the-

ory. Later in the beginning of the eighties Phillips (1981), in cooperation with the authors, explained the results as a consequence of dispersion of short waves in the presence of longer waves. The results of the work showed that short waves are distorted and convected by dominant long waves, but they continue to propagate at phase speeds that depends on their own intrinsic frequencies and on their location with respect to the dominant wave if the dominant wave is short of breaking. It was suggested that dominant wave breaking could suppress the propagation of the shorter waves. It was also suggested that filtered signals would be strongly dominated by the conditions at the long-wave crests, and that capillary blockage at very high frequencies under strong wind forcing could suppress freely travelling capillary-gravity waves even without breaking. The sum of these effects implied that waves generated under such conditions could be much less dispersive. Later also Barrick (1986) explained the claim by Phillips (1981) from a somewhat different perspective by invoking known results from perturbation theory.

Numerical simulations by Krogstad and Trulsen (2010) of the cubic nonlinear Schrödinger equation (NLS) and the Dysthe (1979) or modified nonlinear Schrödinger equation (MNLS) suggested that components above the spectral peak could have larger phase and group velocities than anticipated by linear theory. Moreover, it was also suggested that the spectrum did not maintain a thin well-defined dispersion surface but rather developed into a continuous distribution in (k, ω) -space. The dynamic nonlinearity is contained in the (M)NLS evolution equations and in the numerical simulations Krogstad and Trulsen accounted for the dispersion of Phillips (1981), the bound harmonics of Barrick (1986) in addition to a classical nonlinear Stokes amplitude correction (Tucker and Pitt 2001). The numerical wave field evolved over a rather long propagation distance of 140 peak wavelengths.

High-resolution spatiotemporal measurements suitable for validation of the linear dispersion relation are rarely available. In the late seventies experiments in a wind-wave flume were carried out by Mitsuyasu et al. (1979) and interpreted in terms of a weakly nonlinear theoretical model developed by Masuda et al. (1979). The theoretical model also proposed a method for separating the spectra of free and bounded waves from the measured spectrum. For the experiments a linear array of twelve equispaced resistance-type wave gauges were used to measure the wind induced surface elevation. Among the experimental findings were components near the spectral peak satisfying linear theory. It was also reported about enhanced energies from spectral components at twice the spectral peak caused by second order bounded waves.

In the mid-eighties Donelan et al. (1985) published an extensive study of (\mathbf{k}, ω) -spectra both from field data from Lake Ontario and from a 80 m long laboratory wave flume. Both in the field and in the laboratory study an array of fourteen capacitance-type wave staffs in the form of a cross was used to measure the surface elevation. Under conditions of strong wind forcing in the laboratory their findings were significant effects on the phase velocity caused by amplitude dispersion and the presence of bound harmonics. Under natural wind conditions the field observations showed amplitude related dispersions, but bound harmonics were too weak to be detected from the field data.

Recent published papers of field studies related to wave dispersion are found in Hara and Karachintsev (2003) and Wang and Hwang (2004). Hara and Karachintsev (2003) examined how static nonlinearity and directionality influenced the frequency spectrum of a growing wave field under increasing wind forcing. As the wind forcing increased their findings were enhanced contributions from bounded waves in the frequency spectra. The field observations were taken from a moored spar buoy outside the coast of California. The surface elevation was measured with three wave staffs placed 1 m apart and the wave staffs were composed of 10 m long capacitance wave gauges.

Wang and Hwang (2004) examined the dispersion relation of short wind waves. A linear wave gauge array configured from a set of 20 capacitance wires was used in the field measurements. The array was mounted on a free drifting buoy deployed at two different field sites, in St. Andrews bay, Florida, well sheltered from long waves by a barrier island and in the Gulf of Mexico. Similar to our work, Wang and Hwang derived two-dimensional wavenumber-frequency spectra from the space-time recordings. The low-resolution spectra revealed main contributions near the linear wave dispersion manifold and effects from higher harmonics were reported. Both wavenumber-based and frequency-based phase speeds, $c(k)$ and $c(\omega)$, were extracted from the spectra, showing that the effect of higher harmonics revealed in the two-dimensional spectra was most prominent on the frequency-based phase speeds $c(\omega)$.

The data collected from field measurements are often characterized by relatively low spatial resolution and on field scale, conducting high-resolution spatiotemporal measurements are limited by the spatial extension and economic cost such recordings would require. The imaging of the ocean surface with X-band marine radar does provide the desired spatiotemporal coverage, but the interpretation of the radar images currently depends on the linear dispersion relation as a prerequisite, Nieto Borge et al. (2004). For example is the linear dispersion relation used to estimate the surface current by means of a least square fit using the linear dispersion equation with current advection, Nieto Borge et al. (2008). The main part of the analysis of X-band radar imagery consists of applying a 3D band-pass filter keeping only those (k, ω) -components that belong to the imaged wave field. Thus, high-resolution spatiotemporal measurements could open for a better identification of the location and behavior of these spectral contributions.

An important step towards achieving real time deterministic wave prediction has been the recent advances in the inversion of X-band nautical radar imagery into real ocean surface elevation. However, as mentioned, the inversion of the radar imagery currently relies on linear wave theory as a prerequisite.

Attention to nonlinear effects can substantially improve the performance of X-band nautical radars and improve the quality of real time wave prediction. Real time wave prediction over time intervals of the order of seconds to minutes opens up for a range of possible applications. Examples are avoidance against extreme waves and dangerous wave groups causing enormous forces and leading to critical situations or even loss of ship, cargo and crew, Clauss et al. (2008). Once a dangerous wave group is identified, one approach to avoid dangerous situations is to adjust heading and cruise speed.

Wave prediction could lead to improvement of weather sensitive and costly offshore operations. This applies to dynamic positioning in float-over-installations, lifting operations, oil and gas loading operations and helicopter take-off and landing on ship deck, to mention a few.

Another interesting application is alternative energy, where wave prediction could lead to enhanced extraction of power from floating wind turbines and real time latching control of wave energy devices, Barbarit and Clément (2006).

On laboratory scale high-resolution spatiotemporal measurements are less costly and easy to conduct and could give valuable information about wave dispersion and fill the gap between field data and unidirectional numerical simulations. When a laboratory wave field is long-crested and unidirectional information about dispersive properties is relatively easily achieved from a linear array and a 2D FFT routine. If a laboratory wave field is directional and short-crested, as is always the case in the ocean, the dispersion relation need to be derived from an array design which measures directionality and by applying a 3D FFT routine. If a wave field propagate in a range of different directions, high-resolution spatial measurements are complicated to achieve. To create dispersion models for directional and short-crested wave fields,

and multiple wave fields interacting from different directions, is probably one of the biggest challenges in the development of ocean water surface wave prediction in the future.

The main purpose of the experimental work in the thesis has been to design high-resolution spatiotemporal measurements and to derive spectra of measured dispersion relations to investigate more precisely how spectral components are distributed in the spectra both in comparison to the linear dispersion relation and static and dynamic nonlinear effects. As in the numerical simulations by Krogstad and Trulsen (2010) the wave fields are long-crested and unidirectional when an absorbing beach is used at the far end of the wave flume. A central part of the work has been the design of linear equispaced synthetic arrays which allows the surface elevation to be measured with higher spatial resolutions. Our findings so far have only partly validated the suggestion from the numerical simulations that spectral components above the peak can have larger phase and group velocities than anticipated by linear theory. This could be caused by that the laboratory wave field evolves over a relatively shorter propagation distance compared to the numerical simulations. The sampled propagation length in the laboratory covers only about 14 peak wavelengths and thus only 10% of the sampled propagation length in the numerical simulations. The propagation distance for the wave field in the laboratory could therefore be too short to allow significant dynamic nonlinear evolution.

The main focus of the work in the thesis has been to derive various spectra for the measured dispersion relations. In chapter 2, a brief presentation of the theoretical framework for linear wave theory and the static and dynamic nonlinearity is given. The experimental arrangement is presented already in chapter 3 such that the synthetic measurement techniques are easier to associate with the method of analysis of the surface elevation in the following chapter 4. A presentation of signal processing issues related to the surface elevation data, tapering to prevent spectral leakage caused by the finite extension of the space and time series and frequency and wavenumber spectra is given in chapter 5. The wave-induced current is presented in chapter 6. In chapter 7 a relatively extensive presentation of the main result in the thesis, the measured dispersion relations, is given. A leading order numerical model was developed to simulate some of the small suspected measurement errors in the experiments. The model and the results are presented in chapter 8. Topics which were evaluated to be rather lengthy to include in the mentioned chapters are presented in the Appendix. These include detailed mathematical derivations, quantitative presentations of the frequency spectra and the effect of developed tapering functions and other information regarding signal processing issues.

2 Theoretical framework

This chapter presents the theoretical framework which is applied to compare with the experimental results. The chapter is divided into two sections. In the first section linear wave theory and the linear dispersion relation is presented. Detailed derivations are given in Appendix A.1. In the second section, a brief presentation of the most fundamental properties of nonlinear waves and a abstract of some of the results from Krogstad and Trulsen (2010) is given.

2.1 Linear wave theory

The governing equations for the velocity potential $\phi(\mathbf{r}, z, t)$ and the surface displacement $\eta(\mathbf{r}, t)$ of an incompressible, inviscid, irrotational fluid with uniform depth h are, the Laplace equation,

$$\nabla^2 \phi = 0 \quad \text{for} \quad -h < z < \eta, \quad (1)$$

the kinematic boundary condition at the free surface,

$$\frac{\partial \eta}{\partial t} + \nabla \phi \cdot \nabla \eta = \frac{\partial \phi}{\partial z} \quad \text{at} \quad z = \eta, \quad (2)$$

the dynamic boundary condition at the free surface,

$$\frac{\partial \phi}{\partial t} + g\eta + \frac{1}{2}(\nabla \phi)^2 = 0 \quad \text{at} \quad z = \eta \quad (3)$$

and the kinematic boundary condition at the bottom,

$$\frac{\partial \phi}{\partial z} = 0 \quad \text{at} \quad z = -h, \quad (4)$$

where g is the acceleration of gravity, the horizontal position vector is $\mathbf{r} = (x, y)$, the vertical coordinate is z , $\nabla = (\partial/\partial x, \partial/\partial y, \partial/\partial z)$, and t is time. Surface tension is neglected. The linearization of the equations (1)-(4) is,

$$\nabla^2 \phi = 0 \quad \text{for} \quad -h < z < 0, \quad (5)$$

$$\frac{\partial \eta}{\partial t} = \frac{\partial \phi}{\partial z} \quad \text{at} \quad z = 0, \quad (6)$$

$$\frac{\partial \phi}{\partial t} + g\eta = 0 \quad \text{at} \quad z = 0, \quad (7)$$

$$\frac{\partial \phi}{\partial z} = 0 \quad \text{at} \quad z = -h, \quad (8)$$

Kundu and Cohen (2008). The solution of the linearized equations (5)-(8) is a linear superposition of simple harmonic regular waves such as

$$\eta(\mathbf{r}, t) = a \cos(\mathbf{k} \cdot \mathbf{r} - \omega t) \quad (9)$$

$$\phi(\mathbf{r}, z, t) = \frac{a\omega}{k} \frac{\cosh k(z+h)}{\sinh kh} \sin(\mathbf{k} \cdot \mathbf{r} - \omega t). \quad (10)$$

where a is the amplitude, $\omega = 2\pi/T$ is the angular frequency and T is the period. $\mathbf{k} = (k_x, k_y)$ is the wavenumber vector and $|\mathbf{k}| = \sqrt{k_x^2 + k_y^2}$ is the wavenumber.

For waves which propagate along the x -direction only, we define $|\mathbf{k}| = \sqrt{k_x^2 + k_y^2} = k = 2\pi/\lambda$, where λ is the wavelength, and the solutions to the linear equations can be written on the form,

$$\eta(x, t) = a \cos(kx - \omega t) \quad (11)$$

$$\phi(x, z, t) = \frac{a\omega}{k} \frac{\cosh k(z+h)}{\sinh kh} \sin(kx - \omega t). \quad (12)$$

Appendix A.1.1 shows how the velocity potential in equation 12 is obtained by solving the boundary value problem of the linearized equations (5) - (8).

The linear dispersion relation,

$$\omega^2 = gk \tanh kh, \quad (13)$$

is obtained by substituting the velocity potential (12) and the monochromatic wave solution (11) into the linearized dynamic boundary condition (7), see Appendix A.1.2. With current advection,

$$(\omega - uk)^2 = gk \tanh kh \quad (14)$$

where u is the x component of the current velocity $\mathbf{U} = (u, v, w)$.

The phase plane of the waves moves with the speed,

$$c = \frac{\omega}{k} = \frac{2\pi/T}{2\pi/\lambda} = \frac{\lambda}{T} \quad (15)$$

in surface normal direction, and c is therefore called the phase speed. By substituting $\omega = ck$ into the linear dispersion relation (13) we find the phase speed,

$$c = \sqrt{\frac{g}{k} \tanh kh}. \quad (16)$$

On deep water when $kh \rightarrow \infty$ the hyperbolic tangent function $\tanh kh \sim 1$ and,

$$c = \sqrt{\frac{g\lambda}{2\pi}}. \quad (17)$$

(17) shows that for free surface gravity waves on deep water the phase speed c is proportional to the square root of the wavelength $\sqrt{\lambda}$. Waves for which c is a function of λ , are called dispersive because waves of different wavelengths, propagate at different speeds, and disperse or separate, Kundu and Cohen (2008).

The group velocity is given by,

$$c_g = \frac{d\omega}{dk}. \quad (18)$$

By substituting equation (13) into (18),

$$c_g = \frac{c}{2} \left(1 + \frac{2kh}{\sinh 2kh} \right). \quad (19)$$

On deep water,

$$c_g = \frac{c}{2}. \quad (20)$$

The rate of transmission of energy of a sinusoidal wave component is the wave energy times the group velocity, Kundu and Cohen (2008),

$$F = Ec_g, \quad (21)$$

so according to linear theory, the wave energy is transmitted with the group velocity c_g .

The regular wave solution in (11),

$$\eta(x, t) = a \cos(kx - \omega t),$$

can from Euler's identity be written in terms of the exponential function such that,

$$\begin{aligned} \eta(x, t) &= \frac{a}{2} \left[e^{i\theta} + e^{-i\theta} \right] \\ &= \frac{a}{2} e^{i\theta} + \text{c.c.} \\ &= \text{Re} \left[a e^{i\theta} \right], \end{aligned} \quad (22)$$

where $\theta = kx - \omega t$ is the phase function, $i = \sqrt{-1}$ is the imaginary unit, c.c. denotes the complex conjugate, and Re denotes the real part of the complex number. Given that (22) is a regular wave, its propagation will satisfy the linear dispersion relation $\omega = \omega(k)$ in equation (13).

Linear theory assumes that the free surface η is a random linear superposition of n non-interacting regular waves,

$$\eta(x, t) = \sum_n a_n \cos(k_n x - \omega_n t + \psi_n) \quad (23)$$

where $\theta_n = k_n x - \omega_n t$ are the phase functions, ψ_n are random uniformly distributed phases, and each regular wave in equation (23) satisfies the linear dispersion relation,

$$\omega_n = \omega(k_n). \quad (24)$$

In terms of the exponential function, (23) can be written on the form,

$$\begin{aligned} \eta(x, t) &= \sum_n \frac{a_n}{2} \left[e^{i(\theta_n + \psi_n)} + e^{-i(\theta_n + \psi_n)} \right] \\ &= \sum_n \frac{1}{2} A_n e^{i\theta_n} + \text{c.c.} \end{aligned} \quad (25)$$

where the complex number $A_n = a_n e^{i\psi_n}$ has been introduced. When a synthetic wave field is composed from a random linear superposition, a common approach is to relate the amplitudes a_n of the waves to a frequency spectrum $a_n = \sqrt{2S(\omega_n)\Delta\omega}$, or a wavenumber spectrum, where the energy at each frequency component $S(\omega_n)$ is given from alternative distributions; Gaussian, JONSWAP, etc. This approach is applied to create the synthetic wave field with a JONSWAP spectral frequency distribution in the numerical model in chapter 8.

2.2 Nonlinearity

We distinguish two types of nonlinearity,

- Static nonlinearity due to wave reconstruction leading to various dispersion shells.
- Dynamic nonlinearity due to energy transfer among different wave components over long spatial propagation distances leading to various distributions of wave energy.

As mentioned in the introduction the static nonlinearities which leads to reconstruction of the freely propagating waves are added to the linear field by considering straightforward perturbation expansions of the surface elevation. In (k, ω) -space the frequency and wavenumber components of the higher harmonic bounded waves are assumed to be distributed along various dispersion shells. In comparison with the measured dispersion relations in chapter 7 we have plotted the curves for,

$$(q\omega)^2 = gqk \tanh(qkh), \quad (26)$$

where $q = 1, 2$ and 3 and $q = 1$ corresponds to the linear dispersion relation, also referred to as the first order dispersion shell, $q = 2$ corresponds to the second order dispersion shell and $q = 3$ corresponds to the third order dispersion shell.

The dynamic nonlinearities are caused by energy transfer among different wave components which leads to various distributions of wave energy. The dynamic nonlinearities evolve over longer propagation distances. We were particularly interested in investigating how the wave energy of the free waves were distributed adjacent to the linear dispersion relation. If the wave energy is distributed tangentially to the linear dispersion relation $\omega = \omega(k)$ this could, from a very simplified perspective, indicate that the free waves propagate with the group velocity $c_g = d\omega/dk$, which by mathematical definition is tangential to the linear dispersion relation curve.

As mentioned in the introduction the dynamic nonlinearity is contained in the (M)NLS evolution equations. The nonlinear models can be summarized in the following evolution equation for the first harmonic complex amplitude $B(x, t)$ of the free waves, Krogstad and Trulsen (2010),

$$\begin{aligned} \frac{\partial B}{\partial t} + \mathfrak{L}B + \frac{i\omega_c k_c^2}{2}|B|^2 B \\ + \left[\frac{5\omega_c k_c}{4}|B|^2 \frac{\partial B}{\partial x} + \frac{\omega_c k_c}{4} B \frac{\partial |B|^2}{\partial x} + ik_c B \frac{\partial \bar{\phi}}{\partial x} \right] = 0, \\ \text{at } z = 0, \end{aligned}$$

where the terms in the brackets are discarded for the NLS equation and included for the MNLS equation. The characteristic wavenumber k_c and angular frequency ω_c are related by the linear dispersion relation. The linear dispersive part is written in the exact form and the differential operator \mathfrak{L} is defined in terms of,

$$\mathfrak{L} = i \left\{ \sqrt{g \sqrt{\left(k_c - i \frac{\partial}{\partial x}\right)^2}} - \sqrt{gk_s} \right\}.$$

For the MNLS equation the induced flow is also added,

$$\begin{aligned}\frac{\partial \bar{\phi}}{\partial z} &= \frac{\omega_c}{2} \frac{\partial |B|^2}{\partial x} \quad \text{at } z = 0, \\ \frac{\partial^2 \bar{\phi}}{\partial x^2} + \frac{\partial^2 \bar{\phi}}{\partial z^2} &= 0 \quad \text{for } -\infty < z < 0, \\ \frac{\partial \bar{\phi}}{\partial z} &= 0 \quad \text{at } z \rightarrow -\infty.\end{aligned}$$

The reconstruction of the surface elevation η includes static nonlinear bounded waves which takes the form,

$$\eta = [\bar{\eta}] + \frac{1}{2}(Be^{i\theta} + B_2e^{2i\theta} + [B_3e^{3i\theta}] + \text{c.c.}),$$

where $\theta = k_c x - \omega_c t$ is the phase function and c.c. denotes the complex conjugate. Again the terms in the brackets are discarded for the NLS equation and included for the MNLS equation. The bound wave components are given by,

$$B_2 = \frac{k_c}{2} B^2 - \left[\frac{i}{2} B \frac{\partial B}{\partial x} \right], \quad B_3 = \frac{3k_c^2}{8} B^3, \quad \bar{\eta} = -\frac{1}{g} \frac{\partial \bar{\phi}}{\partial t}.$$

The (M)NLS equations are the result of a perturbation expansion with respect to two small parameters, the steepness and the bandwidth. The zeroth-harmonic bound waves appears at third order. This is due to the fact that as a result of the perturbation expansion the zeroth-harmonic bound waves turns out to be the product of the bandwidth and the square of the steepness, Krogstad and Trulsen (2010).

The (k, ω) -spectra resulting from the nonlinear spatiotemporal evolution of the long-crested unidirectional irregular waves on infinite depth, described above, are shown in figure 5 and 7 in Krogstad and Trulsen (2010). Figure 5 shows the spectra resulting from the simulation with the NLS evolution equation and figure 7 shows the spectra resulting from the simulation with the MNLS evolution equation. The wave fields have been reconstructed to second and third order, respectively. For both spectra the amplitudes of the waves are initialized from a Gaussian bell-shaped wavenumber spectrum with scaled RMS width $\sigma_x = 0.1$. The steepness $\epsilon = k_c a_c = 0.1$, where k_c is the characteristic wavenumber, and the characteristic amplitude is $a_c = \sqrt{2\langle \eta^2 \rangle}$. The spectral estimates are taken from spatiotemporal measurements covering 140 peak wavelengths and 170 peak periods.

In figure 5 and 7 in Krogstad and Trulsen (2010), the white curve corresponds to the linear dispersion relation. The separate wave energy distributions above and under the linear dispersion relation corresponds to the various dispersion shells of the higher harmonic waves caused by the static nonlinearities. The deviation of wave energy distributions from the linear dispersion relation corresponds to dynamic nonlinearities. The numerical simulations suggest that components above the spectral peak have larger phase and group velocities than anticipated by linear theory. Moreover, the spectrum does not maintain a thin well-defined dispersion surface, but rather develops into a continuous distribution in (k, ω) -space.

3 Experimental arrangements

In this chapter the experimental arrangements are presented. In principal two different arrangements were used in the wave flume. The first arrangement presented in section 4.1 was applied in an early stage of the experimental work. In these experiments a stationary array with four ultrasonic probes was used to measure the surface elevation. The second arrangement presented in section 4.3 was applied in a later stage of the experimental work. In these experiments a stationary array with sixteen probes was used to measure the surface elevation and an acoustic Doppler current profiler (ADCP) was used to measure the wave-induced fluid particle velocities. In section 4.2 a detailed presentation of the synthetic array design is given. The synthetic array is central in the development of high-resolution spatiotemporal measurements of the surface elevation.

3.1 Early stage experimental arrangement

The experiments were carried out in the long wave flume in the Hydrodynamic laboratory at the University of Oslo, Blindern. The wave flume is 24.6 m long and 0.5 m wide. Figure 1 shows a 1:193 scaled version of the wave flume with the experimental arrangement which was used in the early stage of the experimental work. In these experiments the wave flume was filled with $h = 0.35$ m of water.

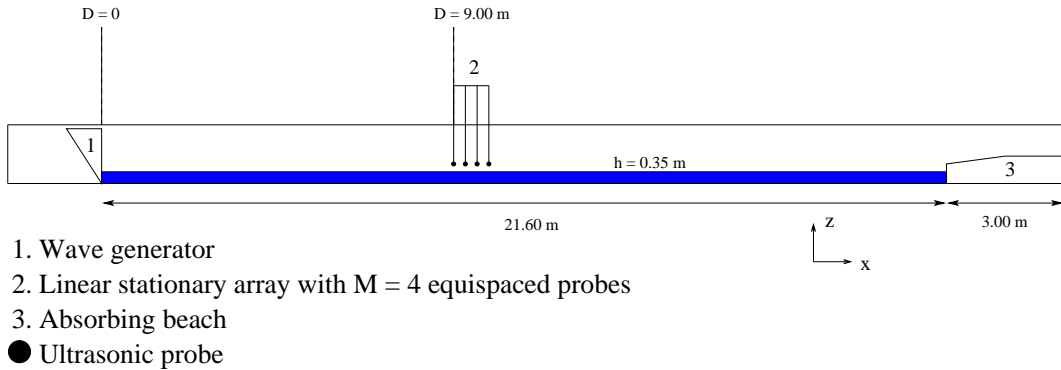


Figure 1: Early stage experimental arrangement.

At the left end of the wave flume there is a hydraulic piston wave generator (1) which induces water surface waves into the flume. The wave generator is controlled by a computer software, Wavelab[©]. In Wavelab input files in electrical Voltage can be given for the back and forth movement of the wave generator. In the experiments six input files from a foregoing project, Grue et al. (2003), was applied. The input files give irregular wave fields with spectral distributions based on different JONSWAP spectra. The wave fields which are generated from the six input files are defined as series 1-6. The length of each time series is about five and a half minutes (330 s). We attempted to modify the original input files to increase the amplitude in the generated time series. The modifications of the original input files are presented in more detail in Appendix B.1.1.

The waves which are generated into the flume are long-crested and the crests and the troughs of the waves extend over the entire width of the flume perpendicular to the propagation direction. This allows us to consider waves which propagate along one axis. The x -axis is defined to be the axis along the longitudinal direction of the wave flume. The z -axis is defined to be the vertical axis. The mean water level

is defined to be at $z = 0$. This reference system is also applied in the theoretical framework and in the method of analysis in chapter 2 and 4.

At the right end of the wave flume there is an absorbing beach (3). The beach reflects less than 3% of the amplitude of the incoming waves from the wave generator, Grue et al. (2003). At a water depth of $h = 0.35$ m the reflection of incoming waves was larger than at a water depth of $h = 0.60$ m which was the water depth that was applied at a later stage of the experimental work. This was caused by that at $h = 0.35$ m the waves hit the vertical edge of the absorbing beach which increases the presence of reflected waves in the flume. With the absorbing beach operational the waves are approximately unidirectional. With increased reflection the waves are strictly not unidirectional, but propagate only along the longitudinal direction of the wave flume.

The surface elevation is measured with a set of ultrasonic U-GAGE S18U probes from Banner®. The probes are vertically looking and located 15 cm above the mean water level at the half-width of the wave flume. In distinction to capacitance or resistance-type wave gauges the ultrasonic probes are non-intrusive and do not affect the wave propagation. The probes are controlled by a computer software, LabView©. In LabView the probes are set to measure the surface elevation in a window ranging from $-5 \text{ cm} < z < 5 \text{ cm}$. At the early stage of the experimental work a linear stationary array with $M = 4$ equispaced probes placed $\Delta x = 0.30$ cm apart (2), was applied to measure the surface elevation. These four probes are defined as P1, P2, P3 and P4 respectively. The array was placed $D = 9.00$ m from the wave generator. D is defined to be the distance between the wave generator and the first probe P1 in the array. This distance is indicated in figure 1.

The sampling rate of the data acquisition was 200 Hz. In the experiments $N = 68000$ samples (340 s) of the wave field were taken by each probe and in the spectral analysis the first 12000 samples (60 s) and the last 4000 samples (20 s) were removed. This was done to remove the effect of startup waves from the wave generator and to obtain information from the wave field after that it had stabilized for some time and to remove the samples of the wave field which were taken after the wave generator ceased to generate waves into the wave flume.

The probes were triggered to start the measurement simultaneously with the wave generator. In the experiments the probes were triggered to start the measurement of the surface elevation 1 s before the wave generator started to generate waves into the flume.

The ultrasonic probes have a sensing range from $s_{min} = 3$ cm to $s_{max} = 30$ cm, and emit ultrasonic sound at frequencies of 300 kHz. When a pulse of ultrasonic energy is emitted it will travel through the air at the speed of sound. A portion of this energy is reflected by the water surface and travels back to the sensor. The sensor measures the total time required for the energy to reach the target and return to the sensor. The distance to the water surface is then calculated simply by

$$d_s = \frac{c_s t_t}{2},$$

where d_s is the distance from the sensor to the water surface, $c_s \approx 343$ m/s is the speed of sound in air, and t_t is the transit time for the ultrasonic pulse to reach the target and return to the sensor. All the ultrasonic probes which were applied in the experiment were calibrated and in Appendix B.1.2 the calibration procedure is explained in more detail.

There are limitations to which extent the ultrasonic probes can measure an inclined surface. At a minimum sensing range s_{min} the maximum target inclination angle is $\alpha_{s_{min}} = 10^\circ$, and decreases to a maximum target inclination angle of approximately $\alpha_{s_{max}} = 5^\circ$ at the maximum sensing range s_{max} . Beyond these angles the signal from a probe reflects off the target at such a large reflection angle that

it cannot return to the sensor. This effect is particularly seen when steep waves are measured, and dropouts in the measured surface elevation data appear at steep spatial locations, between the crest and the troughs. A cubic interpolation method was developed to replace the dropouts. A more detailed presentation of the interpolation method is given in chapter 5.

Another problem, common for all digital and electrical measuring devices, is noise, which is handled with filtering. Noise can also be seen in the measurement data from the ultrasonic probes. The filter applied is presented in more detail in chapter 5.

3.2 Synthetic array design

The upper array in figure 2 illustrates the stationary array with 4 equispaced probes from figure 1. The probes were placed $\Delta x = 30$ cm apart.

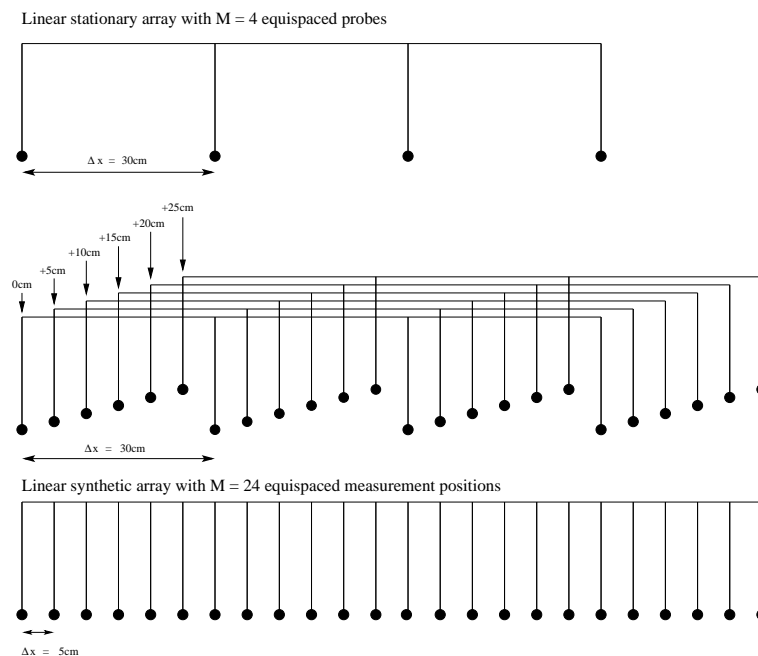


Figure 2: A stationary array and synthesis of a more dense array.

For two identical electrical signals the wave generator moves back and forth with the exact same motions. In Grue et al. (2003) it was reported that the wave fields are very repeatable, but it was also reported about small repetition differences in the wave fields. Due to nonlinear wave interactions we might doubt that the wave generator will generate the exact same spatial and temporal wave field in the wave flume from two identical input files. It might be expected that two wave fields which are generated from the same input file over a long time period can be slightly different due to nonlinear wave interactions. The repeatability of two time series is presented in more detail and discussed in chapter 5, and shows that there generally is a 1-3% relative error between two time series which are generated with the absorbing beach operational at the far end of the wave flume. In experiments with constructions at the far end of the wave flume which provides increased reflection and steeper wave fields, the relative errors increases. This is mostly caused by dropouts in the surface elevation data, which in worst case extends

over entire crests or troughs, leading to failure of the interpolation method. The problem is presented in more detail in chapter 5.

The stationary array is mobile on rails along the length D of the waveflume. Since the wave field is approximately repeatable we can create synthesis of a much more dense array. This can be done by systematically displacing the stationary array to new spatial locations and measure the wave field at each spatial location. In the early stage of the experimental work the stationary array was displaced 5 cm for each measurement so that a synthesis of an array with $M = 24$ equispaced measurement positions, placed $\Delta x = 5$ cm apart, was created. This procedure is sketched in figure 2. Six measurements of the five and a half minute time series are required to create the synthetic array in figure 2. The (k, ω) -spectra from the synthetic array provides better resolution along the wavenumber axis compared to the stationary array. But even for the synthetic array with $M = 24$ measurement positions the wavenumber resolution is quite poor. A stationary array with sixteen probes was therefore developed. This array is presented in the next section.

3.3 Later stage experimental arrangement

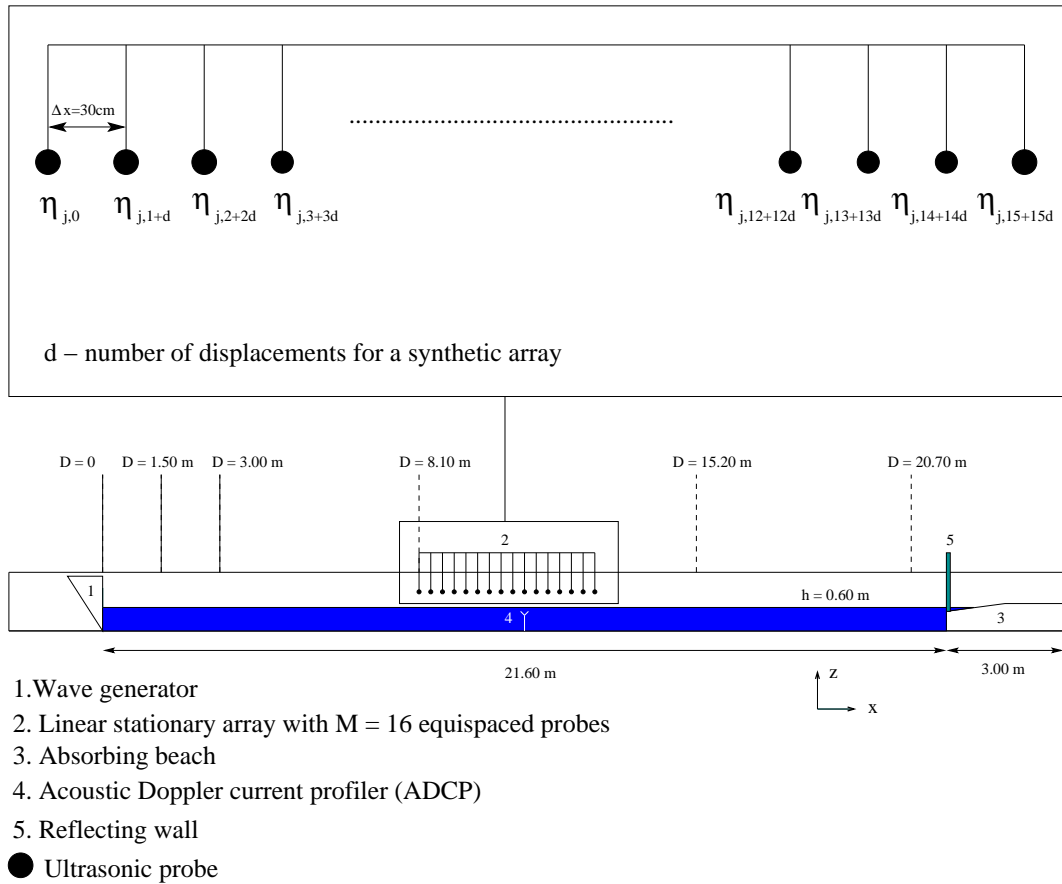


Figure 3: Later stage experimental arrangement.

The lower part of figure 3 shows a 1:193 scaled version of the wave flume with the experimental arrangement which was used at a later stage in the experimental work. In these experiments the wave flume was filled with $h = 0.60$ m of water. The linear

array with four equispaced probes was substituted by a linear array with sixteen equispaced probes (2) and figure 4. All the probes P1-P16 were placed $\Delta x = 30$ cm apart from each other. D is defined to be the distance between the wave generator and the first probe P1.



Figure 4: The linear array, wave generator (end) and the wave field.



Figure 5: ADCP in horizontal position and bottom rack.

An ADCP (4) and figure 5 was applied to measure the wave-induced fluid particle velocities. The ADCP was placed 10.8 m from the wave generator at the half-width of the flume. The ADCP has a bi-static sonar type sensor and sends out ultrasound from a centered beam. The ultrasound has a frequency of 10 MHz. The reflected signal is received by four sensors. The water is seeded with $20 \mu\text{m}$ polamid spheres to increase the reflection. The u , v , and w components of the fluid particle velocities are measured at one point which is located about 5 cm above the sensors. The ADCP is controlled by a computer software VECTRINO+ where data for the u , v , and w components of the fluid particle velocities are collected in data columns. The u , v , and w components are related to a fixed coordinate system on the measuring device. When the current at the bottom was measured the ADCP was, for practical

purposes, placed in a horizontal position, and when the current near the mean water level was measured the ADCP was placed in a vertical position. Since the velocities are related to a fixed coordinate system, the data for the u -velocity is collected in different columns in the Vectrino+ software, depending on the horizontal or vertical positioning. Different racks were used near the bottom (figure 5) and near the mean water level.

The sampling rate of the data acquisition was set to 200 Hz, which is the similar sampling rate used to measure the surface elevation. In the experiments the ADCP was not triggered electronically but started manually simultaneously with the wave generator. About $N = 68000$ time samples (340 s) were taken from each wave series and for the statistical analysis of the ADCP data in chapter 6 the first 12000 samples (60 s) and the last 4000 samples (20 s) were removed. Thus, information about the wave-induced current was taken from the same time window which was applied for the spectral estimate of the surface elevation.

At the far end of the wave flume it was possible to place a reflecting wall (5) in front and on top of the vertical edge of the absorbing beach (3). The reflecting wall is placed in a vertical position and is mounted on rails on the inside side-walls of the wave flume. The reflecting wall can be removed easily. A reflecting beach with 25° inclination, measured from the horizon, was also applied to increase the wave reflection. The reflecting beach and the reflecting wall is presented in more detail in chapter 7. In experiments where the reflection from the absorbing beach and the reflecting wall was investigated the wave field from series 1 was measured at $D = 3.00$ m, 8.10 m and 15.20 m from the wave generator. These distances are indicated in figure 3.

The upper part of figure 3 sketches a general description of how the probes in the stationary array with sixteen probes are represented in a synthetic array. d is the number of displacements of the stationary array to create synthesis of more dense arrays. For the synthetic array which was based on the stationary array with four probes in section 3.2 the number of displacements was $d = 5$. As illustrated in the upper part of figure 3 the measured time series of the surface elevation from each stationary probe in a synthetic array can generally be represented by

$$\eta_{n,m+md} \quad \text{where } d = \text{number of displacements,} \quad (27)$$

$n = 0, 1, 2, \dots, N - 1$ is the number of time samples and $m = 0, 1, 2, \dots, 15$ is the number of measurement positions in the stationary array. With no displacement $d = 0$ the above description represents the stationary array with sixteen probes. If the number of displacements is chosen to be $d = 5$ for the stationary array with sixteen probes, $\Delta x = 5$ cm = 0.05 m and the last surface elevation measurement $\eta_{n,15+15d+d} = \eta_{n,95}$. This corresponds to a synthetic array with $M = 96$ measurement positions. Each probe has a Δx associated with them so the length of the array is equal to $L = M\Delta x = 96 \times 0.05$ m = 4.8 m.

The measurement procedure presented above can be characterized as a measurement sub-procedure. The sub-procedure can be linked by distances Δx up to four times along the wave flume to create longer synthetic linear equispaced arrays. The longest synthetic array covered a propagation length of $L = 4 \times 4.8$ m = 19.2 m with $M = 256$ measurement positions and a spatial resolution of $\Delta x = 7.5$ cm. The number of displacements in each of the four sub-procedures was $d = 3$. The surface elevation measurement $\eta_{n,0}$ was taken $D = 1.5$ m from the wave generator, and the surface elevation measurement $\eta_{n,255}$ was taken $D = 20.7$ m from the wave generator. These distances are indicated in figure 3. Sixteen measurements of the five and a half minutes time series are required to create this synthetic array.

4 Method of analysis

4.1 Discrete Fourier transform

For the Fourier analysis of the experimental data we have applied the discrete Fourier transform DFT, which has been computed with the fast Fourier transform algorithm FFT implemented in Matlab[®].

The temporal discrete Fourier transform is defined on a finite time interval T . The finite number of samples in time, is defined as N . Each discrete time step is defined in terms of,

$$t_n = n\Delta t \quad (28)$$

where,

$$T = N\Delta t \quad (29)$$

for a number of time samples $n = 0, 1, 2, \dots, N - 1$. In terms of the free surface η the temporal DFT is defined as,

$$\eta(t_n) = \sum_{j=0}^{N-1} \hat{\eta}(\omega_j) e^{-i\omega_j t_n}. \quad (30)$$

The discrete angular frequency steps,

$$\omega_j = \frac{2\pi j}{T} \quad \text{where} \quad \Delta\omega = \frac{2\pi}{T}, \quad (31)$$

and $j = 0, 1, \dots, N - 1$. $\hat{\eta}_j$ is obtained by utilizing the mathematical property that a system of complex exponential functions is an orthogonal system of functions, and by taking the l_2 inner product of (30), see Appendix C.1.1, we obtain,

$$\hat{\eta}(\omega_j) = \frac{1}{N} \sum_{n=0}^{N-1} \eta(t_n) e^{i\omega_j t_n}. \quad (32)$$

(30) and (32) is the 1D temporal DFT pair.

Figure 6 shows an illustration of an array with $M = 4$ elements similar to the stationary array with four probes from our experiments.

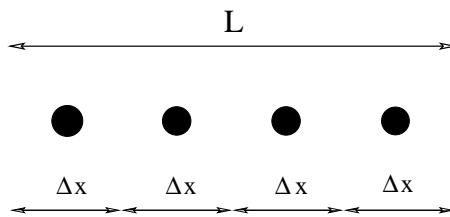


Figure 6: Example of an array with $M = 4$ elements.

For an array with M finite elements, the spatial DFT is defined on a finite spatial interval L which corresponds to the total spatial extension of the array. Each element in the array has a finite spatial extension Δx associated with them, which is equal to the horizontal distance between the elements. The total extension of the array is equal to,

$$L = M\Delta x. \quad (33)$$

The discrete spatial steps,

$$x_m = m\Delta x \quad (34)$$

for a number of spatial measurement points $m = 0, 1, 2, \dots, M - 1$. The discrete wavenumber steps,

$$k_g = \frac{2\pi g}{L} \quad \text{where} \quad \Delta k = \frac{2\pi}{L} \quad (35)$$

for $g = 0, 1, 2, \dots, M - 1$. The 1D spatial DFT pair is,

$$\eta(x_m) = \sum_{g=0}^{M-1} \hat{\eta}(k_g) e^{ik_g x_m} \quad (36)$$

and

$$\hat{\eta}(k_g) = \frac{1}{M} \sum_{m=0}^{M-1} \eta(x_m) e^{-ik_g x_m}. \quad (37)$$

A combination of (30), (32), (36), and (37) gives the 2D spatiotemporal DFT pair,

$$\eta(x_m, t_n) = \sum_{g=0}^{M-1} \sum_{j=0}^{N-1} \hat{\eta}(k_g, \omega_j) e^{i(k_g x_m - \omega_j t_n)} \quad (38)$$

$$\hat{\eta}(k_g, \omega_j) = \frac{1}{MN} \sum_{m=0}^{M-1} \sum_{n=0}^{N-1} \eta(x_m, t_n) e^{-i(k_g x_m - \omega_j t_n)}. \quad (39)$$

In section 5.9 Sampling, more information about sampling criteria for $\Delta\omega$, Δk , Δt and Δx is given.

In general N discrete time samples of the surface elevation η measured from M discrete measurement positions placed Δx apart in the experiments can be represented by a $N \times M$ matrix,

$$\eta_{n,m} = \begin{pmatrix} \eta_{0,0} & \eta_{0,1} & \eta_{0,2} & \cdots & \eta_{0,M-3} & \eta_{0,M-2} & \eta_{0,M-1} \\ \eta_{1,0} & \eta_{1,1} & \eta_{1,2} & & \eta_{1,M-3} & \eta_{1,M-2} & \eta_{1,M-1} \\ \eta_{2,0} & \eta_{2,1} & \eta_{2,2} & & \eta_{2,M-3} & \eta_{2,M-2} & \eta_{2,M-1} \\ \vdots & & & \ddots & & & \vdots \\ \eta_{N-3,0} & \eta_{N-3,1} & \eta_{N-3,2} & & \eta_{N-3,M-3} & \eta_{N-3,M-2} & \eta_{N-3,M-1} \\ \eta_{N-2,0} & \eta_{N-2,1} & \eta_{N-2,2} & & \eta_{N-2,M-3} & \eta_{N-2,M-2} & \eta_{N-2,M-1} \\ \eta_{N-1,0} & \eta_{N-1,1} & \eta_{N-1,2} & \cdots & \eta_{N-1,M-3} & \eta_{N-1,M-2} & \eta_{N-1,M-1} \end{pmatrix}$$

where the columns are the time series and the rows are the space series of the surface elevation. $\hat{\eta}_{j,g}$ is computed from the 2D DFT, which results in the matrix,

$$\hat{\eta}_{j,g} = \begin{pmatrix} \hat{\eta}_{0,0} & \hat{\eta}_{0,1} & \hat{\eta}_{0,2} & \cdots & \hat{\eta}_{0,M-3} & \hat{\eta}_{0,M-2} & \hat{\eta}_{0,M-1} \\ \hat{\eta}_{1,0} & \hat{\eta}_{1,1} & \hat{\eta}_{1,2} & & \hat{\eta}_{1,M-3} & \hat{\eta}_{1,M-2} & \hat{\eta}_{1,M-1} \\ \hat{\eta}_{2,0} & \hat{\eta}_{2,1} & \hat{\eta}_{2,2} & & \hat{\eta}_{2,M-3} & \hat{\eta}_{2,M-2} & \hat{\eta}_{2,M-1} \\ \vdots & & & \ddots & & & \vdots \\ \hat{\eta}_{N-3,0} & \hat{\eta}_{N-3,1} & \hat{\eta}_{N-3,2} & & \hat{\eta}_{N-3,M-3} & \hat{\eta}_{N-3,M-2} & \hat{\eta}_{N-3,M-1} \\ \hat{\eta}_{N-2,0} & \hat{\eta}_{N-2,1} & \hat{\eta}_{N-2,2} & & \hat{\eta}_{N-2,M-3} & \hat{\eta}_{N-2,M-2} & \hat{\eta}_{N-2,M-1} \\ \hat{\eta}_{N-1,0} & \hat{\eta}_{N-1,1} & \hat{\eta}_{N-1,2} & \cdots & \hat{\eta}_{N-1,M-3} & \hat{\eta}_{N-1,M-2} & \hat{\eta}_{N-1,M-1} \end{pmatrix}$$

The spectral energy density is computed from,

$$S(k_g, \omega_j) = |\hat{\eta}_{g,j}|^2 = \hat{\eta}_{g,j} \hat{\eta}_{g,j}^* \quad (40)$$

where * denotes the complex conjugate c.c. With matrix representation,

$$S_{j,g} = \begin{pmatrix} S_{0,0} & S_{0,1} & S_{0,2} & \cdots & S_{0,M-3} & S_{0,M-2} & S_{0,M-1} \\ S_{1,0} & S_{1,1} & S_{1,2} & & S_{1,M-3} & S_{1,M-2} & S_{1,M-1} \\ S_{2,0} & S_{2,1} & S_{2,2} & & S_{2,M-3} & S_{2,M-2} & S_{2,M-1} \\ \vdots & & & \ddots & & & \vdots \\ S_{N-3,0} & S_{N-3,1} & S_{N-3,2} & & S_{N-3,M-3} & S_{N-3,M-2} & S_{N-3,M-1} \\ S_{N-2,0} & S_{N-2,1} & S_{N-2,2} & & S_{N-2,M-3} & S_{N-2,M-2} & S_{N-2,M-1} \\ S_{N-1,0} & S_{N-1,1} & S_{N-1,2} & \cdots & S_{N-1,M-3} & S_{N-1,M-2} & S_{N-1,M-1} \end{pmatrix}$$

In the (k, ω) -spectra in chapter 7 the scalar values from $S_{j,g}$ are plotted as contour levels for the corresponding discretizes k_g and ω_j values.

The angular frequency and wavenumber spectra in chapter 5 are computed from,

$$S(\omega_j) = |\hat{\eta}(\omega_j)|^2 \quad (41)$$

and,

$$S(k_g) = |\hat{\eta}(k_g)|^2. \quad (42)$$

The discrete Fourier transform can be extended periodically, or cyclically permuted such that temporally,

$$\eta_{n+N} = \eta_n \quad \text{and} \quad \hat{\eta}_{j+N} = \hat{\eta}_j \quad (43)$$

and spatially,

$$\eta_{m+M} = \eta_m \quad \text{and} \quad \hat{\eta}_{g+M} = \hat{\eta}_g. \quad (44)$$

Look at for instance,

$$\begin{aligned} e^{ik_{g+M}x_m} &= e^{i\frac{2\pi(g+M)}{L} \frac{Lm}{M}} \\ &= e^{i2\pi(g+M)\frac{m}{M}} \\ &= e^{i\frac{2\pi gm}{M}} e^{i2\pi m} \\ &= e^{i\frac{2\pi gm}{M}} \cdot 1 = e^{i\frac{2\pi g}{L} \frac{Lm}{M}} = e^{ik_g x_m}. \end{aligned} \quad (45)$$

We can start the transform summation at any index r ,

$$\begin{aligned} \hat{\eta}_g &= \frac{1}{M} \sum_{g=r}^{r+M-1} \eta_m e^{-ik_g x_m} \\ &= \frac{1}{M} \sum_{g=r}^{r+M-1} \left(\sum_{h=0}^{M-1} \hat{\eta}_h e^{ik_g x_h} \right) e^{-ik_g x_m} \\ &= \sum_{h=0}^{M-1} \hat{\eta}_h \frac{1}{M} \sum_{i=r}^{r+M-1} e^{ik_g(x_h - x_m)} \\ &= \sum_{h=0}^{M-1} \hat{\eta}_h \delta_{h,m} \\ &= \hat{\eta}_g, \end{aligned} \quad (46)$$

which shows that the discrete Fourier transform is periodic, and has a cyclic permutation from any index r . Discontinuities in the transition from the end of a space or time series to the beginning of the series are handled with tapering in time and

space, which is presented more detail in chapter 5.

It can sometimes be convenient to discretize the angular frequencies and the wavenumbers for negative values,

$$\omega_j = \frac{2\pi j}{T} \quad (47)$$

for $j = -N/2, -(N-1)/2, \dots, -2, -1, 0, 1, 2, \dots, (N-1)/2, N/2$ and,

$$k_g = \frac{2\pi g}{L} \quad (48)$$

for $g = -M/2, -(M-1)/2, \dots, -2, -1, 0, 1, 2, \dots, (M-1)/2, M/2$.

When $S(\omega_j)$ and $S(k_g)$ are computed for the experimental data from the 1D temporal and spatial DFT for $j = 0, 1, \dots, N-1$ and $g = 0, 1, \dots, M-1$, one peak appears for low discretised values and one peak appear for high discretised values. Due to the periodicity of the Fourier transform the peak at the highest discretized values can be cyclically permuted and discretized for negative angular frequencies and wavenumbers. This representation has been referred to as the two-sided spectra $S_{(2)}(\omega_j)$ and $S_{(2)}(k_g)$ for $\omega \gtrless 0$ and $k \gtrless 0$. It has also sometimes been convenient to refer to the one-sided spectra $S(\omega_j) = 2S_{(2)}(\omega_j)$ and $S(k_g) = 2S_{(2)}(k_g)$.

In a similar manner, the columns and rows in the matrix representation of the spectral energy density $S_{j,g}$ can be cyclically permuted and discretized for negative angular frequencies and wavenumbers. This has been done for all the (k, ω) -spectra in chapter 7, but in some of the spectra only the spectral energy density for positive angular frequencies $\omega \geq 0$ has been contour plotted. The spectral energy density for negative angular frequencies $\omega \leq 0$ is the energy from waves which are represented by the complex conjugate c.c. and we have chosen to give the water surface waves with positive angular frequencies $\omega \geq 0$ a physical interpretation.

5 Surface elevation

For the surface elevation in total 23 experiments were carried out to measure the dispersion relations, and as a consequence of the synthetic array measurement techniques in total 2376 measurements of the five and a half minute time series 1-6 and modified series were taken. The time series were measured on two different water depths $h = 0.35$ m and $h = 0.60$ m, and on a range of different locations from 1.5 m to 20.7 m from the wave generator. Series 1 was also measured with the additional reflecting beach and end wall. The collection of surface elevation data is therefore quite extensive, and only recordings from two experiments are selected for the analysis in the sections in this chapter. The recordings represents four time series from a experiment with the absorbing beach operational at the far end of the wave flume and four time series from a experiments where the absorbing beach was substituted by the reflecting wall. The intention of presenting the data in this manner has been to show the difference between the two generated wave fields, both with regard to signal processing issues and with regard to the energy in the wave fields.

The surface elevation measurements were done by the first four probes P1-P4 in the stationary array with sixteen probes at $D = 8.1, 8.4, 8.7$ and 9.0 m from the wave generator ($\Delta x = 0.30$ cm). For the wavenumber spectra recordings from the synthetic array which provided the largest number of spatial measurement points $M = 256$, over the longest measured propagation length $L = 19.2$ m, were chosen for the spectral analysis. For the frequency and wavenumber spectra and the (k, ω) -spectra in chapter 7 the first 60 s and the last 20 s of each time series were removed for the spectral estimates.

The chapter is divided into nine sections. The first four sections 5.1 - 5.4 present the time series of the surface elevation itself and deals with technical issues connected to the signal processing of the raw data from the ultrasonic probes. In section 5.5 and 5.6 the tapering functions applied to taper the data in time and space are presented. In section 5.7 and 5.8 the frequency and wavenumber spectra are presented and the dimensional analysis to obtain information about the steepness of the wave fields and the normalized bandwidths of the frequency spectrums is presented. Section 5.9 presents sampling issues connected the measured surface elevations and the (k, ω) -spectra which will be presented in chapter 7.

5.1 Interpolation

Figure 7 shows the raw data from the measurement by P1 of time series 1 at $D = 8.1$ m from the wave generator with the absorbing beach operational at the far end of the wave flume. The measurement is in total 340 s, and the first 10 s shows the calm water surface which is measured before the first wave in the wave train reaches the water surface under the probe. The spikes extending vertically up to $\eta = 5$ cm are dropouts at the steepest locations between the crests and the troughs, caused by the limitations in the probes to measure the inclined surface. The dropouts appeared quite frequently in the raw data, and a looping sequence was developed to interpolate the surface elevation between the points where the dropouts appeared. If the measured data points exceed the thresholds $|\eta_{n+1,m} - \eta_{n,m}| > 1/2$, $\eta_{n,m} > 4.9$ and $\eta_{n,m} < -4.9$ these points are removed and the looping sequence interpolates between the removed points. The thresholds $\eta_{n,m} > 4.9$ and $\eta_{n,m} < -4.9$ are defined to be larger and smaller than the highest crest and lowest trough respectively, in both the wave field generated with the reflecting wall and with the absorbing beach. A quantitative illustration of the looping sequence is given in section 5.4.

The upper part of figure 8 shows a 20 s abstract from figure 7 after 180 s of wave generation. We see that the dropouts appear on the largest and steepest waves. The lower part of the figure shows the surface elevation after a cubic interpolation has

been used to interpolate between the points where the dropouts appear. It is expected that the cubic interpolation method is a good estimate for the surface elevation. At least the only alternative to deal with the problem of the dropouts is to apply interpolation.

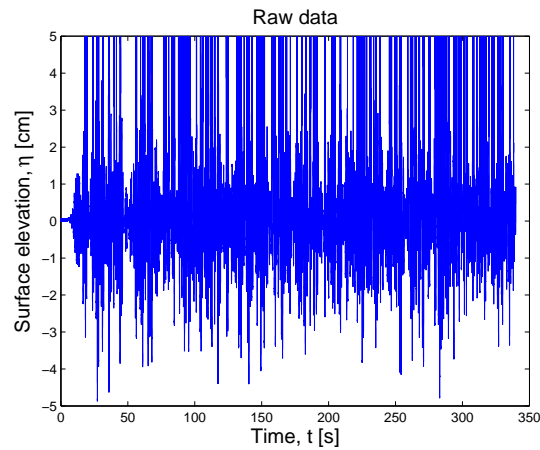


Figure 7: Raw data.

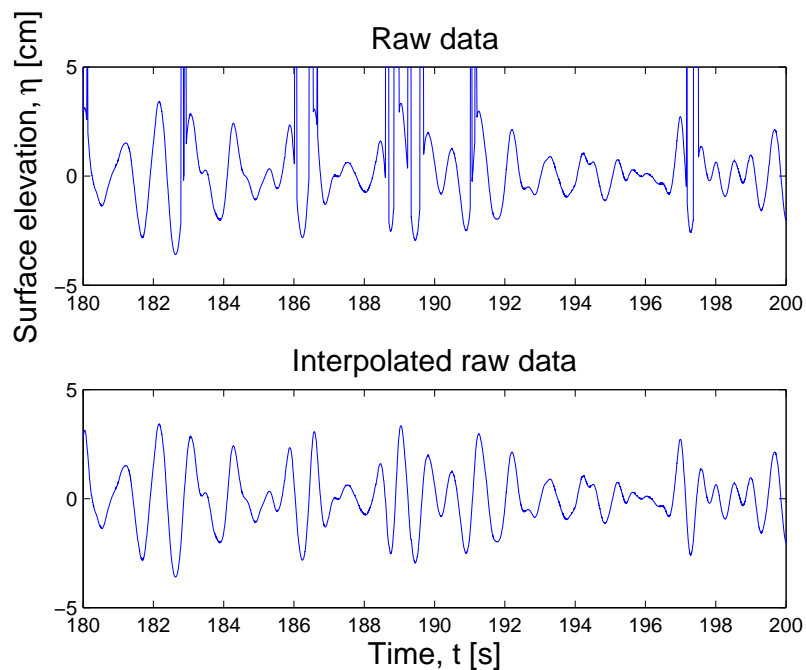


Figure 8: Cubic interpolation.

A linear and spline interpolation were also tested and figure 9 shows the result of the linear, cubic and spline interpolations on the time interval between 188.4 s and 189.8 s from figure 8. The linear interpolation works quite well on the sharp transition between the dropout points and the measured surface elevation, but it

gives a rather straight approximation of the surface elevation between the troughs and the crests. In comparison, the cubic interpolation does not work that well on the sharp transitions between the interpolation points and the surface elevation, especially in the transition on the down-crossing at 189.3 s. On the other hand, the curvature of the cubic interpolation probably gives a more realistic approach to the surface elevation. With the spline interpolation the transition between the interpolation points and the measured surface elevation is sharper compared to the other methods.

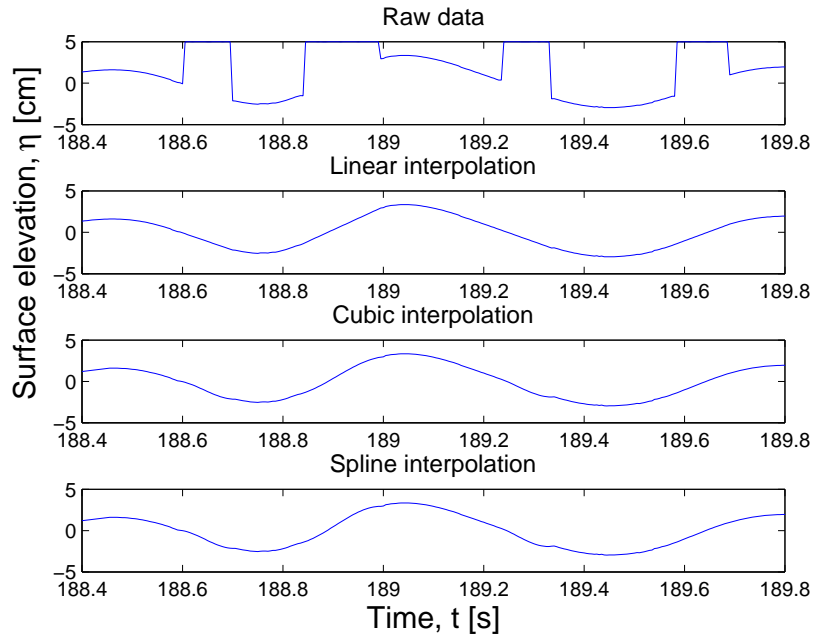


Figure 9: Linear, cubic and spline interpolations.

An extensive data material of dropouts were investigated in this manner. Although it might seem that the linear interpolation gives the smoothest approximation in this case, it was concluded that the cubic interpolation in many other cases gave a better approximation since it included a more curved surface. On this background we decided to apply the cubic interpolation. In any case the three interpolation methods gave very similar results and as we will see later larger interpretation uncertainties were connected to measurement errors caused by dropouts in the surface elevation data.

5.2 Filter

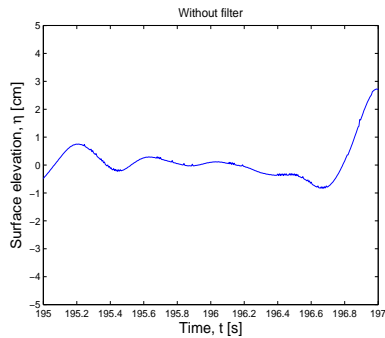


Figure 10: Without filter.

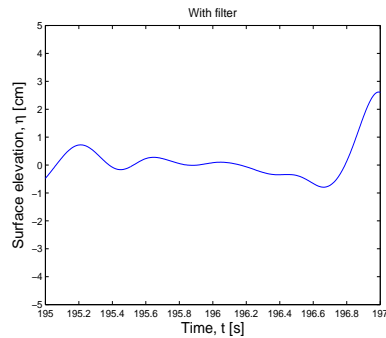


Figure 11: With a Savitzky-Golay smoothing filter.

Figure 10 shows a 2 s abstract of the interpolated raw data between 195 s and 197 s in figure 8. No filter has been applied to the data, and the noise appears as small prickers on the measured surface elevation. Figure 11 shows the corresponding filtered data. A weak Savitzky-Golay filter has been applied to the surface elevation data. Savitzky-Golay filters are least square smoothing filters, which typically are applied for signals with relatively broad bandwidth, excluded noise. With reference to Matlab© instructions, the Savitzky-Golay filter should perform better than standard averaging FIR filters, which tend to filter out a significant portion of the frequency content in the signal, excluded noise.

The Savitzky-Golay filter was used to filter the relatively weak noise in the measured surface elevation data which was applied for the spectral estimates for the (k, ω) -spectra in chapter 7. Even though it was promised that the Savitzky-Golay filter should not affect the wavenumber and frequency content we could suspect the opposite. To test this suspicion a strong filter was tested on the measured (k, ω) -spectra in subsections 7.1.5 and 7.2.2. The results are presented in Appendix E.3.1 and shows that a strong filter reduces the magnitude of the spectral energy density but does not seem to effect the spectral distribution in the spectra significantly.

The spectral energy density in the frequency and wavenumber spectra at the end of this chapter, are obtained from the filtered surface elevations and are in addition filtered with a weak filter to smooth out the spectral curves. The weak filter applied should ensure that the spectral distributions are not affected significantly by the filter. The spectral energy density in the (k, ω) -spectra in chapter 7 has not been additionally filtered.

5.3 Startup effects

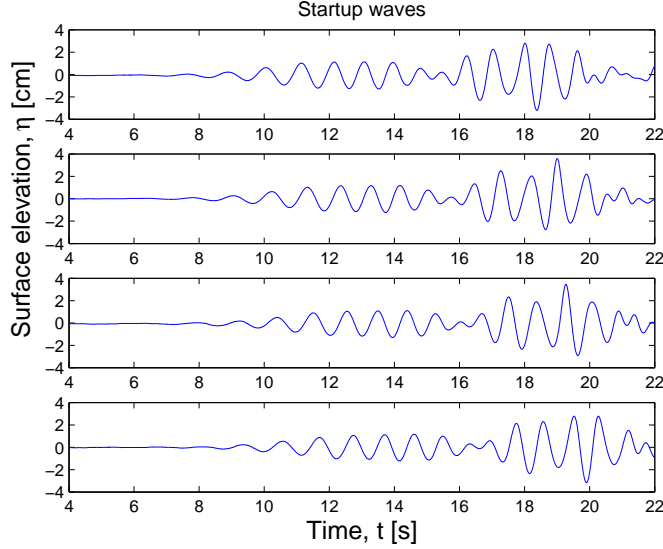


Figure 12: Startup waves.

Figure 12 shows the startup waves in series 1, the first waves in the wave train. The waves were measured at $D = 8.1, 8.4, 8.7$ and 9.0 m by the first four probes in the stationary array with sixteen probes (upper to lower plot respectively). We see that for the first wave in the wave train it takes about $1/2$ s to propagate from the first probe P1 (upper plot) to the fourth probe P4 (lowest plot). As mentioned, for the spectral estimate the first minute of the time series was removed to avoid transient startup effects and to contemplate the wave field after it had stabilized for some time.

5.4 Repeatability

The (k, ω) -spectra which shows the measured dispersion relations in chapter 7 are obtained from synthetic array measurement techniques which are heavily relying on that the wave fields which are generated from the wave generator are repeatable. In this section the repeatability of the time series is investigated in more detail. The section is divided into two subsections. In the first subsection the repeatability when the wave field is generated with the absorbing beach at the far end of the wave flume is investigated, and in the second subsection a similar investigation is when the wave field is generated with the reflecting wall at the far end of the wave flume.

5.4.1 With absorbing beach

Figure 13 shows two independent repetitions, blue and red, of time series 1 measured from the same positions with the absorbing beach operational at the far end of the wave flume. The waves were measured at $D = 8.1, 8.4, 8.7$ and 9.0 m by the first four probes P1-P4 in the stationary array with sixteen probes respectively. Upper to lower time series in the figures shows the measurements from P1-P4 respectively. The time series shows the last 20 s of surface elevation which is applied

for the spectral estimate.

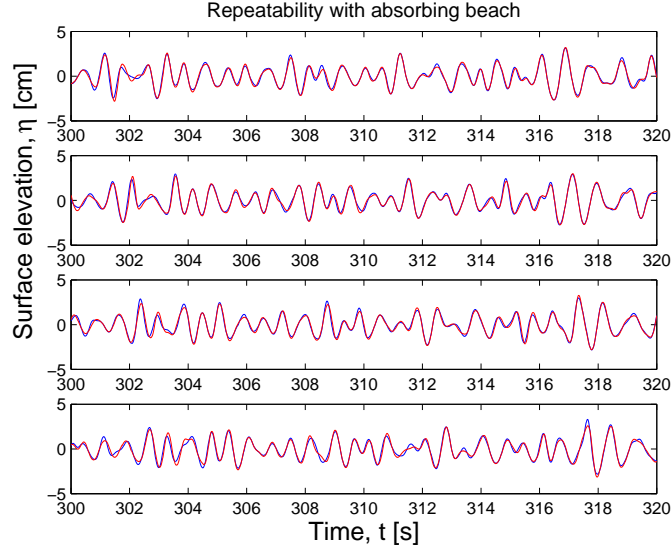


Figure 13: Repeatability with absorbing beach.

With the absorbing beach operational we see that the time series are quite identical, and only small differences occur. It is interesting to see that after 300 s (5 minutes) of wave generation, the two time series are approximately repeatable.

In each experiment where the dispersion relation is measured, the relative errors between two time series are tabulated together with the corresponding (k, ω) -spectra in chapter 7. The relative errors between the two time series measured by P1 - P4, presented above, are given in table 1. The relative errors are estimated from the entire measured time series (340 s). The beginning and the end of the time series are also quite identical. The repetition errors are relatively small.

D [m]	Rel. error at P1 [%]	P2[%]	P3 [%]	P4 [%]
8.1	2.57	2.85	1.90	3.39

Table 1: Repetition errors with absorbing beach.

By comparing the interpolated and filtered time series with the corresponding time series of the raw data, it does not seem that any of the differences in the surface elevations are caused by errors in the interpolation of the dropouts. In figure 14 the upper two time series are the raw data series and the interpolated/filtered series measured by P1. The lower two time series are the corresponding series measured by P2. In figure 15 the upper two time series are the corresponding series measured by P3, and the lower two time series the corresponding series measured by P4. The raw data from P4 did not contain any dropouts in the time interval.

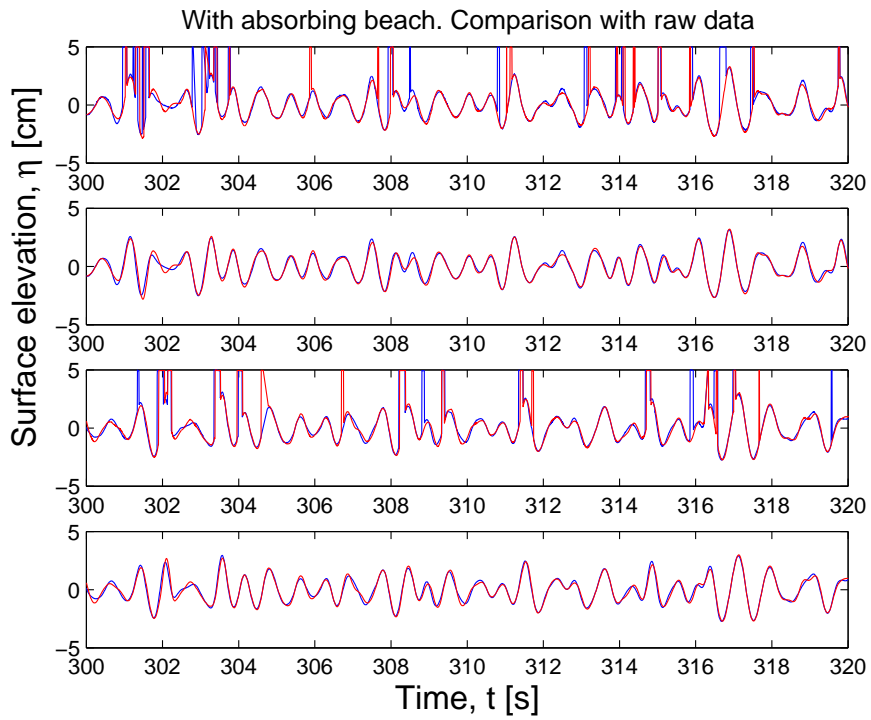


Figure 14: With absorbing beach. Comparison with the raw data. P1 and P2.

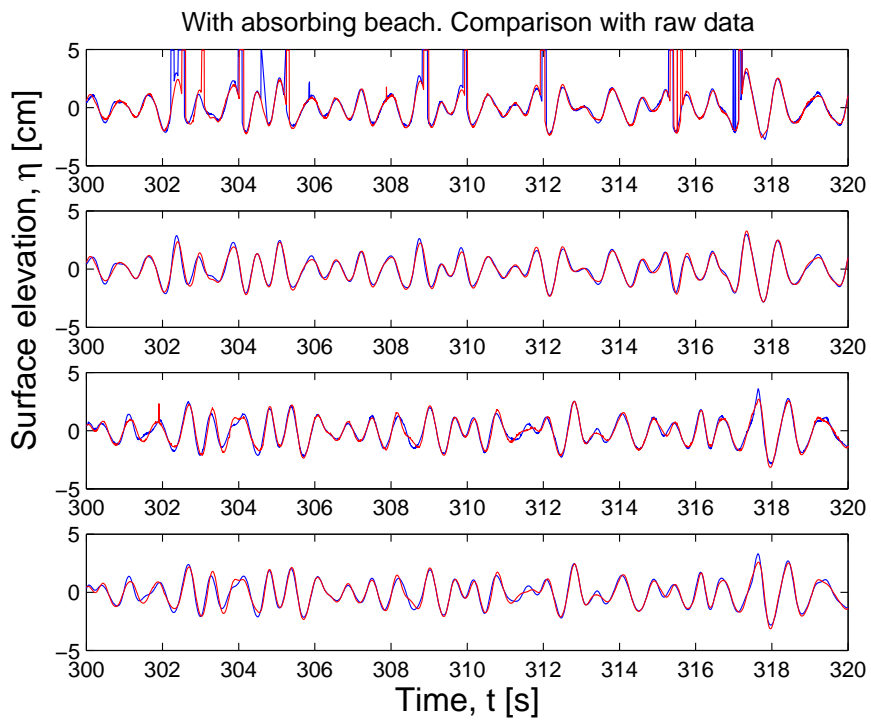


Figure 15: With absorbing beach. Comparison with the raw data. P3 and P4.

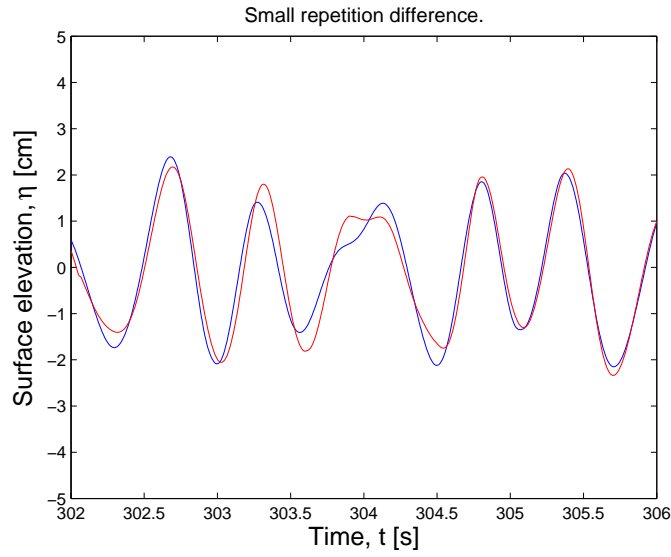


Figure 16: Small difference in surface elevation measured by P4.

A difference in the surface elevation which is not caused by errors in the interpolation occurs after 304 s of wave generation in the measurement by P4. This type of repetition difference could be caused by a nonlinear wave-wave interactions.

5.4.2 With reflecting wall

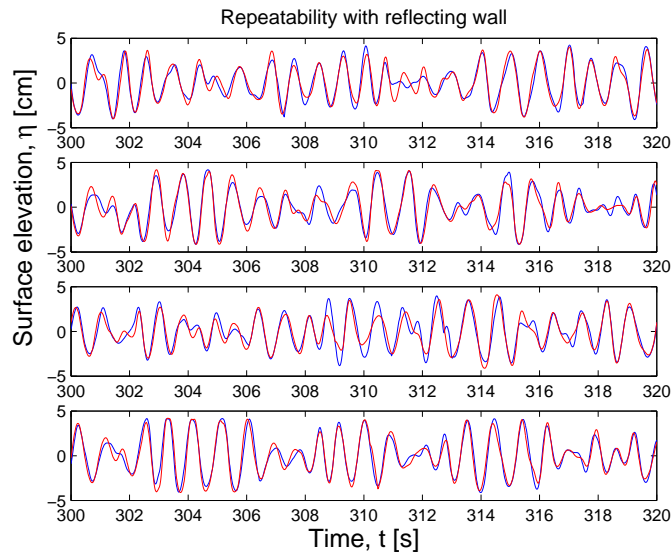


Figure 17: Repeatability with reflecting wall.

With the reflecting wall at the far end of the wave flume the wave series are less identical, and the differences between two independent time series measured from the same positions are larger (figure 17). With the reflecting wall the wave field generally consists of larger and steeper waves, compared to when the wave field is

generated with the absorbing beach. The wave field was measured by P1-P4 from the exact same positions as in the previous subsection.

The relative errors between the two time series measured with the reflecting wall operational are given in table 2. The errors are higher compared with the experiments done with the absorbing beach.

D [m]	Rel. error at P1 [%]	P2[%]	P3 [%]	P4 [%]
8.1	5.29	7.10	5.68	8.23

Table 2: Repetition errors with reflecting wall.

The raw data from the wave field generated with the reflecting wall is presented in figure 19 and 20 in a similar manner as in the previous section. The raw data is quite messy, and dropouts appear frequently. It is possible that some of the differences in the repetitions are caused by measurement errors in the probes when dropouts extend over entire crests or troughs. This is exemplified in figure 18 which shows a large error in the measurement between 310-314 s by P1. In the raw data we see that the probe probably does not measure the trough after 311 s of wave generation.

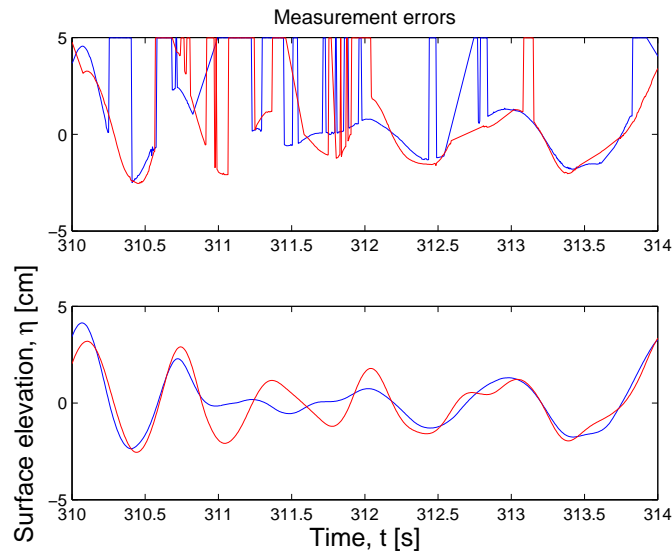


Figure 18: Measurement error by P1.

When this type of measurement error occurs the interpolation method logically interpolates over and past the trough. As we will see in chapter 7 rather large relative repetition errors occurred in some of the experiments. A comparison with the raw data similar to the analysis in this section showed that these errors are caused by a few large measurement errors and consequently errors in the interpolations which in sum contribute to relatively larger errors in these time series.

The raw data presented here are not of a good quality and we might have to expect that at least a few relative large errors will be present in the processed data when the wave field is generated with the reflecting wall. To carry out experiments efficiently, it would at least have been too time-consuming to manually manipulate

and fix the raw data. With this approach a quite large uncertainty connected to the interpretation of the raw data surface elevation would also have been introduced.

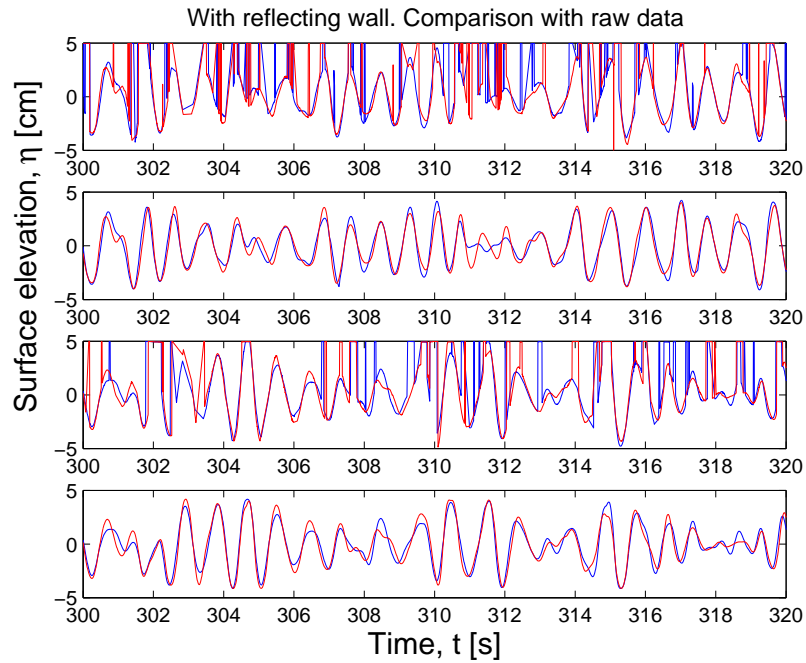


Figure 19: With reflecting wall. Comparison with the raw data. P1 and P2.

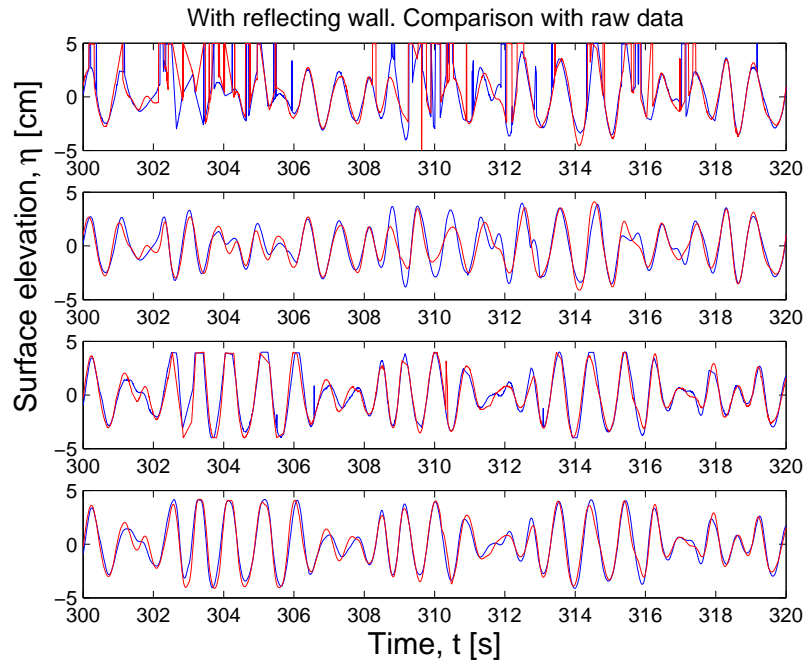


Figure 20: With reflecting wall. Comparison with the raw data. P3 and P4.

5.5 Time tapering

Any attempt to apply Fourier analysis on a finite series will impose periodic boundary conditions. We might be concerned if the periodic boundary conditions also impose discontinuities in functional values and derivatives at endpoints. We wish that the periodic extension should be smooth, so that the Fourier analysis is not polluted by the effect of lacking smoothness at the endpoints. In general, this type of data pollution results in spectral distributions which often are referred to as spectral leakage.

A signal processing method for preventing spectral leakage is tapering. The time series is multiplied with a tapering function so that there is a smooth transition from the end of the time series to the beginning of the time series. We agreed on making a tapering function which is equal to one most over so that it preserves most of the time series. At both ends however there should be a function that gradually declines, or tapers to zero. The end points can be composed from conventional window functions implemented in Matlab[®]. Figure 21, 22, and 23 shows a Blackman, Blackman-Harris, and Nuttall window, which is a family of windows that could be applied at the endpoints of the tapering function. The Nuttall window is a minimum four term Blackman-Harris window and produces slightly lower sidelobes than the Blackman-Harris window, Nuttall and Albert (1981). We chose to apply the Nuttall window at both ends of the tapering function. Our self composed tapering function is quite similar to the Tukey window already implemented in Matlab[®].

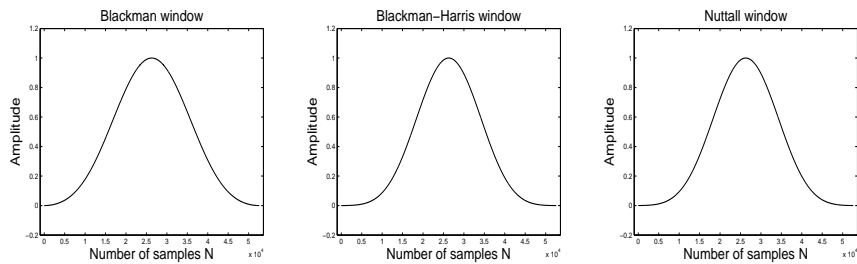


Figure 21: Blackman window. **Figure 22:** Blackman-Harris window. **Figure 23:** Nuttall window.

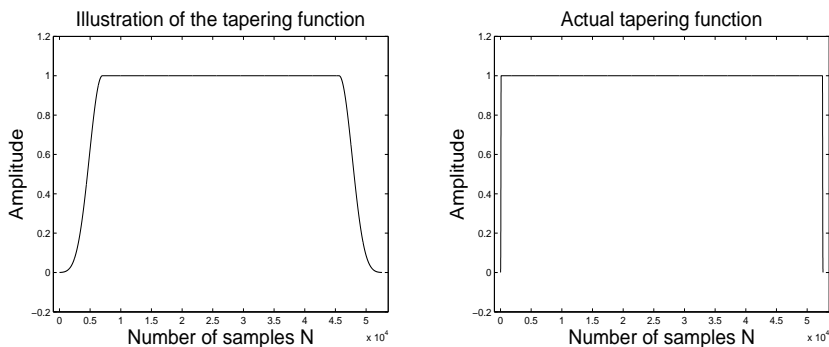


Figure 24: Illustration of the tapering function. **Figure 25:** Actual tapering function applied to taper the time series.

Figure 24 shows an illustration of the tapering function which is applied to

taper the time series. The tapering function consists of ones in the middle, and symmetrically at each end is the Nuttall window. The width of the Nuttall window region can be chosen freely. For illustrating purposes each half of the Nuttall window stretches over 7000 samples, so to see the gradual declination from one to zero. Figure 25 shows the actual tapering function used to taper the time series. Each half of the Nuttall window stretches over 100 samples ($1/2$ s), and the number of samples which are modified by the tapering function is 0.0038% of the total number of samples $N = 52000$ in the time series after that the start and the end of the series have been removed.

Figure 26 shows the tapered start of time series 1 from a synthetic array measurement where $M = 96$ time series were measured, and figure 27 shows the corresponding tapered end of the time series. Each element in the time series have been multiplied with the corresponding elements from the tapering function shown in figure 25. Within half a second the time series gradually declines, or tapers to zero at both ends. Appendix E.2.2 shows the effect of time tapering in a (k, ω) -spectrum measured from $M = 96$ measurement positions and how the spectral leakage is reduced.

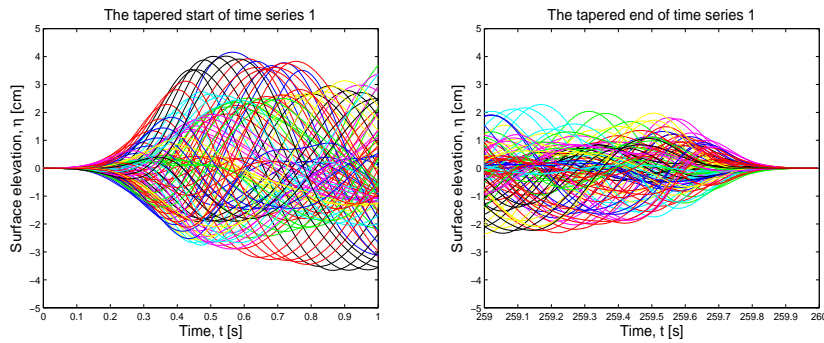


Figure 26: Tapered start of $M = 96$ time series. **Figure 27:** Tapered end of $M = 96$ time series.

5.6 Space tapering

The space series consisted of much fewer data points than the time series and in the experiments the length of the space series varied between $M = 24$ and 256. From the synthetic array based on the stationary array with four probes the space series only consisted of $M = 24$ data points. With such few data points we carefully tried to develop tapering methods in space which hopefully would affect the spatial data series as little as possible. The first tapering method consisted of adding a zero to the end of the space series. The zero works as a declination point for the first and the last data points in the space series. As a bi-effect, the array is prolonged by Δx and $\Delta k = 2\pi/L$ decreases slightly which in turn gives a slightly higher resolution along the wavenumber axis.

The second method consisted of, in addition to adding a zero, multiplying the first and the last data points in the space series with a $1/2$ to obtain a more gradual declination towards the zero. Other more extended versions of these methods were also tested. In Appendix E.1.2 these space tapering methods are presented in more detail in connection with the (k, ω) -spectra measured from $M = 24$ measurement positions and shows how the spectral leakage, resulting from the spatial data series, is reduced.

Later in the experimental work the synthetic arrays based on the stationary

array with sixteen probes increased the number of elements in the space series to $M = 96, 128, 192$ and 256 . For these space series a space tapering function similar to the time tapering function in section 5.5 was developed. The space tapering function consists of ones in the middle and a Nuttall window symmetrically at both ends. A zero is added to the end of the tapering function to correspond to the added zero at the end of the space series. The first and the last elements in the Matlab© generated Nuttall window are zeros. These have been deleted and replaced by ones in the middle window region. The width of the Nuttall window region can be chosen freely. Figure 28 shows the amplitude of the space tapering function with each Nuttall window region consisting of ten elements. Different widths of the Nuttall window regions were tested. In chapter 7 the different percentage widths relative to the entire space series are presented in connection with the (k, ω) -spectra. Appendix E.2.3 shows the effect of different space tapering Nuttall window widths in a range of (k, ω) -spectra measured from $M = 96$ measurement positions and how the different window widths affect the spectral leakage.

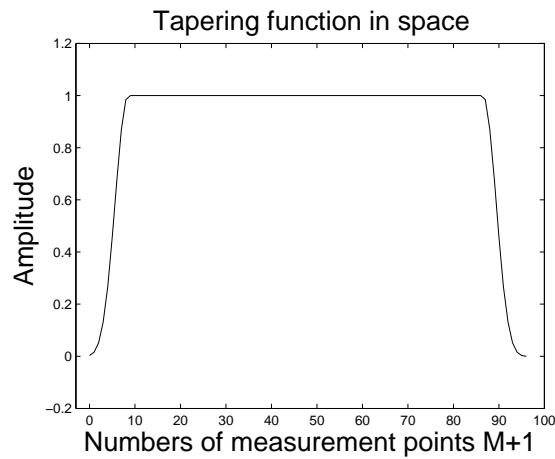


Figure 28: The space tapering function.

5.7 Frequency and wavenumber spectra

5.7.1 Frequency spectra

Figure 29 shows the two-sided ($\omega \gtrless 0$) linear frequency spectrum $S_{(2)}(\omega)$ estimated from the measured series 1 by P1, with the absorbing beach at the far end of the wave flume and with a water depth of $h = 0.60$ m. The time series have been time tapered and the spectral energy density curve is smoothed with a weak Savitzky-Golay filter. The frequency spectra for series 1-6 on $h = 0.35$ m are presented in Appendix D.1.

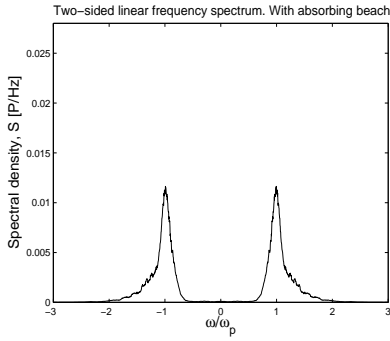


Figure 29: Linear frequency spectrum with absorbing beach.

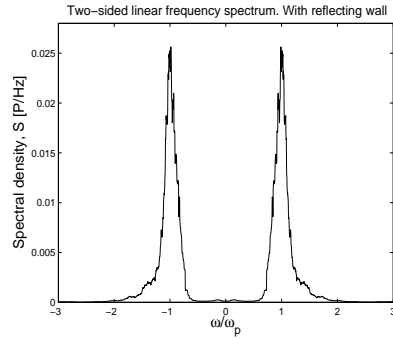


Figure 30: Linear frequency spectrum with reflecting wall.

Figure 30 shows the two-sided linear frequency spectrum $S_{(2)}(\omega)$ estimated from the time series measured with the reflecting wall at the far end of the wave flume. The axes are equal in figure 29 and 30 and $-3\omega_p \leq \omega \leq 3\omega_p$. The spectral energy density increases when the absorbing beach is substituted by the reflecting wall.

Figure 31 and 32 shows the one-sided logarithmic frequency spectra $S(\omega) = 2S_{(2)}(\omega)$ from figure 29 and 30, respectively. The axes are equal and $0 \leq \omega \leq 4\omega_p$. For series 1 the peak angular frequency was estimated to be $\omega_p = 6.80 \text{ rads}^{-1}$.

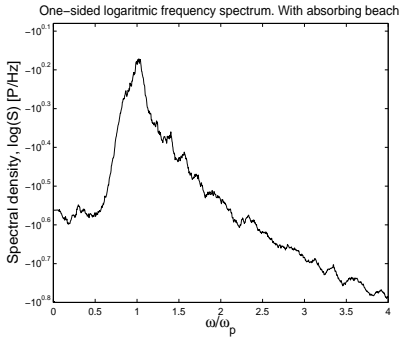


Figure 31: Logarithmic frequency spectrum with absorbing beach.

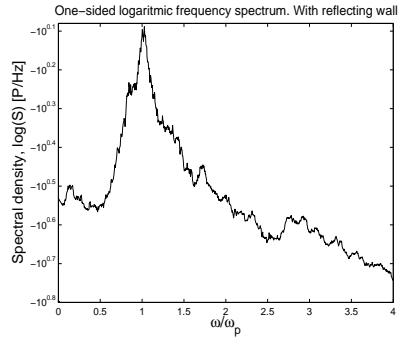


Figure 32: Logarithmic frequency spectrum with reflecting wall.

The peak wavenumber is estimated from a convergent fixed point iteration of the linear dispersion with ω_p as initial input. For series 1 on $h = 0.60$ m the peak wavenumber was estimated to be $k_p = 4.74 \text{ radm}^{-1}$.

In figure 31 and 32 we see that above the peaks there are additional smaller peaks. In both spectra the smaller peaks at $2 \times \omega_p$ and $3 \times \omega_p$ should be connected to enhanced intensities from the second and third order higher harmonic bounded waves. The second order difference appears as enhanced intensities below the peak. We see that the energy from the second order difference is intensified and peaks at lower angular frequency components when the absorbing beach is substituted by the reflecting wall. The third order higher harmonics are also enhanced when the absorbing beach is substituted by the reflecting wall.

Other smaller peaks in the spectra are possible connected to dynamic nonlinear wave interactions in the wave flume. From the wave field generated with the absorbing beach two additional peaks appear between ω_p and $2\omega_p$ and from the wave field generated with the reflecting wall in particular one additional peak appear between ω_p and $2\omega_p$.

In table 3 the peak angular frequencies ω_p and the peak wavenumbers k_p for all the wave fields generated with the absorbing beach operational are summarized. The peak wavenumber estimated from the linear dispersion relation changes slightly from 5.00 radm^{-1} to 4.74 radm^{-1} when the water depth is increased from $h = 0.35 \text{ m}$ to $h = 0.60 \text{ m}$. The peak angular frequency is similar on the two water depths. The 1.7% increasement of the original input file for series 1, as presented in Appendix B.1.1, had a similar angular frequency distribution and peak angular frequency as the original series.

Wavefield time series	h [m]	ω_p [rads $^{-1}$]	k_p [radm $^{-1}$]
Series 1	0.60	6.80	4.74
Series 1	0.35	6.80	5.00
Series 2	"-	5.60	3.71
Series 3	"-	5.55	3.66
Series 4	"-	5.50	3.60
Series 5	"-	6.70	4.90
Series 6	"-	6.40	4.54
Series 1, 1.7% increase	"-	6.80	5.00

Table 3: ω_p and k_p with absorbing beach.

For series 1 on $h = 0.60 \text{ m}$ the non-dimensional depth $k_p h = 2.84$ which is roughly deep water ($\tanh(k_p h) \approx 0.99$). For series 1 on $h = 0.35 \text{ m}$, $k_p h = 1.75$ which is regarded as more intermediate water depth, ($\tanh(k_p h) \approx 0.94$), but not far from deep water.

Given k_p the peak wavelength $\lambda_p = 1.33 \text{ m}$. For series 1 on $h = 0.60 \text{ m}$, the peak wave phase speed $c_p = \sqrt{g\lambda_p}/2\pi = 1.44 \text{ m/s}$ and the group velocity $c_g = 0.72 \text{ m/s}$. During the generation of the five and a half minutes time series 1, the group velocity travels $D_g = c_g T = 237.60 \text{ m}$, so during a generation of the time series the group velocity, according to linear theory, travel along the length of the wave flume $237.60/21.60 \approx 11$ times.

5.7.2 Bandwidth

A dimensional analysis was performed to gain information about the normalized bandwidth $\delta^* = \delta/\omega_p$. δ is the half width at half peak intensity of the linear angular frequency spectrum. Figure 33 shows an illustration of the bandwidth for the two-sided linear frequency spectrum, estimated from the absorbing beach wave

field, in figure 29 in the previous section, for $\omega \geq 0$. In figure 33, δ is equal to half the distance between the points marked with \times where $S_{(2)}(\omega)$ intersects the horizontal line $S_{(2)\max}/2$. A similar illustration is given for the two-sided linear frequency spectra for series 1-6 generated on $h = 0.35$ m in Appendix D.2. These spectra were used to find the normalized bandwidths for all the time series.

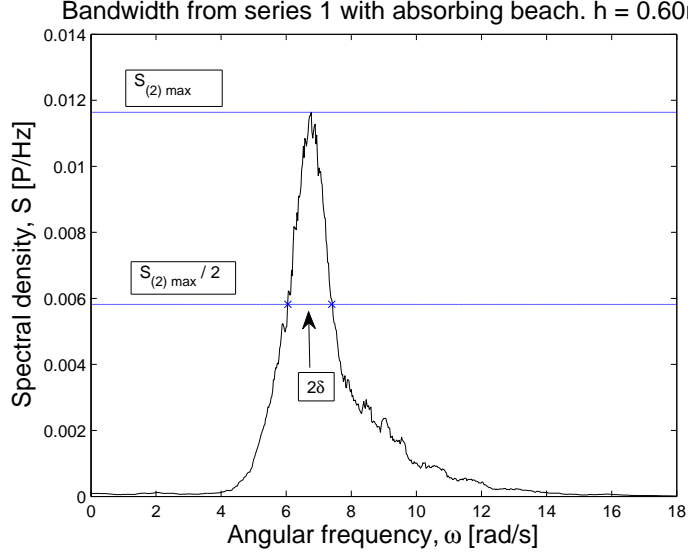


Figure 33: Bandwidth from series 1 with absorbing beach.

The estimated values for δ and δ^* for all the time series are tabulated in table 4. Series 1 provides the narrowest normalized bandwidth. The normalized bandwidth of series 1 increases slightly when the water depth is increased to 0.60 m.

Wavefield time series	h [m]	δ [rads ⁻¹]	$\delta^* = \delta/\omega_p$ [-]
Series 1	0.60	0.6885	0.1013
Series 1	0.35	0.6750	0.0993
Series 2	-"	0.6160	0.1100
Series 3	-"	0.5920	0.1067
Series 4	-"	0.6160	0.1120
Series 5	-"	0.7130	0.1064
Series 6	-"	0.6890	0.1077

Table 4: δ and δ^* with absorbing beach.

Figure 34 shows an illustration of the bandwidth for the two-sided linear frequency spectrum estimated from the reflecting wall wave field in figure 30 in the previous section, for $\omega \geq 0$. The spectral energy density for each angular frequency component close to the peak increases, and relative to the frequency spectrum estimated from the absorbing beach wave field, the spectrum is broader. However, the normalized bandwidth does not change relatively to $S_{(2)\max}$. The half width and the normalized bandwidth was in fact estimated to have the same values as for the spectrum from the absorbing beach wave field.

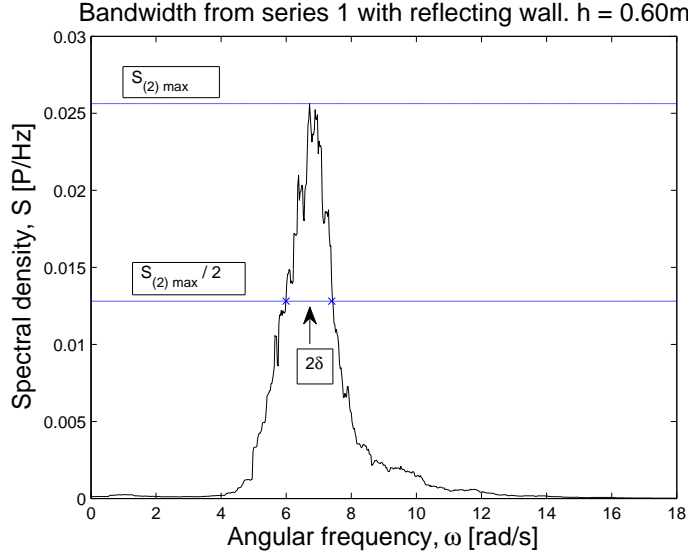


Figure 34: Bandwidth from series 1 with reflecting wall.

5.7.3 Wavenumber spectra

Figure 35 and 36 show the two-sided linear wavenumber spectra $k \in \mathbb{R}$ from the absorbing beach and reflecting wall wave fields, respectively. The axes in the two figures are equal. The wave fields were measured over a propagation length of $L = 19.2$ m, from $M = 256$ positions, on $h = 0.60$ m. The time and space series used for the spectral estimate have been time and space tapered. In the figures all the $N = 52000$ space series of length $M = 256 + 1$, with added space tapering zero, have been plotted, to obtain a visual estimate of the spectral peak.

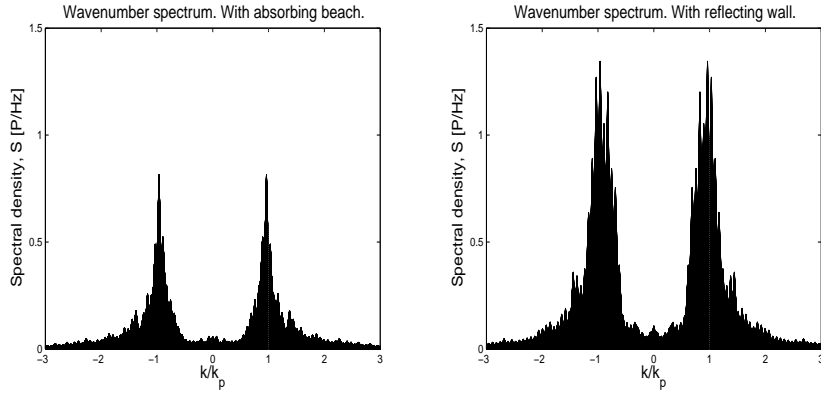


Figure 35: Linear wavenumber spectrum with absorbing beach.

Figure 36: Linear wavenumber spectrum with reflecting wall.

We see that the wavenumber spectral energy density increases when the absorbing beach is substituted by the reflecting wall. The vertical white line is the peak wavenumber k_p estimated from the linear dispersion relation. We see that the spectral peak is just below k_p in both spectra. This may indicate that the peak wavenumber estimated from the spectra is lower than the peak wavenumber k_p es-

timated from linear wave theory.

An interesting analysis could be to determine the RMS wavenumbers k_{RMS} and compare these wavenumbers with linear wave theory wavenumbers k_{LWT} . Unfortunately, the author did not find time to do this analysis before the deadline. It is a consistent feature that RMS wavenumbers estimated from measurement data tend to get much larger than the corresponding linear wave theory wavenumbers when the frequency drops below the spectral peak, contrary to the behaviour above the peak, where the two wavenumbers are more similar, Krogstad and Trulsen (2010).

5.8 Steepness

The wave steepness $\epsilon = k_p a_c$ where $a_c = \sqrt{2\langle \eta^2 \rangle}$ is the characteristic amplitude of the wave field. The estimated values for a_c and ϵ from series 1 with the absorbing beach operational on $h = 0.60$ m are tabulated in table 5. The values for series 1-6 and the modified series on $h = 0.35$ m are also tabulated.

a_c and ϵ increase when the water depth is increased to $h = 0.60$ m. This is most likely caused by that wave breaking in shallower water reduces the amplitudes.

The analysis of series 1-6 on $h = 0.35$ m showed that series 1 was the wave field which provided the largest steepness. By modifying series 1, a_c and ϵ increased slightly. Although the modified series 1 gave a steeper wave field we decided to apply the original series 1 for the latest experiments.

Wavefield time series	h [m]	a_c [m]	ϵ [-]
Series 1	0.60	0.0200	0.0946
Series 1	0.35	0.0174	0.0871
Series 2	-?-	0.0226	0.0839
Series 3	-?-	0.0200	0.0733
Series 4	-?-	0.0173	0.0624
Series 5	-?-	0.0153	0.0751
Series 6	-?-	0.0174	0.0789
Series 1, 1.7% increase	-?-	0.0179	0.0893

Table 5: a_c and ϵ with absorbing beach.

Table 6 shows the values for a_c and ϵ for series 1 with the reflecting wall operational at the far end of the wave flume. We see that a_c and ϵ increases when the absorbing beach is substituted by the reflecting wall.

Wavefield time series	h [m]	a_c [m]	ϵ [-]
Series 1	0.60	0.0271	0.1286

Table 6: a_c and ϵ with reflecting wall.

For our experiments we requested to have the largest possible ratio between the steepness ϵ and the normalized bandwidth δ^* , to increase nonlinear effects in the wave fields. A narrow bandwidth is also an assumption for the (M)NLS equations in Krogstad and Trulsen (2010). We intended to have a δ^* which could be comparable to the relative spectral width σ_x applied in the numerical simulations. As mentioned in chapter 2 a Gaussian bell-shaped wavenumber spectrum with scaled RMS width

$\sigma_x = 0.1$ was used in the numerical simulations. The value for our δ^* estimated from the JONSWAP frequency spectrum is therefore not directly convertible to σ_x .

Table 7 presents the values for ϵ/δ^* for series 1-6 generated on water depths 0.35 m and 0.60 m. Series 1 provides the largest ratio for ϵ/δ^* . After this dimensional analysis we decided to use series 1 for the latest experiments.

Wavefield time series	h [m]	ϵ/δ^* [-]
Series 1	0.60	0.9176
Series 1	0.35	0.8448
Series 2	-"-	0.7627
Series 3	-"-	0.6870
Series 4	-"-	0.5571
Series 5	-"-	0.7058
Series 6	-"-	0.7326

Table 7: Table of parameters for ϵ/δ^* .

5.9 Sampling

In general many samples are taken in time due to the high sampling frequency of the ultrasonic probes and few samples are taken in space due to the limitations of the spatial array. The sampling frequency in time is $f_s = 200$ Hz, and $\Delta t = 1/200$ s = 0.005 s. The Nyquist sampling theorem (Johnson and Dudgeon 1993) states that reconstruction of a signal is possible when the sampling frequency exceeds twice the maximum frequency in the sampled signal. Thus we should be able to reconstruct waves with frequencies up to $f_{N/2} = 100$ Hz or angular frequencies up to $\omega_{N/2} = 2\pi f_{N/2} \approx 628$ rads^{-1} . $\omega_{N/2}$ is the Nyquist angular frequency, half of the angular sampling frequency. Given the peak angular frequency $\omega_p = 6.8$ rads^{-1} , we should be able to reconstruct waves with angular frequencies up to about $92 \times \omega_p$. Thus we should be able to reconstruct water surface waves with much higher frequencies than those of interest in the laboratory wave flume.

In space the sampling theorem can be expressed in connection with the distance Δx between our probes;

$$\Delta x \leq \frac{1}{2}\lambda = \frac{1}{2} \frac{2\pi}{k} = \frac{\pi}{k}. \quad (49)$$

To be able to reconstruct the peak wavenumber $k_p = 4.74$ radm^{-1} on $h = 0.60$ m, $\Delta x \leq \pi/k_p = 66$ cm. This criterion is satisfied by the stationary array ($\Delta x = 30$ cm). With $\Delta x = 5$ cm, which was the smallest distance between the probes applied in the synthetic array measurements,

$$k = \frac{\pi}{\Delta x} = 62.83 \text{ radm}^{-1}. \quad (50)$$

Thus, we are able to reconstruct waves with wavenumbers up to about $13 \times k_p$. In the longest synthetic array measurement with $L = 19.2$ m, $M = 256$ and $\Delta x = 7.5$ cm we should be able to reconstruct waves with wavenumbers up to $9 \times k_p$ and wavelengths down to

$$\lambda = \frac{2\pi}{9 \times k_p} \approx 0.15 \text{ m}. \quad (51)$$

This is quite satisfactory considered that the peak wavelength is $\lambda_p \approx 1.33$ m.

$N = 52000$ samples were applied for the spectral analysis, and the corresponding time series was $T = 260$ s long. This gives

$$\Delta\omega = \frac{2\pi}{T} = \frac{2\pi}{260\text{s}} \approx 0.024 \text{ rads}^{-1}. \quad (52)$$

With $L = 19.2$ m,

$$\Delta k = \frac{2\pi}{L} \approx 0.33 \text{ radm}^{-1}. \quad (53)$$

Thus we have a much better resolution in the frequency domain than in the wavenumber domain. This is in particular seen in the (k, ω) -spectra measured with the $L = 1.2$ m long synthetic array in chapter 7. In the (k, ω) -spectra measured with the $L = 19.2$ m long synthetic array the result is more satisfactory. However we should be aware of how the contour levels of the spectral energy density is plotted on the (k, ω) -grid. In practice each integer wavenumber in the grid contains only about three Δk and each integer angular frequency contains about fourty-one $\Delta\omega$.

The numerical simulations in Krogstad and Trulsen (2010) covers 140 peak wavelengths and about 400 wave periods, of which the last 170 periods have been used to obtain the spectrum estimate. The peak wave period in the experiments with series 1 on $h = 0.60$ m is,

$$T_p = \frac{2\pi}{\omega_p} = 0.92 \text{ s}. \quad (54)$$

Compared with our experiments this gives,

$$L = 140\lambda_p = 186.2 \text{ m} \quad (55)$$

and

$$T = 400T_p = 368 \text{ s}. \quad (56)$$

Thus the simultaneous coverage in space applied in the experiments of $L = 19.2$ m is only about 10% of the simultaneous coverage in the numerical simulations and covers only about 14 peak wavelengths. The measurement time T is about the same with $T = 340$ s in the experiments. With T_p from the experiments substituted into the time $T = 170T_p = 156.4$ s used to obtain the spectral estimate in the numerical simulations, we see that the time used to obtain the laboratory spectral estimate $T = 260$ s could have been reduced more significantly.

6 Current

The random wave fields are run so long that an additional return flow in the wave flume is induced, Grue et al. (2003). A return flow below the wave group generally reduces the velocities below mean water level and increases the velocities near the crest. The return flow is caused by the radiation stress, Longuet-Higgings and Stewart (1963). In order to identify a possible Doppler shift on the dispersion surface in the (k, ω) -spectra presented later in chapter 7 we were interested in determining the wave-induced current.

Grue et al. (2003) applied PIV equipment to perform precise measurements of the instantaneous velocity field below crest. The wave-induced current is however a slowly varying velocity field, and recordings of long time series of the wave field using PIV is prevented by limitations of the apparatus. As pointed out in Grue et al., they were unable to measure the induced drift velocities in the wave flume using PIV equipment. On this background Grue et al. speculated that a relatively pronounced slowly varying return velocity was responsible for an additional tilt in the velocity profiles observed in the late part of the experiments in some of the series.

Instead of using PIV we attempted to measure the slowly varying wave-induced current with the acoustic Doppler current profiler ADCP, presented in section 3.3, which in contrast to the PIV equipment does not have any limitations on records of long time series.

The chapter is divided into two sections. Section 6.1 presents the ADCP measurements which were done with the absorbing beach at the far end of the flume, and section 6.2 presents the ADCP measurements which were done when the absorbing beach was substituted by the reflecting wall. The measured data for the u component of the fluid particle velocity $\mathbf{U} = (u, v, w)$ are presented. The fluid particle velocities were measured from series 1 on a water depth of $h = 0.60$ m. The analysis shows that the wave-induced velocities in general increase when the absorbing beach is substituted by the reflecting wall.

The estimated values for the u current speed is substituted into the theoretical linear dispersion relation with current advection in equation (14), and in chapter 7 the theoretical solution which includes the estimated value for u has been plotted with white curves. Since for the spectral estimates the first minute and the last twenty seconds of the surface elevation time series were removed this has also been done for the analysis of the current series so that the data material for the current and the possible Doppler shift on the dispersion surface are comparable. The ADCP was started manually so the removed samples do not correspond exactly to the removed samples in the surface elevation time series. It is expected that this does not introduce large uncertainties since the wave-induced current is a slowly varying phenomena. It has been important to remove the first minute of the current time series because in the early part of the series the current is probably weaker than in the late part of the series and this would have led to a underestimation compared to the possible Doppler shift of the spectral energy density on the dispersion surface.

We have attempted to apply a statistical analysis for the ADCP data. The fluid velocity fields were measured in a range of positions along a vertical line from the bottom of the flume to the top near the deepest trough. For each measurement position the mean of the time series of the $u(t)$ speed and the standard deviations $\sigma = \sqrt{\langle u^2 \rangle}$ have been estimated. A deviation from the mean of u could possible be caused by the slowly varying wave-induced current.

It turned out that it was a quite complicated task to determine an estimate for u . The time series of $u(t)$ contains velocities which mostly are induced by the rapidly moving waves in the form of the well-known spiral movements of the fluid particles in the water, Newman (1977). In addition, these velocities have a lon-

gitudinal drift; the well-known Stokes' drift, Newman (1977). Even at the bottom the spiral movements were observed both in the flume during the experiments and in the velocity data. This leads to a much larger estimate for σ than what would be representable for the wave-induced flow only. In general it is very difficult to distinguish between the slowly varying wave-induced current and other velocities which are induced by the rapidly varying individual waves in the wave field.

6.1 With absorbing beach

Figure 37 shows an abstract from the time series of u at the lowest measurement position at a water depth of $z = -52.5$ cm for the last 30 s which are used for the statistical analysis in this section. We see that near the bottom fluid particles move with oscillatory motions similar to motions of fluid particles near the surface.

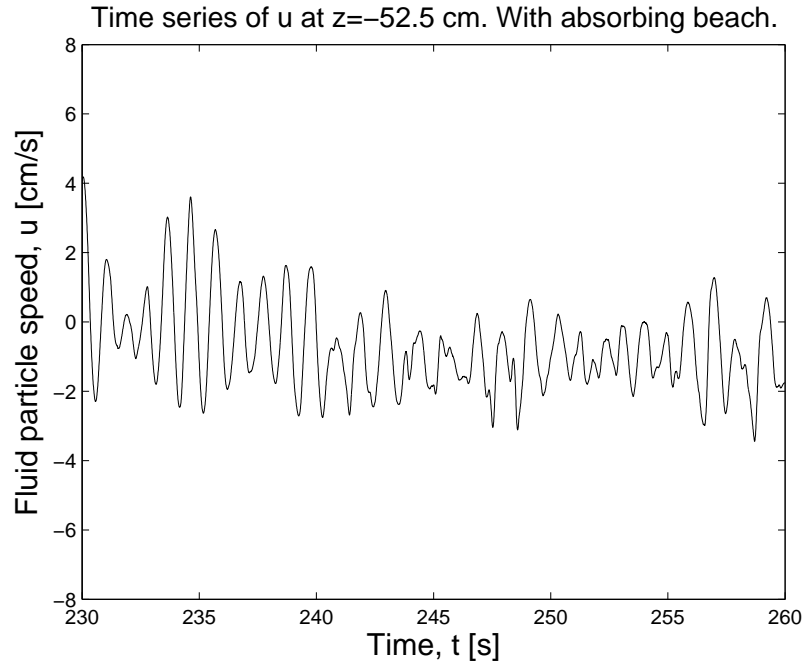


Figure 37: Time series of u at $z = -52.5$ cm. With absorbing beach.

Two or three repetitions of the time series were measured at positions along a vertical line from the bottom to the free surface. Table 8 presents the arithmetic mean of the mean velocities \bar{u} and the standard deviations $\sigma = \sqrt{\langle u^2 \rangle}$ from all repetitions. Three repetitions were done close to mean water level and at $z = -45.0$ cm and $z = -52.5$ cm.

z [cm]	Nr. of repetitions	$\langle \bar{u} \rangle$	$\langle \sigma \rangle$
-6.0	3	0.36	7.12
-10.0	3	-0.14	6.65
-14.0	3	0.32	4.84
-20.0	2	-0.74	3.71
-25.0	2	-0.83	3.10
-30.0	2	-0.97	2.67
-35.0	2	-1.01	2.33
-40.0	2	-0.64	2.26
-45.0	3	-0.51	1.66
-49.5	2	-0.34	1.55
-52.5	3	-0.37	1.53

Table 8: Arithmetic means of \bar{u} and σ . With absorbing beach.

In figure 38 and 39 the data points $(z, \langle \bar{u} \rangle)$ and $(z, \langle \sigma \rangle)$ have been plotted. The lower black horizontal line corresponds to the bottom in the flume, the upper dark blue horizontal line corresponds to the mean water level $z = 0$, and the light blue regular wave corresponds to a wave which has an amplitude equal to the amplitude of the deepest trough ($z = -4.21$ cm) in the wave field generated with the absorbing beach. Note that 39 is not a velocity profile in the sense that it is the arithmetic means of the positive standard deviations in each measurement point that have been plotted.

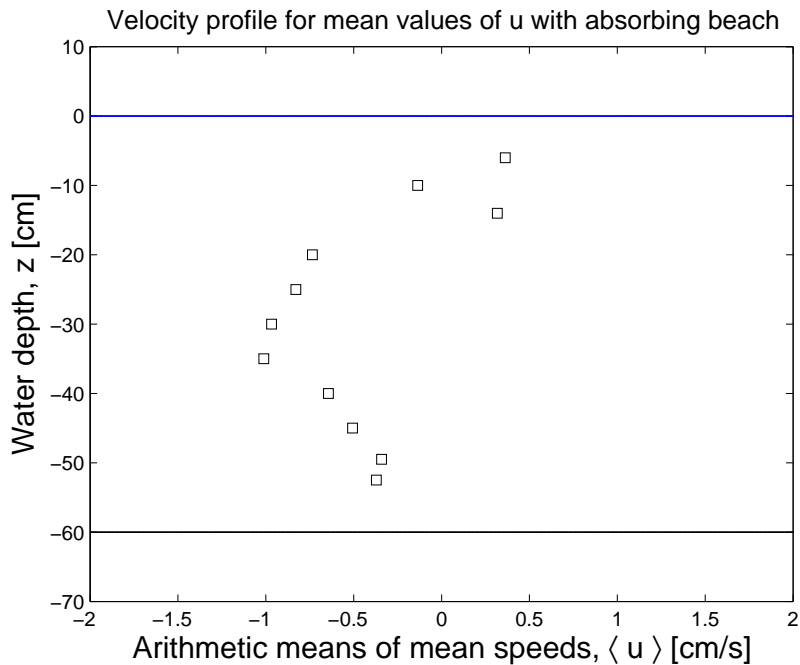


Figure 38: Arithmetic means of the mean speeds $\langle u \rangle$.

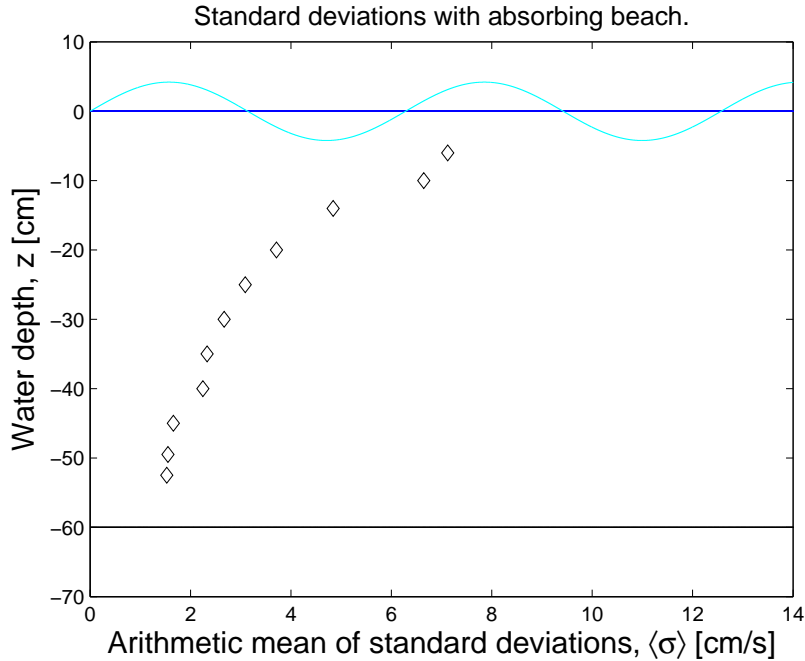


Figure 39: Arithmetic means of the standard deviations $\langle \sigma \rangle$.

The mean values of u seem to form a profile with maximum speeds u at $z = -35$ cm. It was observed during the experiment that fluid particles near the bottom have a drift in the negative x -direction, so this is in accordance with the obtained data in the middle and near the bottom of the profile. The three measurements near the surface deviate from the other measurements.

There is uncertainty connected to the results at the upper three measurement positions near the surface. At these measurement positions the ADCP was positioned in a vertical position. The x coordinate on the ADCP which was used to measure u when the ADCP was placed in a vertical position could have a slightly different setting than the z coordinate which was used to measure u when the ADCP was in a horizontal position for all the other measurements. It is not possible to calibrate the x, y and z coordinates on the ADCP. Ideally the same coordinate position should have been used for all measurements in the profile, but this was not possible with the rack equipment available in the laboratory.

The analysis shows that the standard deviations of u are largest near the mean water level, and decrease towards the bottom. However, from this analysis we are not able to tell much about the current induced velocity, since most standard deviations in the fluid velocities results from the rapidly varying movements of the individual waves in the wave field.

6.2 With reflecting wall

Figure 40 shows an abstract from the time series of u at a water depth of $z = -52.5$ cm for the last 30 s which are used for the statistical analysis in this section. We see that the velocities increase in comparison with figure 37 when the absorbing beach is substituted by the reflecting wall. The axes in figure 37 and 40 are equal.

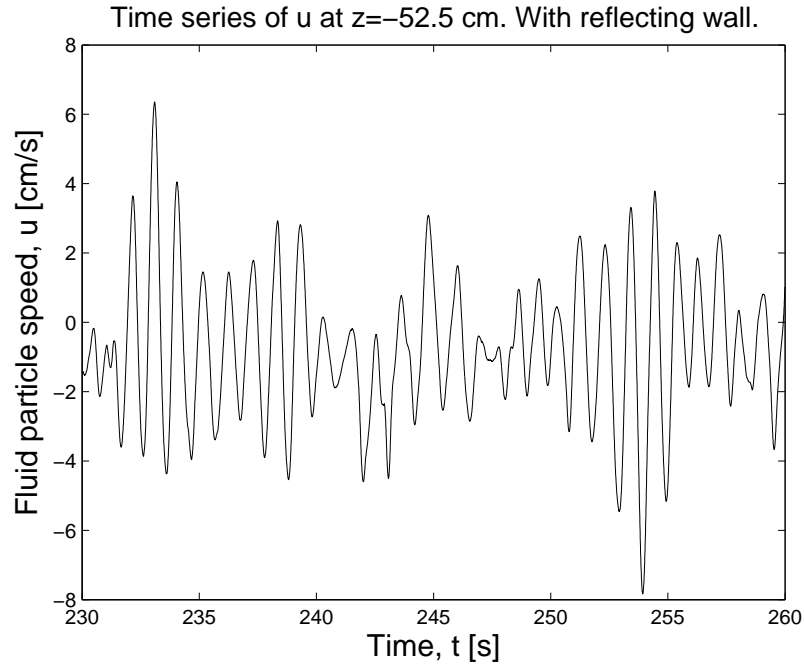


Figure 40: Time series of u at $z = -52.5$ cm. With reflecting wall.

Table 9 presents the arithmetic mean of the mean velocities \bar{u} and the standard deviations $\sigma = \sqrt{\langle u^2 \rangle}$ from all repetitions with the reflecting wall at the far end of the flume. Three repetitions were done close to mean water level and at $z = -45.0$ cm and $z = -52.5$ cm.

z [cm]	Nr. of repetitions	$\langle \bar{u} \rangle$	$\langle \sigma \rangle$
-6.0	3	0.19	13.63
-10.0	3	0.10	9.94
-14.0	3	0.28	7.86
-20.0	2	-1.02	5.90
-25.0	2	-0.98	4.92
-30.0	2	-1.05	4.17
-35.0	2	-1.06	3.60
-40.0	2	-1.05	3.12
-45.0	3	-0.78	2.70
-49.5	2	-0.80	2.54
-52.5	3	-0.57	2.39

Table 9: Arithmetic means of \bar{u} and σ .

In figure 41 and 42 the data points $(z, \langle \bar{u} \rangle)$ and $(z, \langle \sigma \rangle)$ have been plotted. The light blue regular wave corresponds to a wave which has an amplitude equal to the amplitude of the deepest trough ($z = -4.47$ cm) in the wave field generated with the reflecting wall.

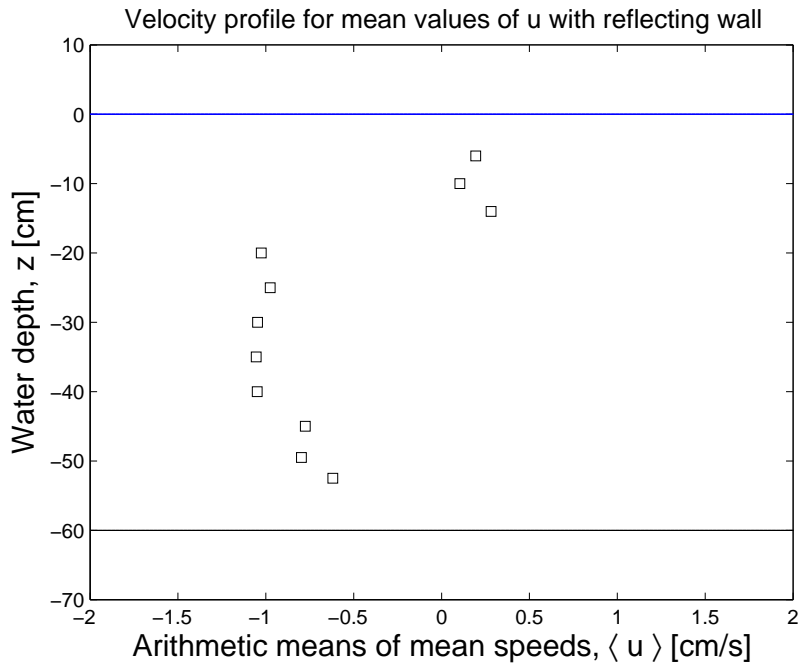


Figure 41: Arithmetic means of mean speeds $\langle u \rangle$.

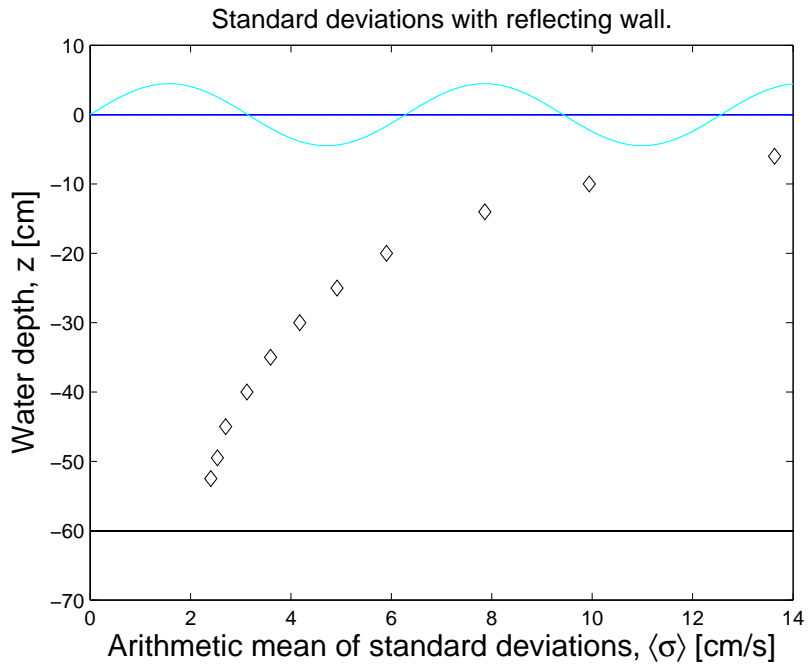


Figure 42: Arithmetic means of the standard deviations $\langle \sigma \rangle$.

The mean values of $\langle u \rangle$ seem to form a more vertical profile with higher deviations from the mean in the middle and at the bottom of the profile. As in the

previous section there are uncertainties connected to the upper three measurements near the surface. The standard deviations of $\langle u \rangle$ are larger when the absorbing beach is substituted with the reflecting wall. The reflected waves contribute to more rapidly varying movements of the fluid particles.

For the wave fields which are generated with the absorbing beach the article Grue et al. (2003) might give expedient information about several single events in the wave fields. In Grue et al. section 4.3 it is pointed out that the additional tilt in the velocity profiles appears especially for the wave field in series 2. Quoted from the article: "The waves in series 2 are 40% longer than those in series 1 and 4. The wave velocity (group velocity) is correspondingly 20% higher and the estimated Stokes drift 60% higher. Correspondingly, an estimated return velocity beneath the wave is 120% higher in series 2 than in series 1 and 4. An addition to the return flow due to a finite length of the tank is set up quicker and becomes stronger in series 2 than in 1 and 4."

The velocity profiles for series 1 in figure 4 and for series 2 in figure 6 in section 4.3 in Grue et al. (2003) shows that the additional tilt is smaller and almost neglectable for series 1 compared to series 2. Thus, we could based on the PIV measured single events late in the time series in Grue et al. (2003), speculate that the wave induced current velocity in series 1 is relatively weak with the absorbing beach operational.

The standard deviations $\langle \sigma \rangle$ which are partly estimated from the rapidly varying movements of the waves in the wave field are probably much larger than the wave-induced fluid velocities. The mean velocities $\langle \bar{u} \rangle$ might give an indication of a slowly varying deviation from the mean, but there are uncertainties connected to the calibration of the ADCP.

For illustrating purposes we have plotted the theoretical solution of the linear dispersion relation with current advection from equation (14) in the (k, ω) -spectra in chapter 7 with $u = 1$ and 2 cm/s. The author believes that an estimate for u probably is lower than these values both with the absorbing beach and the reflecting wall operational. This believe is reasoned by the observation of fluid particles, near the bottom of the wave flume during the experiments, which tend to drift at a very slow speed.

7 Measured dispersion relations

This chapter presents the (k, ω) -spectra, the directly measured dispersion relations, from the wave fields generated in the wave flume. The chapter shows the evolution of measurements done over relatively short propagation lengths L with few measurement points M to measurements done over longer propagation lengths with more measurement points. The analysis of the (k, ω) -spectra has been the main focus of the work in the thesis, and therefore a quite comprehensive presentation of the spectra is given in this chapter.

The chapter is divided into two sections. Section 7.1 presents the experiments which were done with the absorbing beach at the far end of the flume, and section 7.2 presents the experiments which were done with installations at the far end of the flume which provided more reflection of incoming waves from the wave generator. The spectra in subsection 7.1.5 and 7.2.2 were measured over the longest propagation length L with most measurement points M . These spectra will be commented more extensively.

The (k, ω) -spectra from series 1-6 were measured with the synthetic array based on the stationary array with four probes. For this relatively short array, with $L = 1.2$ m, the information about the spectral energy density distribution in the (k, ω) -spectra is rather limited by the low resolution along the wavenumber axis. Therefore only the (k, ω) -spectrum from series 1 is presented in subsection 6.1.1., and the (k, ω) -spectra from series 2-6 are presented in Appendix E.1.1.

Since $N = 52000$ time samples were used for the spectral analysis, ω was distributed over a relatively long range of integer angular frequencies. As a consequence it was quite CPU time consuming to produce contour plots of the entire (k, ω) -domains. This problem was solved by reducing the number of contour levels. A presentation of how contour levels were chosen and how the CPU time was reduced is given in Appendix E.2.1.

Different methods for tapering in time and space were gradually developed in parallel with the experimental work. The effect of tapering in time and space in the (k, ω) -spectra is also presented in the Appendix. For the synthetic array based on the stationary array with four probes the effect of space tapering in the (k, ω) -spectra is presented in Appendix E.1.2 and for the synthetic array based on the stationary array with sixteen probes the effect of time and space tapering in the (k, ω) -spectra is presented in Appendix E.2.2 and Appendix E.2.3.

7.1 With absorbing beach

7.1.1 $L = 1.2$ m and $M = 24$

The (k, ω) -spectrum presented in this subsection was measured with the early stage experimental arrangement presented in chapter 3.1 with the synthetic array based on the stationary array with four probes. This array was the first developed synthetic array with $M = 24$ measurement positions over a short propagation length of $L = 1.2$ m, and with a spatial resolution of $\Delta x = 5$ cm. Given the relatively short array length, $\Delta k = 2\pi/L$ becomes relatively large and the information in the (k, ω) -spectra from the array is rather limited by the low resolution along the wavenumber axis. The (k, ω) -spectra measured from series 2-6 and the additional modified series are therefore presented in Appendix E.1.1, and only the (k, ω) -spectrum measured from series 1 is presented in this subsection.

Figure 43 shows the linear (k, ω) -spectrum, the directly measured dispersion relation from series 1 on $h = 0.35$ m. The wave field was measured at $D = 9.0$ m from the wave generator.

The wavenumber and angular frequency axes are discretized both for positive

and negative values. The lower black curve is the linear dispersion relation, and the upper black curve is the second order dispersion shell. The data-points \circ are the peak points (k_p, ω_p) , and $(2k_p, 2\omega_p)$ and the dashed line is a reference line through the peak points.

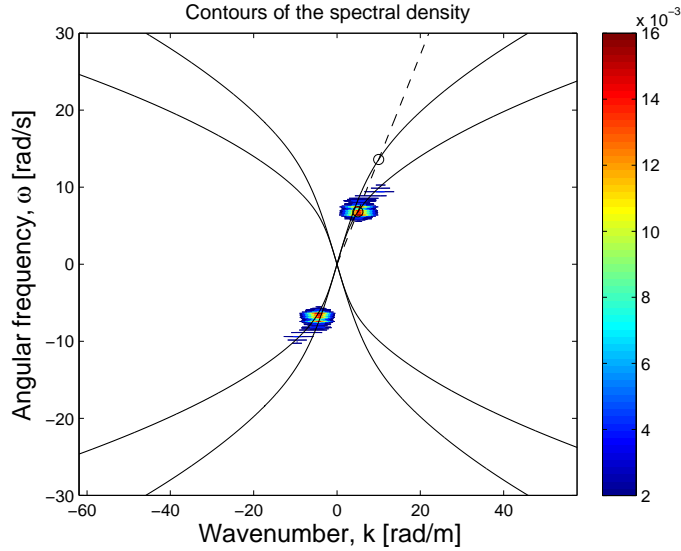


Figure 43: Linear (k, ω) -spectrum. $L = 1.2$ m and $M = 24$.

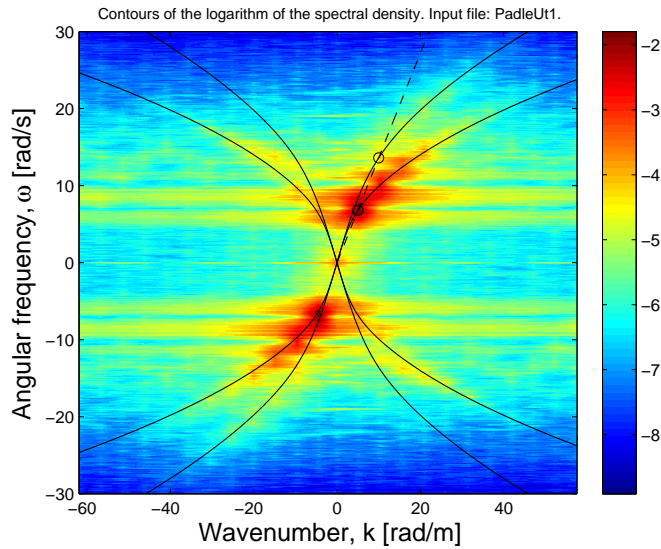


Figure 44: Logarithmic (k, ω) -spectrum. $L = 1.2$ m and $M = 24$.

In figure 43 the contours of the spectral energy density $S(k, \omega)$ are plotted on a linear scale which gives rather limited information about the spectral energy density distribution. We solved this problem by instead plotting the contours of

$\log_{10} S(k, \omega)$ which magnifies the relatively small scalar values of $S(k, \omega)$. The contour lines are defined on a self composed logarithmic scale which is based on only the scalar values around the maximum of $\log_{10} S(k, \omega)$ to reduce the CPU-time significantly. This procedure is explained in more detail and exemplified in Appendix E.2.1.

Figure 44 shows the contour plot of $\log_{10} S(k, \omega)$. The low resolution along the wavenumber axis results in the impression that the logarithm of the spectral energy density $\log_{10} S(k, \omega)$ has a relatively broad distribution. Although, we can see that the spectral energy density is distributed along the linear dispersion relation, and the second order dispersion shell. The spectral energy density for reflected waves is also identified for positive angular frequencies $\omega \geq 0$ and negative wavenumbers $k \leq 0$. The reflection from the absorbing beach was more pronounced at $h = 0.35$ m, than at $h = 0.60$ m, because at $h = 0.35$ m the waves hits the vertical grid edge which the beach is buildt upon.

The broad horizontal distributions out from the peak area is spectral leakage caused by discontinuities in the transition between the end and the start of the spatial data series. At this stage of the experimental work we had developed a quite primitive method for tapering in space, and Appendix E.1.2 shows and presents the effect of tapering in space in the (k, ω) -spectrum from series 6.

As mentioned earlier the (k, ω) -spectra are obtained from synthetic array measurement techniques which are heavily relying on that the wave fields which are generated from the wave generator are repeatable. The relative errors between two independent repetitions of the time series measured from the same position are summarizes in table 10. The relative errors are small, with the exception of larger errors in the experiment with series 2 . In this series measurement errors in the raw data surface elevation were observed, and figure 45 shows a measurement error after 311 s of wave generation. The dropout in the first repetition (blue) extends over the entire crest, but in the second repetition (red) the probe marginally manages to measure the crest successfully. As a consequence of the measurement error the interpolation method interpolates between the points under the crest. Similar errors contributes to a rapid increasement in the overall repetition errors of series 2. The waves in series 2 were rather long and high and relatively many waves had crests and troughs extending to the boundaries of the measurement window of the probes $-5 < z < 5$. Since series 2 was not applied for later work we will not go into further detail.

Wavefield time series	Rel. error at P1 [%]	P2[%]	P3 [%]	P4 [%]
Series 1	3.72	3.10	1.57	2.56
Series 2	10.23	12.35	12.60	10.88
Series 3	1.03	1.54	0.92	0.59
Series 4	1.41	1.40	1.37	1.47
Series 5	0.38	0.33	1.08	0.66
Series 6	0.67	0.57	0.74	0.56
Series 1 modified	2.24	2.50	2.31	2.44

Table 10: Repetition errors. $L = 1.2$ m and $M = 24$.

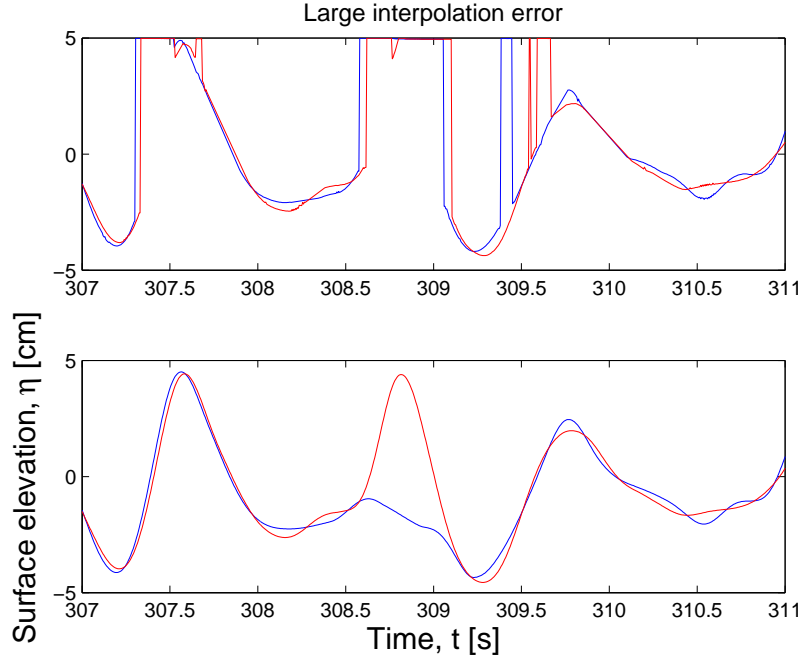


Figure 45: Large interpolation error after 311 s of wave generation in series 2.

7.1.2 $L = 4.8$ m and $M = 96$

The (k, ω) -spectra presented in this subsection were measured with the later stage experimental arrangement presented in chapter 3.3 with the synthetic array based on the stationary array with sixteen probes. This synthetic array had $M = 96$ measurement positions over a propagation length of $L = 4.8$ m, and a spatial resolution of $\Delta x = 5$ cm. This gave a smaller Δk , and a better resolution along the wavenumber axis compared to the synthetic array in subsection 7.1.1.

The (k, ω) -spectra in this subsection were measured from series 1 on $h = 0.60$ m. The measurements of the wave field were performed at three different locations along the wave flume to investigate if the effect of reflected waves from the absorbing beach (figure 46) was dependent on the measurement distance from the absorbing beach. The experiments were performed at distances $D = 3.0, 8.1,$ and 15.2 m from the wave generator. In the experiment $D = 15.2$ m from the generator, the last surface elevation measurement $\eta_{n,95}$ was done 1.30 m from the vertical edge of the absorbing beach.

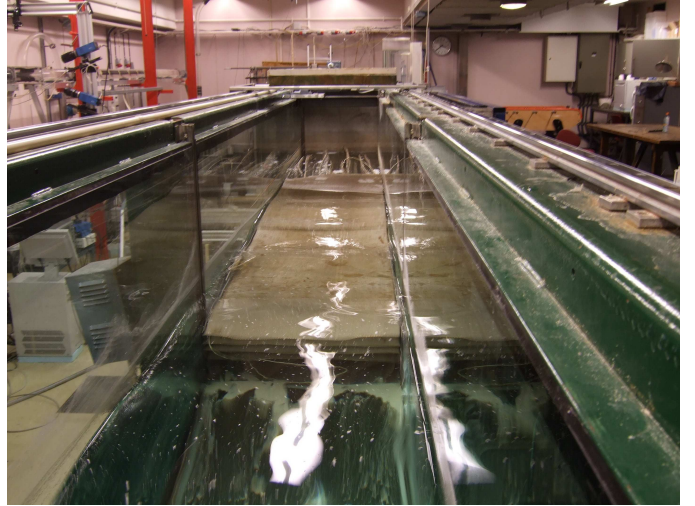


Figure 46: Absorbing beach at $h = 0.60$ m.

Figure 47, 48 and 49 shows the directly measured dispersion relation at $D = 3.0, 8.1,$ and 15.2 m respectively. Apparently we can see more clearly an indication that the spectral energy density is distributed along the linear dispersion relation curve and the second order dispersion shell. An interesting feature which now also

appears in the (k, ω) -spectra is the second order difference harmonic below the spectral peak. The spectral energy density from the third order bounded waves is also possible identified around $(3k_p, 3\omega_p)$ over the second order dispersion shell curve.

The broad horizontal distributions out from the peak area is spectral leakage caused by discontinuities in the transition between the end and the start of the spatial data series. At this stage of the experimental work the space tapering function presented in chapter 5.6 was developed. Appendix E.2.3 shows the effect of the space tapering function in the (k, ω) -spectrum from figure 47 for a range of different Nuttall window end widths.

The (k, ω) -spectra in figure 47-49 showed that the appearance of reflected waves was relatively weak and independent of whether the wave field was measured far from the absorbing beach or close to the absorbing beach. On this background three more experiments were performed with a steeper and harder beach constructed from a wooden plate. The (k, ω) -spectra from these experiment are presented in section 7.2.1 and shows that the spectral energy density from reflected waves increases.

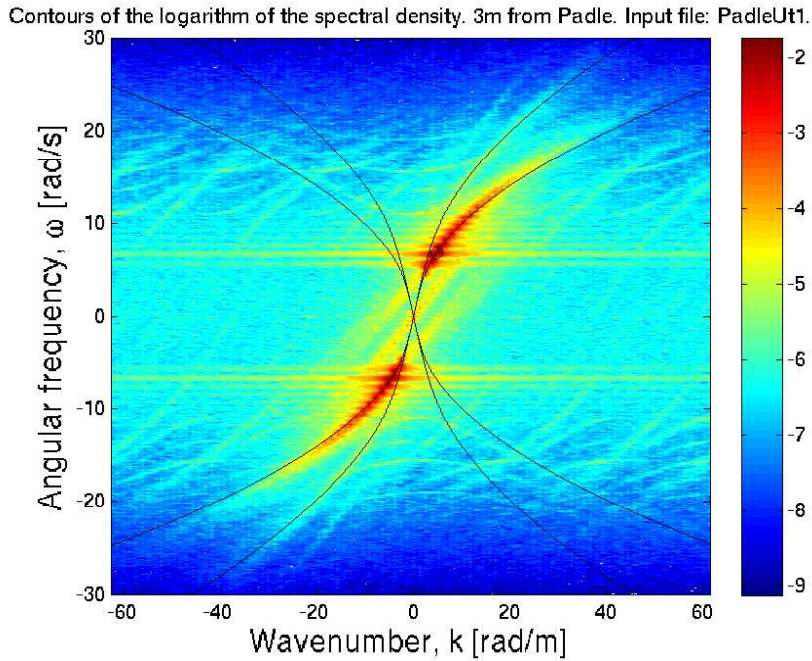


Figure 47: (k, ω) -spectrum. $L = 4.8$ m and $M = 96$. $D = 3.0$ m.

Contours of the logarithm of the spectral density. 8.1m from Padle. Input file: PadleUt1.

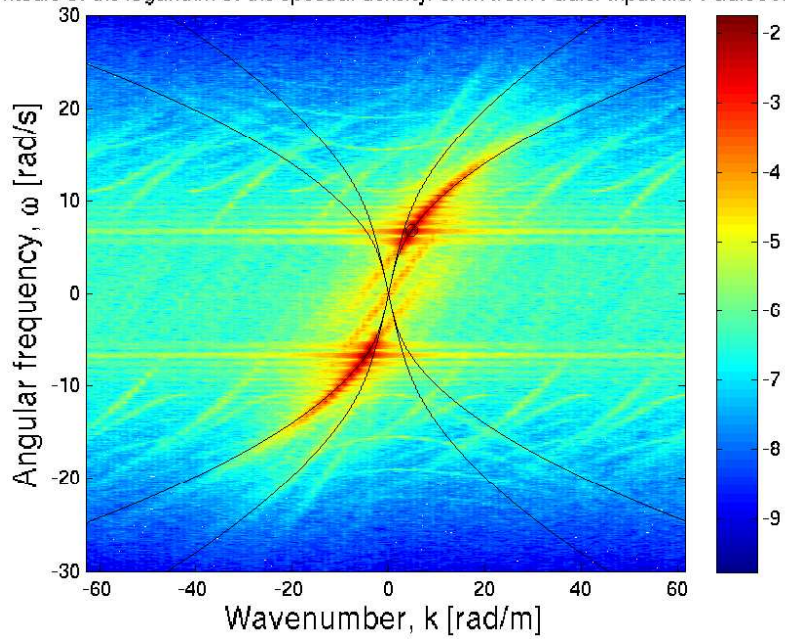


Figure 48: (k, ω) -spectrum. $L = 4.8$ m and $M = 96$. $D = 8.1$ m.

Contours of the logarithm of the spectral density. 15.2m from Padle. Input file: PadleUt1.

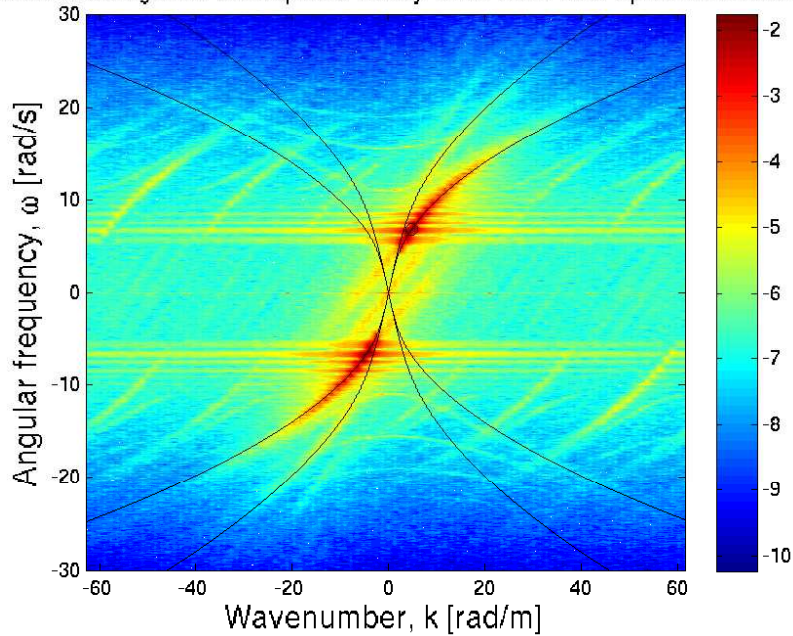


Figure 49: (k, ω) -spectrum. $L = 4.8$ m and $M = 96$. $D = 15.2$ m.

Smaller intensities to the right and the left of the peak intensity with similar shapes as the peak intensity appear especially in the (k, ω) -spectra in figure 48 and

49. These are most likely caused by small errors in either the distance Δx between the probes, or the 5 cm displacement between each synthetic measurement. These distances were set carefully, but since the Fourier transform is discrete, the transform is relatively sensitive to small errors. It is possible that small or larger repetition errors in the wave fields also appear as intensities in Fourier space. The numerical model in chapter 8 will be applied as a tool to test Δx errors.

Table 11 shows the values for the characteristic amplitude a_c and the wave steepness $\epsilon = a_c k_p$ at the three locations D from the wave generator. a_c and ϵ seem to have the largest values at the surface elevation 3.0 m from the wave generator, and lower values 8.1 m and 15.2 m from the generator. The relative size of higher order spectra depends on the steepness of the wave field, Krogstad and Trulsen (2010), but the relatively small differences in ϵ here do not seem to have any significant effect on the spectral distributions along the dispersion shells.

h [m]	D [m]	a_c [m]	ϵ [-]
0.60	3.0	0.0211	0.0998
"-	8.1	0.0200	0.0946
"-	15.2	0.0185	0.0877

Table 11: a_c and ϵ at $D = 3.0, 8.1$ and 15.2 m.

D [m]	Rel. error at P1 [%]	P2[%]	P3 [%]	P4 [%]
3.0	3.11	3.24	3.49	3.46
8.1	2.57	2.85	1.90	3.39
15.2	2.02	2.74	3.25	4.79

Table 12: Repetition errors. $L = 4.8$ m and $M = 96$. With absorbing beach.

Table 12 shows the relative errors between two independent time series measured by the first four probes in the stationary array. The errors are on a acceptable level with the exception of the relative error of 4.79% in P4 in the experiment $D = 15.2$ m from the wave generator.

7.1.3 $L = 9.6$ m and $M = 192$

At a later stage of the experimental work we started to focus on measuring the wave field over longer propagation lengths to possibly capture alterations in the spectral energy density distributions resulting from the dynamic nonlinear evolutions which evolve over longer spatial propagation lengths in the wave field. We also now aimed our focus on how the wave-induced current presented in chapter 6 could be detectable as a Doppler shift on the dispersion surface.

Figure 50 shows the (k, ω) -spectrum from a measurement with $M = 192$ measurement positions over a propagation length of $L = 9.6$ m, and with a spatial resolution of $\Delta x = 5$ cm. This measurement procedure corresponds to linking the two measurement procedures for the synthetic array with length $L = 4.8$ m. The measurement was done from the middle of the tank at $D = 8.1$ m.

The wavenumber and angular frequency axes were made dimensionless, and 10.4% of the elements in the spatial data series were modified by the space tapering function. The white curves shows the linear dispersion relation off-set by a small

Doppler shift due to an estimated wave-induced current of $u = 2$ cm/s. The upper black curve shows the third order dispersion shell.

Although the wave field is measured over a longer propagation length there is no pronounced difference in the spectral distribution around the first order dispersion shell. Intensities along the third order dispersion shell are identified.

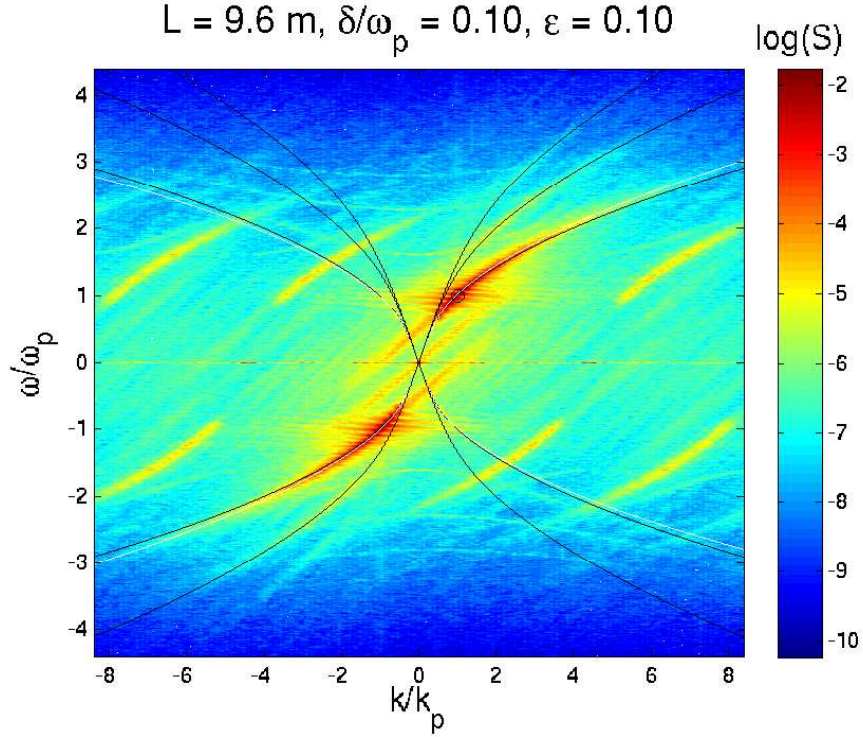


Figure 50: (k, ω) -spectrum. $L = 9.6$ m and $M = 192$. $u = 2$ cm/s.

D [m]	Rel. error at P1 [%]	P2[%]	P3 [%]	P4 [%]
8.1	10.27	12.58	14.31	13.58

Table 13: Repetition errors. $L = 9.6$ m and $M = 192$.

Table 13 shows the relative errors between two independent series measured by the first four probes in the stationary array. The relative errors are high. Interpolation errors were observed in the surface elevation data and figure 51 shows the first 80 s which are used for the spectral estimate measured by P1-P4 (upper to lower plot respectively). Four large interpolation errors can be seen; P2 (at 100 s), P3 and P4 (at 130 s) and P4 (at 70 s). Other errors were also observed later in the time series. The interpolation errors are caused by measurement errors extending over entire crests and troughs.

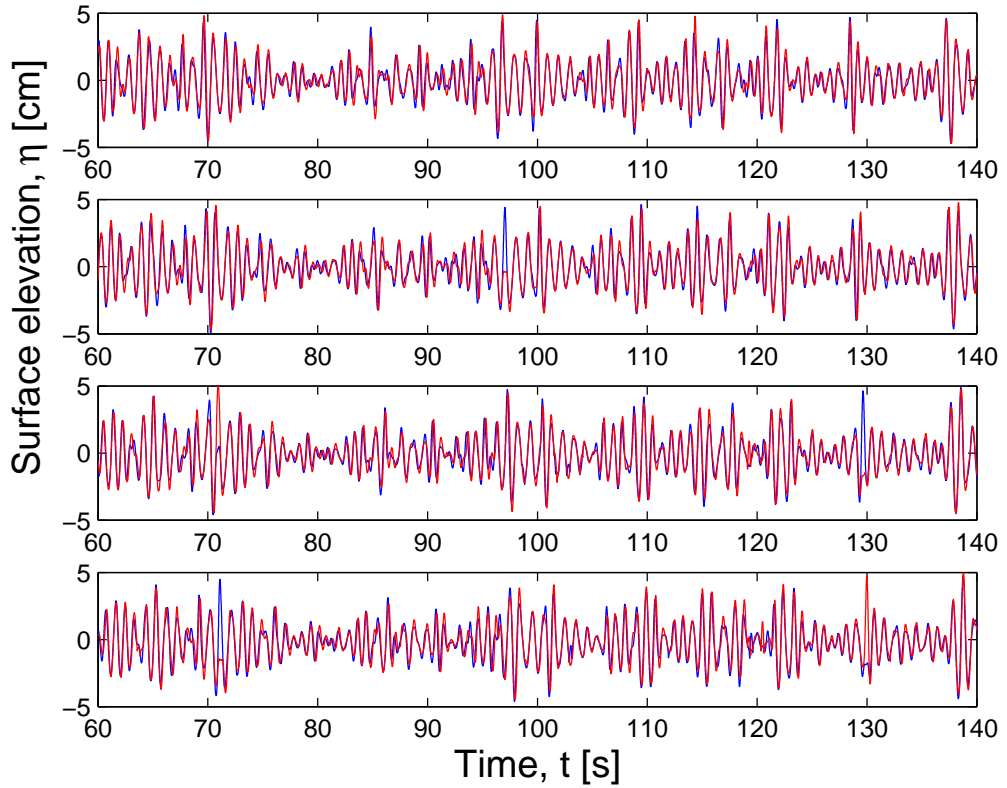


Figure 51: Large interpolation errors. $L = 9.6$ m and $M = 192$.

The author could not find an explanation of why there was such a sudden increase in measurement errors in series 1 which had been measured with lower relative errors earlier. Large dropouts appeared frequently of unknown reasons. Since this array represents a middle stage in the development of the synthetic array we will not go further into detail.

7.1.4 $L = 19.2$ m and $M = 128$

Figure 52 shows the (k, ω) -spectrum from the first experiment that covered most of the wave field in the flume. The synthetic array covered a propagation length of $L = 19.2$ m, with $M = 128$ measurement positions, and a spatial resolution of $\Delta x = 15$ cm. 7.8% of the elements in the spatial data series were modified by the space tapering function. The white curve shows the linear dispersion relation off-set by a small Doppler shift due to an estimated wave-induced current of $u = 2$ cm/s.

In figure 52 the extension of the wavenumber axis is short compared to other spectra. This is caused by that relatively few measurement points M are taken over a long propagation length L .

Over the peak \circ the spectral energy density is distributed over the first order dispersion shell and follows the white wave-induced off-set quite closely. Compared to $L = 9.6$ m in the previous subsection the spectral energy density seem to be distributed more over the first order dispersion shell above the peak. This could be caused by a weak Doppler shift, but the observation could also indicate that we to a larger extent are able to detect the dynamic nonlinear evolution when the wave

field is measured over longer propagation lengths. Uncertainties are connected to dispersion of shorter waves in the presence of longer waves as explained by Phillips (1981). Short propagating waves in presence of longer dominant propagating waves were observed in the wave field generated with the absorbing beach. We will discuss this problem more in detail in the conclusion in chapter 9.

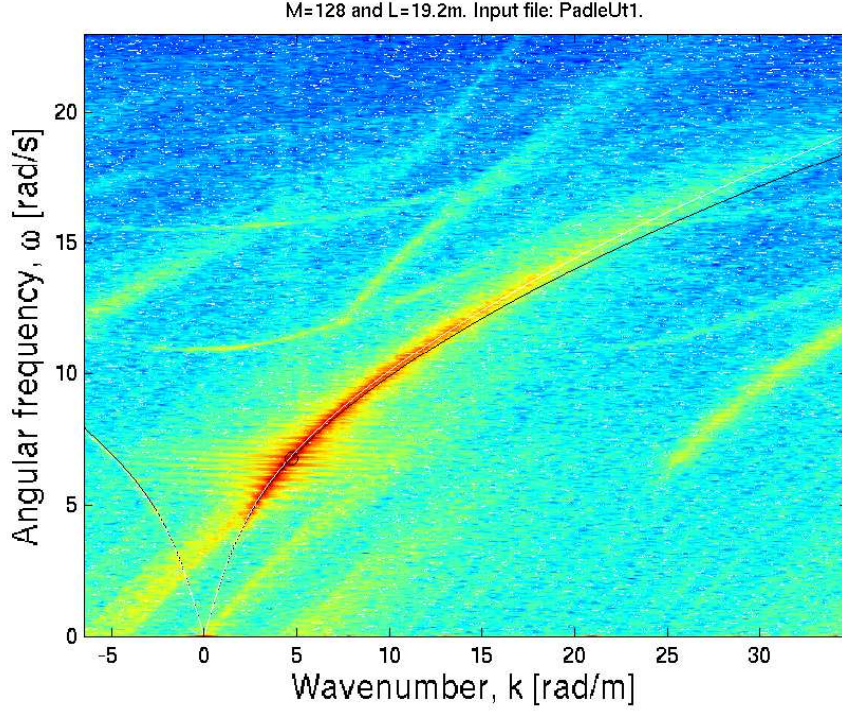


Figure 52: (k, ω) -spectrum. $L = 19.2$ m and $M = 128$. $u = 2$ cm/s.

Table 14 shows the relative error between two independent time series measured by the last four probes in the stationary array P13-P16. P13 was placed $D = 5.10$ m from the wave generator. The relative errors are quite low and lower than in the experiment presented in the previous section.

D [m]	Rel. error at P13 [%]	P14[%]	P15 [%]	P16 [%]
5.10	2.11	3.29	2.57	2.51

Table 14: Repetition errors. $L = 9.6$ m and $M = 192$.

7.1.5 $L = 19.2$ m and $M = 256$

Figure 53 shows the directly measured dispersion relation using a synthetic array which covered a length of $L = 19.2$ m, with $M = 256$ measurement positions, and a spatial resolution of $\Delta x = 7.5$ cm. 4% of the elements in the spatial data series were modified by the space tapering function. The wavenumber and angular frequency axes were made dimensionless. The white curves show the linear dispersion relation

off-set by a small Doppler shift due to an estimated wave-induced current of $u = 1$ cm/s. This illustrates the effect of a weaker current.

The spectral distribution of the free waves close to the peak suggests the validity of the linear dispersion relation. Above the peak the spectral energy density is distributed slightly over the linear dispersion relation. This could be caused by a weak Doppler shift on the dispersion surface. In addition the above peak deviation could indicate that dynamic nonlinear wave interactions are present in the wave field. The effect is on occasion relatively weak.

The spectrum does not maintain a thin well-defined dispersion surface, but we should be aware that relatively broad spectral distributions are caused by spectral leakage. Broad distributions are also caused by the relatively low resolution along the wavenumber axis.

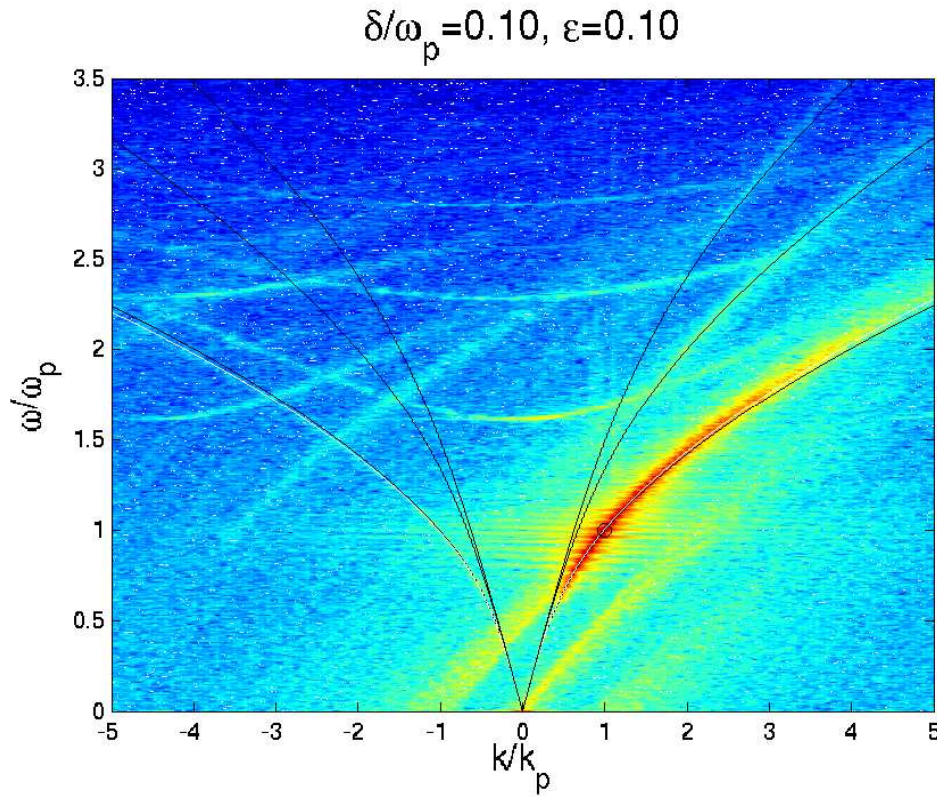


Figure 53: (k, ω) -spectrum. $L = 19.2$ m and $M = 256$. $u = 1$ cm/s.

Intensities along the second and third order dispersion shells are identified. Along the third order dispersion shell intensities are identified close to $(3k_p, 3\omega_p)$. Intensities from the second order difference harmonic below peak is pronounced and is distributed out from the origin and up to about $(2k_p, \omega_p)$.

The intensities which extends horizontally in bows and crosses the angular frequency axis at $\omega = 1.6\omega_p, 2.4\omega_p$ and $2.9\omega_p$ have not been identified. During the master thesis project we discussed that these intensities have a similar distribution as the dispersion of the Klein-Gordon equation. This has not been confirmed and will be discussed in the conclusion in chapter 9.

As in the previous subsections the smaller intensities to the left of the peak intensity with similar shape as the peak intensity is most likely caused by small errors

in either the distance Δx between the probes, or the 5 cm displacement between each synthetic measurement. The error will be tested in the numerical model in chapter 8.

Table 15 shows the relative error between two independent time series measured by the last four probes in the stationary array P13-P16. P13 was placed $D = 5.10$ m from the wave generator. The relative errors are low and a few minor measurement errors were observed in the surface elevation data.

D [m]	Rel. error at P13 [%]	P14[%]	P15 [%]	P16 [%]
5.10	3.46	3.07	5.11	2.79

Table 15: Repetition errors. $L = 19.2$ m and $M = 256$. Absorbing beach.

7.2 With reflecting beach and end wall

7.2.1 $L = 4.8$ m and $M = 96$

When the water depth was increased to $h = 0.60$ m, the spectra in subsection 7.1.2 showed that the appearance of reflected waves was less pronounced than when the water depth was $h = 0.35$ m. It was also observed that the appearance of reflected waves in the flume diminished when the water level was increased to $h = 0.60$ m. At $h = 0.35$ m the waves hit the vertical grid edge which the beach is built upon and this resulted in more reflected waves in the flume. At $h = 0.60$ m the waves propagated onto the sloped absorbing beach and were damped and absorbed more efficiently by the construction. On this background three additional experiments were performed with a steeper and harder beach constructed from a wooden plate (figure 54). The (k, ω) -spectra shows that the appearance of reflected waves then increases.



Figure 54: Reflecting beach.

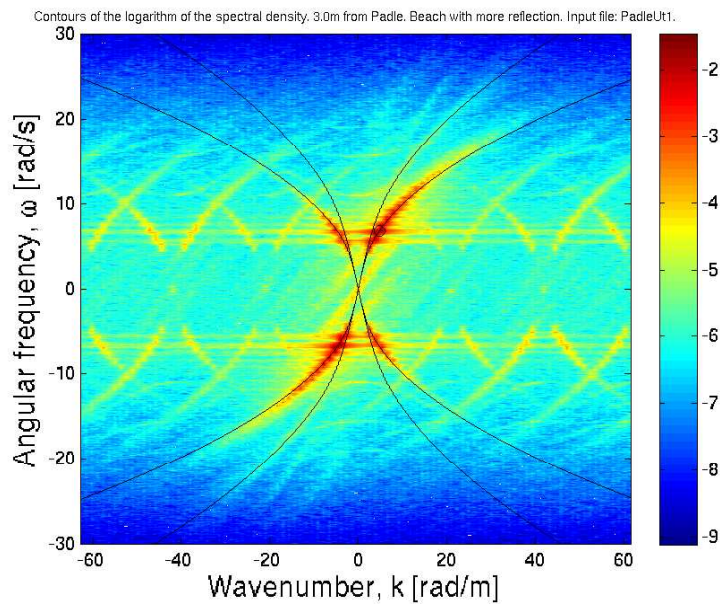


Figure 55: (k, ω) -spectrum. Reflecting beach. $L = 4.8$ m and $M = 96$. $D = 3.0$ m.

Figure 55-57 shows the directly measured dispersion relation at $D = 3.0$, 8.1, and 15.2 m, with the reflecting beach at the far end of the wave flume. The spectral energy density for reflected waves increases in the second quadrant for positive angular frequencies $\omega \geq 0$, and negative wavenumbers $k < 0$.

The (k, ω) -spectra shows that the spectral energy density from reflected waves

extends further up on the first order dispersion shell from the measurement at $D = 15.2$ m. This indicates that the presence of shorter reflected waves with higher frequency and wavenumber components are more pronounced near the absorbing beach.

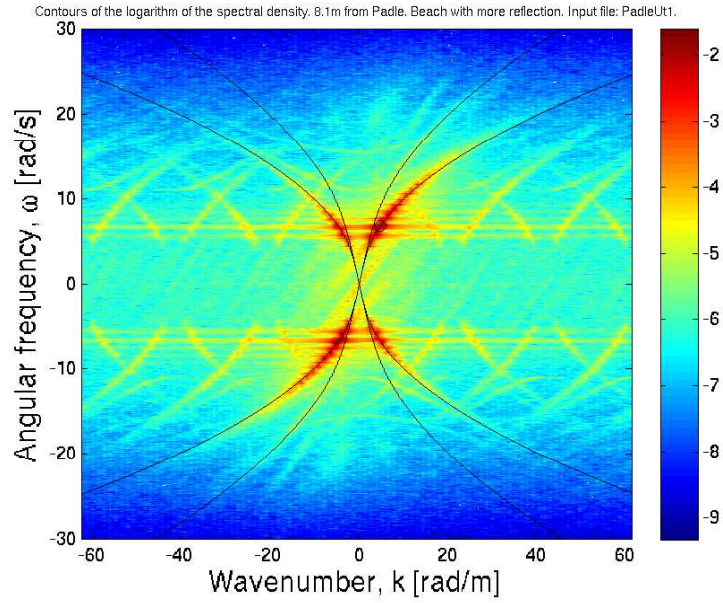


Figure 56: (k, ω) -spectrum. Reflecting beach. $L = 4.8$ m and $M = 96$. $D = 8.1$ m.

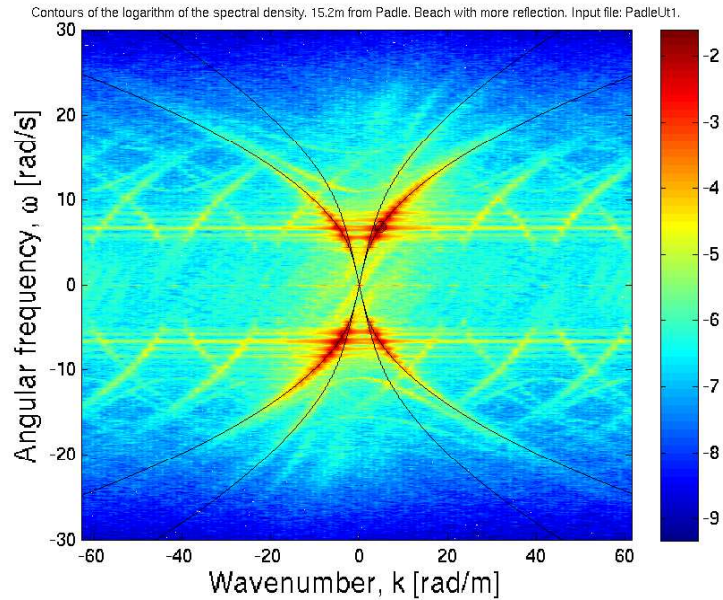


Figure 57: (k, ω) -spectrum. Reflecting beach. $L = 4.8$ m and $M = 96$. $D = 15.2$ m.

Table 16 shows the values for ϵ and a_c from the measured wave fields at $D =$

3.0, 8.1, and 15.2 m. a_c and ϵ increases when the wave reflection, from the reflecting beach, increases. Similar to the experiments in subsection 7.1.2 a_c and ϵ have the largest values at $D = 3.0$ m and lower values at $D = 8.1$ and 15.2 m.

D [m]	a_c [m]	ϵ [-]
3.0	0.0231	0.1095
8.1	0.0228	0.1082
15.2	0.0212	0.1005

Table 16: a_c and ϵ with reflecting beach.

D [m]	Rel. error at P1 [%]	P2[%]	P3 [%]	P4 [%]
3.0	19.86	18.63	22.19	20.22
8.1	1.93	2.71	1.46	1.91
15.2	3.41	2.28	2.22	2.85

Table 17: Repetition errors. $L = 4.8$ m and $M = 96$. Reflecting beach.

Repeatability with reflecting beach. Reflecting beach in slightly different positions.

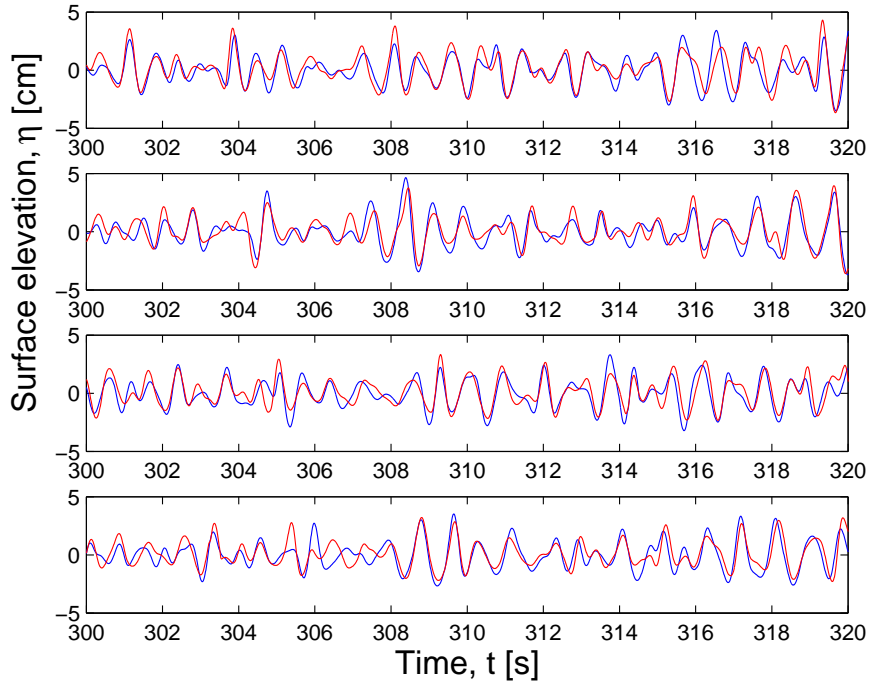


Figure 58: Repetition errors in experiment at $D = 3.0$ m with reflecting beach.

Table 17 shows the relative errors between two independent time series measured by the first four probes in the stationary array. The large errors in the

experiment at $D = 3.0$ m from the wave generator were caused by that in this experiment the reflecting beach was taken out of the wave flume between each run of series 1 to obtain more damping and less waiting time between each run. Figure 58 shows how these repetition errors appear in the time series and how sensitive the wave field is to slightly different positioning of the reflecting beach. In the experiments at $D = 8.1$ and 15.2 m the reflecting beach was not removed between each wave run and in these experiments the repetition errors were lower.

This experience established the importance of applying a reflection construction which could be kept in the same position for each wave run. Later we applied instead a vertical plastic wall which could be mounted on vertical rails on the wave flume inside side-walls (figure 59). The reflecting wall gives more reflection and is kept in the same position at each wave run. The reflecting wall can be removed easily between each wave run so that it takes less time before the wave field is damped and ready for a next run.



Figure 59: Reflecting wall.

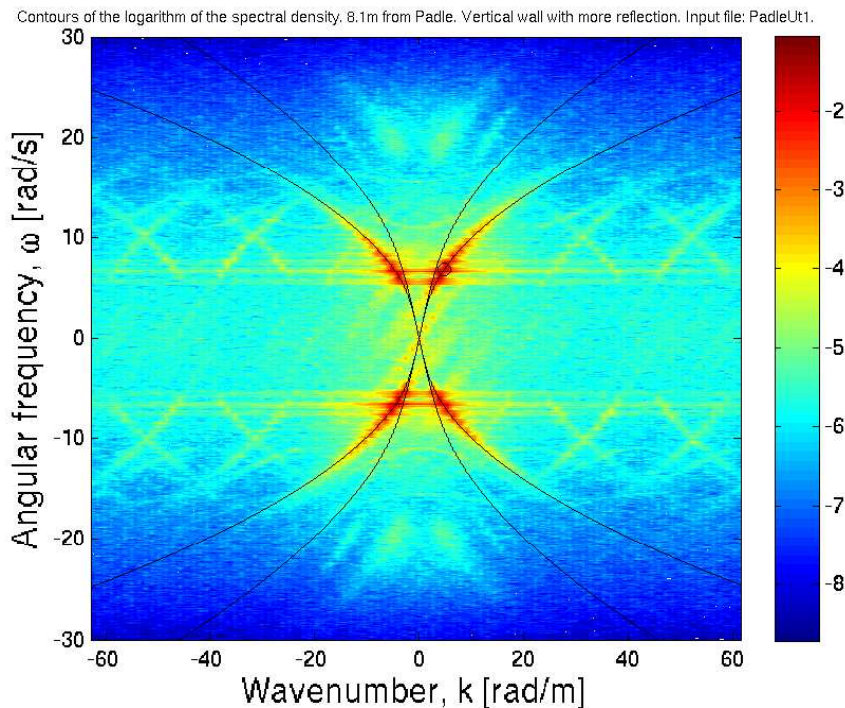


Figure 60: (k, ω) -spectrum. Reflecting wall. $L = 4.8$ m and $M = 96$. $D = 8.1$ m.

Figure 60 shows the directly measured dispersion relation using the reflecting wall at the far end of the wave flume. The wave field was measured in the middle of

the tank at $D = 8.1$ m. The spectral energy density from reflected waves ($\omega \geq 0$ and $k < 0$) increases in comparison with figure 55-57. There is now nearly a balance, in the spectral energy density distribution, between reflected and non-reflected waves.

Table 18 and 19 shows the values for ϵ and a_c from the experiment with the reflecting beach and the reflecting wall. There is a significant increase in a_c and ϵ when the reflecting beach is substituted by the reflecting wall.

D [m]	a_c [m]	ϵ [-]
8.1	0.0228	0.1082

Table 18: a_c and ϵ with reflecting beach.

D [m]	a_c [m]	ϵ [-]
8.1	0.0271	0.1286

Table 19: a_c and ϵ with reflecting wall.

Table 20 shows the relative errors between two independent time series measured by the first four probes in the stationary array. The errors were presented in more detail in chapter 5.4.2. The relative errors are caused by measurement errors from the probes which partly are a consequence of the increased steepness in the wave fields. Otherwise the repeatability is also quite good when the wave field is generated with the reflecting wall.

D [m]	Rel. error at P1 [%]	P2[%]	P3 [%]	P4 [%]
8.1	5.29	7.10	5.68	8.23

Table 20: Repetition errors. $L = 4.8$ m and $M = 96$. Reflecting wall.

7.2.2 $L = 19.2$ m and $M = 256$

Figure 61 shows the directly measured dispersion relation using the reflecting wall at the far end of the wave flume. The wave field was measured over a propagation length of $L = 19.2$ m, from $M = 256$ measurement positions, and with a spatial resolution of $\Delta x = 7.5$ cm. 4% of the elements in the spatial data series were modified by the space tapering function. The white curve is the linear dispersion relation off-set by a small Doppler shift due to an estimated wave-induced current of $u = 1$ cm/s.

The spectral distribution for reflected free waves $k < 0$ suggests the validity of the linear dispersion relation. The spectral energy density is distributed slightly under the first order dispersion shell and closer to the wave-induced off-set. This could indicate a weak Doppler shift on the dispersion surface.

For non-reflected free waves $k > 0$ the spectral energy density is distributed along the first order dispersion shell and close to the peak, the spectral distribution suggests the validity of the linear dispersion relation. Above the peak the spectral energy density is distributed slightly over the first order dispersion shell.

The spectrum does not maintain a thin well-defined dispersion surface, but we should be aware that relatively broad spectral distributions are caused by spectral leakage. Broad distributions are also caused by the relatively low resolution along the wavenumber axis. The effect of the resolution could be investigated in more detail.

Compared to the similar array measurement with the absorbing beach in subsection 7.1.5 figure 53, the spectral energy density along the second and third order dispersion shells are intensified. Even for the reflected waves we can see a weak intensity along the upper third order dispersion shell at $(-3k_p, 3\omega_p)$. The intensification could be a consequence of a increment in ϵ , from $\epsilon \approx 0.10$ in the wave field generated with the absorbing beach to $\epsilon \approx 0.13$ in the wave field generated with the reflecting wall.

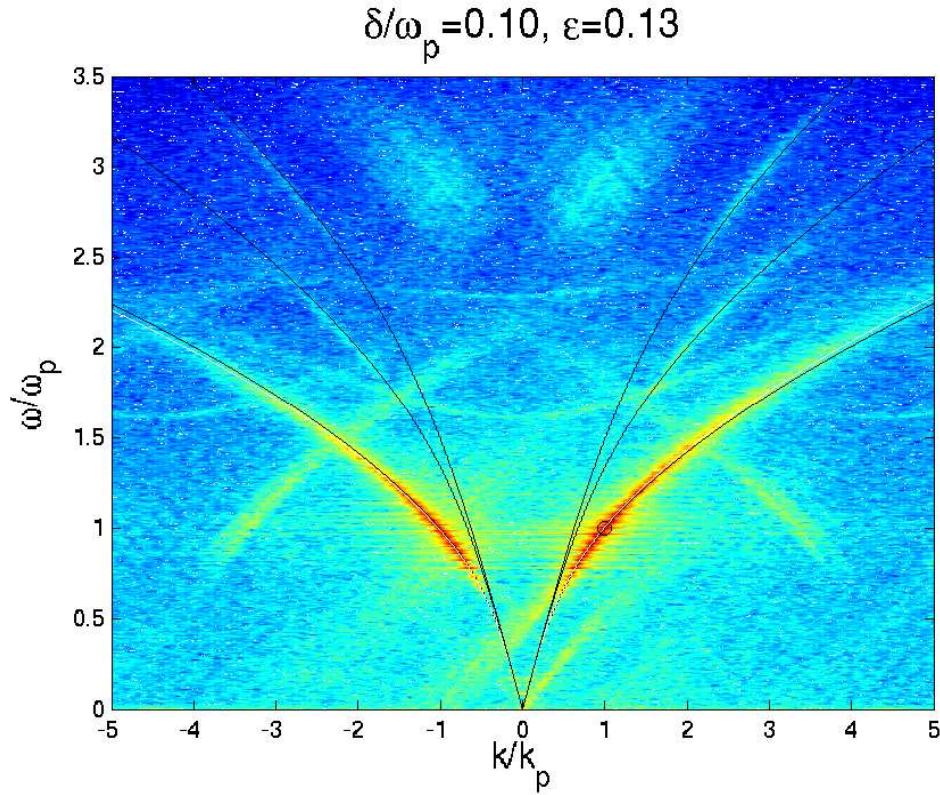


Figure 61: (k, ω) -spectrum. Reflecting wall. $L = 19.2$ m and $M = 256$. $u = 1$ cm/s.

The intensity from the second order difference harmonic below peak is not as pronounced as for the wave field which was generated with the absorbing beach. The spectral energy density is distributed from the origin and up to about $(k_p, \frac{1}{2}\omega_p)$. This indicates that the bounded second order difference waves appears at lower angular frequency and wavenumber components when the absorbing beach is substituted by the reflecting wall. The wave field generated with the reflecting wall generally consisted of longer and steeper waves.

Compared to the wave field generated with the absorbing beach the intensity from freely propagating waves above the spectral peak seemed to be less pronounced. This could be caused by that shorter propagating waves were suppressed and erased by the longer and steeper dominant breaking waves. With the reflecting wall oper-

ational, dominant wave breaking occurred frequently.

Similar to figure 53 intensities extend horizontally in bows and crosses the angular frequency axis at $\omega = 1.6\omega_p$ and $2.4\omega_p$. For reflected waves enhanced more pointwise intensities also appear at $(k_p, 3\omega_p)$ and $(-k_p, 3\omega_p)$. These have not been identified.

The smaller intensities beside the peak intensities with similar shapes as the peak intensities are most likely caused by small errors in either the distance Δx between the probes, or the 5 cm displacement between each synthetic measurement. The errors will be tested in the numerical model in chapter 8.

Table 21 shows the relative errors between two independent time series measured by the last four probes in the stationary array P13-P16. P13 was placed $D = 5.10$ m from the wave generator. The relative repetition errors are high. Some large measurement errors were observed in the surface elevation data.

D [m]	Rel. error at P1 [%]	P2[%]	P3 [%]	P4 [%]
5.10	10.73	13.20	12.42	10.40

Table 21: Repetition errors. $L = 19.2$ m and $M = 256$. Reflecting wall.

8 Numerical model

A simple first order numerical model of the unidirectional wave field in the laboratory wave flume was developed. The numerical model was applied to investigate the unwanted artifacts in the (k, ω) -spectra in chapter 7, the suspicion of small errors in Δx in the synthetic array measurements.

8.1 First order numerical model

A random linear superposition of s non-interacting regular synthetic unidirectional waves are generated from the summation,

$$\eta(x_m, t_n) = \sum_s A_s \cos(k_s x_m - \omega_s t_n + \theta_s) \quad (57)$$

where θ_s are random uniformly distributed phases between 0 and 2π . A new sequence of random numbers for the random phases is generated for each s .

The wavenumbers are uniformly distributed,

$$k_s = \frac{2\pi s}{L_s} \quad (58)$$

for $s = 0, 1, 2, \dots, S-1$. L_s is the propagation length of the synthetic wave field. The length of the array is set to $L_a = 19.2$ m in accordance with the longest synthetic array applied in the experiments. The propagation length of the synthetic wave field is approximately equal to the distance between the wave generator and the edge of the absorbing beach. The propagation length is set to be a irrational number $L_s = \sqrt{470} = 21.6794\dots$ so no rational relations occur between L_s and L_a .

The angular frequencies,

$$\omega_s = \sqrt{gk_s \tanh(k_s h)} \quad (59)$$

satisfies the linear dispersion relation and are non-uniformly distributed. To satisfy the non-uniformity $\Delta\omega_s$ is obtained by taking the difference between each ω_s value. The water depth is set to $h = 0.60$ m, in accordance with the latest experiments.

The amplitudes,

$$A_s = \sqrt{2S_s \Delta\omega_s} \quad (60)$$

where S_s is the spectral distribution from a JONSWAP spectrum with peak angular frequency $\omega_p = 6.80$ rads^{-1} in accordance with series 1 from the experiments.

The wavefield is sampled in time and space such that $x_m = m\Delta x$ for $m = 0, 1, 2, \dots, M-1$, and $t_n = n\Delta t$ for $n = 0, 1, 2, \dots, N-1$. The number of measurement points is set to $M = 256$ in accordance with the synthetic array which covered a propagation length of $L = 19.2$ m. $N = 64000$ time samples are taken from the synthetic wave field. After the samples have been collected $N = 12000$ time samples are removed from the start of the time series and the last $N = 52000$ time samples are applied for the spectral estimate. The time and space series have been tapered correspondingly to the referred experiment.

For the spectral analysis the angular frequencies and the wavenumbers have been discretized in the same manner as for the experimental analysis in section 4.1 with

$$\omega_j = \frac{2\pi j}{T} \quad (61)$$

for $j = -N/2, -(N-1)/2, \dots, -2, -1, 0, 1, 2, \dots, (N-1)/2, N/2$ and

$$k_g = \frac{2\pi g}{L_a} \quad (62)$$

for $g = -M/2, -(M-1)/2, \dots, -2, -1, 0, 1, 2, \dots, (M-1)/2, M/2$. $L_a = 19.2$ m is the length of the array. The spectral energy density is obtained from equation (40) in section 4.1,

$$S(k_g, \omega_j) = |\hat{\eta}_{g,j}|^2 = \hat{\eta}_{g,j} \hat{\eta}_{g,j}^*. \quad (63)$$

The contour levels of $\log_{10}(S)$ have been chosen in the same manner as in the experimental analysis.

8.2 Errors in Δx

Figure 62 shows the spectra for the first order synthetic wave field as presented in the previous section. No errors between the $M = 256$ equispaced measurement positions have been introduced. The bandwidth of the JONSWAP spectrum is relatively broader compared to the bandwidth of the measured spectrum in the laboratory. In fact it was rather difficult to diminish the spectral energy density above the spectral peak by applying the JONSWAP parameters to obtain a similar distribution as for the experimental wave fields. The relatively narrow bandwidths from the experiments are naturally caused by the relatively weak energy from waves with high frequency and wavenumber components in the laboratory wave flume. The spectra shows that the first order synthetic wave field satisfies the linear dispersion relation. The resolution in the spectra is not very satisfactory but it should be possible to see the introduced errors in Δx .

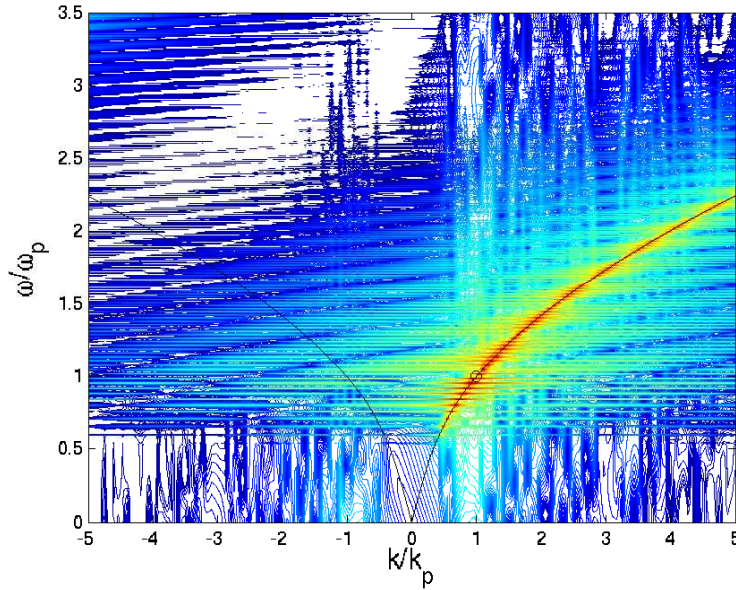


Figure 62: No errors in Δx introduced.

Figure 63 shows the spectrum in figure 62 when a 3 mm error in Δx is introduced between the 1st and the 2nd probe in the stationary array of sixteen probes. The spectrum shows similar features as in the spectrum from the experiments with the absorbing beach (figure 53 in subsection 7.1.5) but the spectral distributions connected to the errors is distributed more closely than in the experimental spectra. Caused by the relative broader bandwidth in the numerical simulations the spectral distribution extends up to higher wavenumber and angular frequency components.

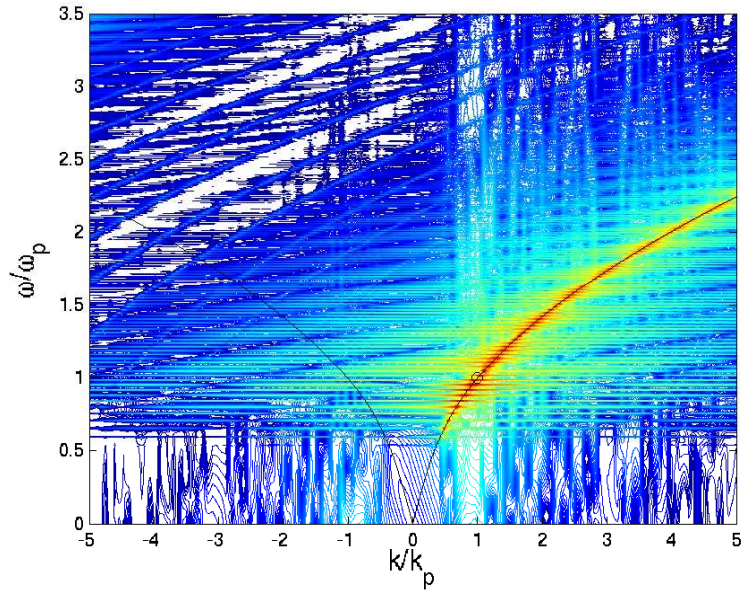


Figure 63: 3 mm error in Δx between the 1st and 2nd probe.

Figure 64 shows the spectrum when a 3 mm error in Δx is introduced between the 4th and the 5th probe in the stationary array of sixteen probes. Compared to figure 63 the distributions are grouped in three and three.

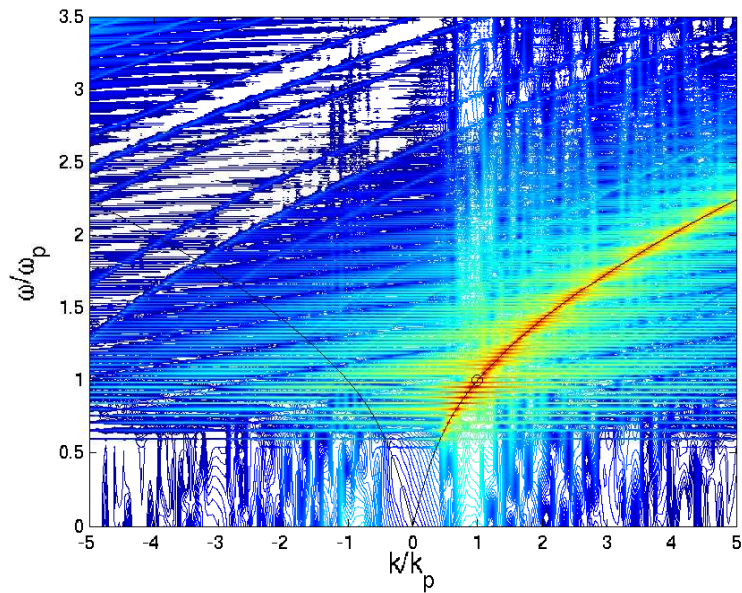


Figure 64: 3 mm error in Δx between the 4th and 5th probe.

Figure 65 shows the spectrum when a 3 mm error in Δx is introduced between the 8th and the 9th probe in the stationary array of sixteen probes. Compared to the spectra in figure 63 and figure 64 the distance between the distributions are

longer but the spectral distributions connected to the errors are still distributed more closely than in the experimental spectra.

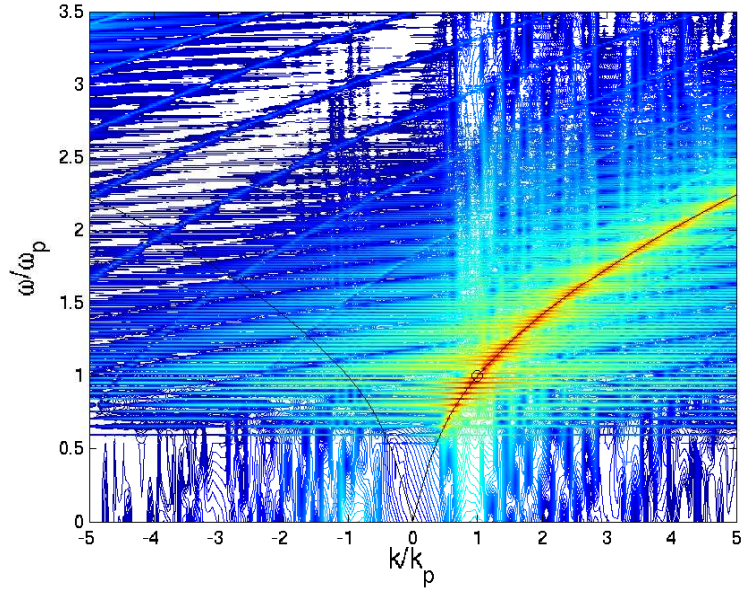


Figure 65: 3 mm error in Δx between the 8th and 9th probe.

Figure 66 shows the spectrum when a 3 mm error in Δx is introduced between the 12th and the 13th probe in the stationary array of sixteen probes. The spectra shows similar features as the spectrum in figure 64 were the error was introduced between the 4th and the 5th probe.

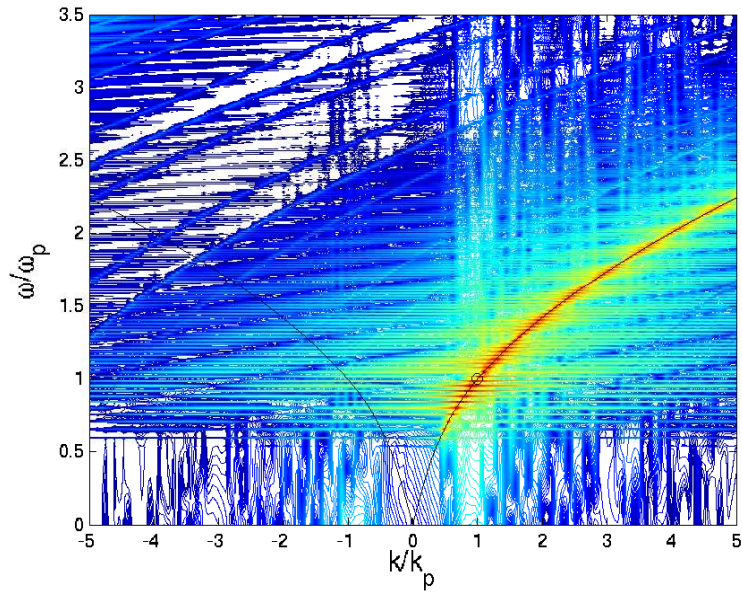


Figure 66: 3 mm error in Δx between the 12th and 13th probe.

Figure 67 shows the spectra when a 3 mm error in Δx is introduced between the last three synthetic measurement sub-procedures of $L = 4.8$ m. These errors introduces a glimmer on the dispersion surface.

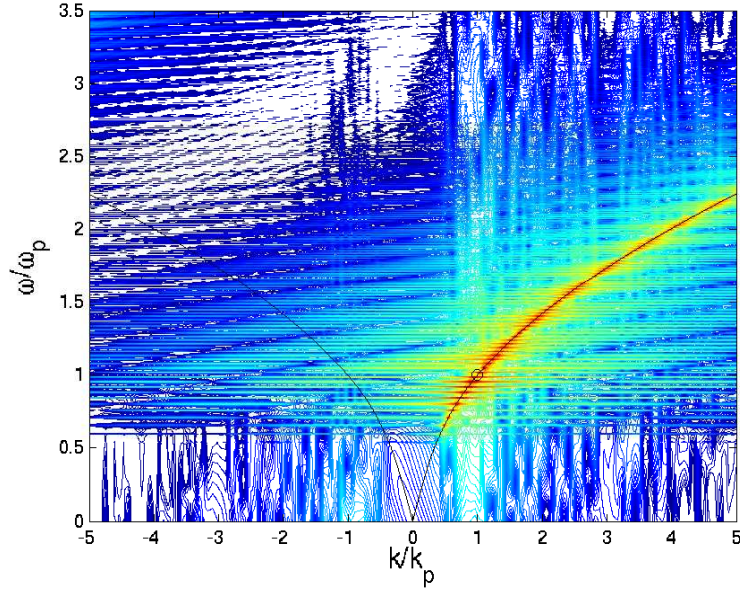


Figure 67: 3 mm error in Δx between the measurement sub-procedures.

When systematic errors in Δx between the probes in the stationary setup are introduced the spectra shows similar features in the spectral distributions as in the laboratory spectra. Although the spectral distributions caused by the errors are distributed closer in the numerical spectra. The numerical model is conclusive with regard to the shape of the spectral distributions caused by the errors but non-conclusive with regard to the distance between the distributions. 3 mm errors were introduced between all probes in the stationary array of sixteen probes and all errors showed spectral distributions in the spectra which were distributed closer than in the experimental spectra. Nevertheless, the shape of the spectral distributions may give an indication that errors between the probes generates the unwanted artifacts in the laboratory spectra. When a 3 mm error in Δx is introduced between the last three synthetic measurement sub-procedures of $L = 4.8$ m, these errors introduces a glimmer on the dispersion surface.

9 Conclusion

9.1 Conclusions and discussions

With reference to figure 53 and 61 in subsections 7.1.5 and 7.2.2 our laboratory experiments so far suggest the validity of the linear dispersion relation when the propagation distance for the free waves is rather short.

When the wave field is measured with the absorbing beach operational the spectral components of the free waves are distributed close to the linear dispersion relation. Above the peak the spectral energy density is distributed slightly over the linear dispersion relation. This could be caused by a weak Doppler shift, but the statistical analysis of the current is non-conclusive about the magnitude of the wave-induced current velocity. The spectral distributions from short waves above the peak, located slightly over the linear dispersion relation, are more prominent when the wave field is generated with the absorbing beach than with the reflecting wall. This is caused by that the presence of shorter free waves is more pronounced when the absorbing beach is operational. When the reflecting wall is operational long and steep waves are more dominant and wave breaking occur more frequently. As a consequence many short waves are distorted, suppressed and erased.

Based on observations of the wave field generated with the absorbing beach similar features as explained in reference to Phillips (1981) in indent five in the introduction appear in our experiments. The wave field generated with the absorbing beach is more short of breaking and this could lead to dispersion of shorter waves in the presence of longer waves. The deviation above peak could therefore be caused by that the dispersive short waves continue to propagate at a phase speed which depends on their own intrinsic frequency and on their location with respect to the dominant wave. When the slope of the dominating wave in the absorbing beach wave field increases, so does also its harmonic content which also propagates at the dominant wave speed. The effect of that the data is weakly filtered is probably less affective on the short propagating waves with reference to the figures in section 5.2 and the effect of capillary blockage at very high frequencies under strong wind forcing is less actual for our experiments since the waves are not wind generated.

When the wave field is measured with the reflecting wall operational the spectral components of both the reflected and the non-reflected free waves are distributed close to the linear dispersion relation. For non-reflected waves the spectral energy density is distributed slightly over the linear dispersion relation above the peak and for reflected waves the spectral energy density is distributed slightly under the linear dispersion relation above the peak. This could be caused by a weak Doppler shift, but supported by the statistical analysis of the current, the magnitude of the wave-induced current velocity is probably larger when the wave field is generated with the reflecting wall compared to when the wave field is generated with the absorbing beach. The indicated Doppler shift with the reflecting wall operational can therefore not be used as a general reference for a Doppler shift for both cases.

Static nonlinearities have been identified up to third order. When the wave field is generated with the absorbing beach the second order difference is prominent below the spectral peak in the spectrum. With the absorbing beach operational the second order difference is distributed up to higher wavenumber and frequency components compared to when the reflecting wall is operational. This is probably caused by that steeper and longer waves are more dominant in the wave field generated with the reflecting wall operational and so the harmonic content from the second order difference is distributed at lower wavenumber and frequency components.

Spectral distributions from higher harmonic second and third order bounded waves are more prominent when the absorbing beach is substituted by the reflect-

ing wall. This is most likely caused by the increased steepness of the wave field generated with the reflecting wall. As the steepness of the wave field increases, so does its harmonic content. With the reflecting wall operational the spectral distribution from reflected third order higher harmonic bounded waves are identified.

The experiments are non-conclusive with regard to the dynamic nonlinearity. The deviation from the linear dispersion relation in the numerical simulations by Krogstad and Trulsen (2010) suggesting that components above the spectral peak have larger phase and group velocities than anticipated by linear theory has not found support in the experimental results. This is most likely caused by that the simultaneous coverage in space applied in the experiments is too short to allow significant dynamic nonlinear evolution. The longest laboratory measurements covered a propagation length of 14 peak wavelengths, while for the numerical simulations a significantly longer propagation length covering 140 peak wavelengths was applied. Nevertheless, when the laboratory wave fields are measured over the longest propagation lengths the spectra indicates that the wave energy is distributed more over the linear dispersion relation above peak than when the wave fields are measured over short propagation lengths. This could strengthen an assumption that dynamic nonlinear wave interactions appear in the wave fields, but uncertainty is also connected to whether the above peak deviation is a consequence of a weak Doppler shift on the dispersion surface. As explained by Phillips (1981) deviations from the linear dispersion relation above peak could also be caused by that shorter waves are less dispersive in the presence of the more dominant breaking waves.

It has also been suggested from the experiments that the spectrum does not maintain a thin well-defined dispersion surface. Rather than being distributed along thin theoretical curves the wave energy has a more continuous distribution in (k, ω) -space. Some care needs to be taken into account for this interpretation, regarding the relatively low resolution along the wavenumber axis in the laboratory spectra and spectral leakage.

Some unidentified intensities appear in the laboratory spectra. The intensities which extends horizontally in bows and crosses the angular frequency axis at $\omega = 1.6\omega_p$ and $2.4\omega_p$ in figure 53 and 61 have not been identified. We discussed that these intensities have a similar distribution as the dispersion of the Klein-Gordon equation. This has not been investigated. The most reasonable explanation for these intensities can be found by an evaluation of the wavenumber and frequency components that these intensities carry in space and time. For instance, if we look at the lowest bow, the one that crosses the angular frequency axis at $\omega = 1.6\omega_p$ we see that the highest intensities appears for rather low wavenumbers meaning that this energy phenomena have rather long wavelengths. In addition the angular frequency components that this phenomena carry in time is about 50% higher than the peak angular frequency. One suggestion could be that this phenomena is long standing waves with different nodes which sets up in the tank during and after each wave run. When an experiment is performed some waiting between each wave run is recommended such that the long standing waves are properly damped before a next wave run. A waiting time for about ten minutes was recommended and used in the experiments. Nevertheless, the standing waves could be present during the wave generation and live for a longer time than expected after the wave generator ceases to generate waves into the flume. The intensities distributed at $\omega = 2.4\omega_p$ and $2.9\omega_p$ in the spectra from the absorbing beach wave field could be intensities from standing waves with other nodes. Offcourse this is only a speculation for the cause of these intensities and the results have not been confirmed. One way to verify this phenomena could in fact be to measure the surface elevation systematically after that the wave fields have been generated and possibly supplement the laboratory investigation with a mathematical model for the eigenfrequencies of the standing waves in the system, Kundu and Cohen (2008).

The smaller intensities beside the peak intensities with similar shapes as the peak intensities are most likely caused by small errors in the distance Δx between the probes in the stationary array. When introducing errors in Δx between the probes in the numerical model, similar spectral distributions appear as in the laboratory spectra, but the intensities are distributed closer than in the laboratory spectra. The shape of the spectral distributions may give an indication that small errors in Δx between the probes generates the unwanted intensities in the laboratory spectra, but the numerical model is non-conclusive with regard to the distance between the distributions. When a 3 mm error in Δx is introduced between the last three synthetic measurement sub-procedures of $L = 4.8$ m, the errors introduces a glimmer on the dispersion surface, which supports that these errors most likely are not causing the unwanted intensities in the laboratory spectra.

9.2 Suggestions for further work

To possibly verify dynamic nonlinear evolution a wave field should be measured over a longer propagation distance than that applied in the wave flume in the Hydrodynamic laboratory at Blindern. If a wave flume with longer simultaneous coverage in space could be applied, one requirement is that it is equipped with rails along the propagation direction of the wave field such that measurements can be taken with synthetic arrays and the wave field should be repeatable. For the measurements to be comparable to the numerical simulations by Krogstad and Trulsen (2010) one requirement is also that the generated waves are long-crested and unidirectional. With the peak wavelength $\lambda_p = 1.33$ m applied from series 1 in the recent experiments, the wave field should at least cover a propagation length of $L = 140\lambda_p = 186.2$ m to compare with the simultaneous coverage in space from the numerical simulations. With sixteen probes, limited by the number of sixteen input channels on the data acquisition card, in a stationary array, the consequence would be rather lengthy and time consuming measurement procedures, but probably possible to achieve.

Another interesting experiment could be to generate directional waves in a larger wave pool, equipped with multiple wave generators, and design an array which could measure directionality by using for instance an array transfer function such as from Barbers' method explained in Donelan et al. (1985). These types of experiments could enlighten problems connected to 3D FFT analysis of X-band radar imagery of short-crested, directional seas. It is known to the author that Marine© in Delft, in the Netherlands, offers these types of advanced laboratory facilities.

In the Hydrodynamic laboratory one alternative is to reduce the scale of the unidirectional short-crested wave fields. This can be done by reducing the peak wavelength and peak wave period. The simultaneous coverage in space in the wave flume is then utilized more optimally. If the peak wavenumber is reduced to $\lambda_p = 0.14$ m the propagation length $L = 19.2$ m covers about 140 peak wavelengths. If such short peak wavelength wave fields are possible to generate with the wave generator care must be taken to distinguish between the gravity and capillary regime. A investigation of the capillary wave dispersion relation could in itself be interesting, but is less applicable to real time ocean wave prediction. Care must be taken for the sampling in space, but with the synthetic array we have the freedom to chose the most convenient resolution in space for a given peak wave length.

Together with a reduction in the peak wavelength and wave period, the amplitude of the waves should be increased to increase the effect of nonlinearity in the wave field. The bandwidth could also be made more narrow. A Gaussian bell-shaped spectrum is probably easier to adjust with regard to the bandwidth and the wave energy distribution, and opens up for more precise modification of the wave field, than the JONSWAP spectrum which in any case is more broad banded as a consequence of the additional tail above the spectral peak. New input files for the wave generator

could be created with Gaussian bell-shaped, either frequency or wavenumber, wave energy distributions. A study of kurtosis or other statistical properties could also be applied to create laboratory wave fields with possible extreme events.

To determine the wave-induced current is a complicated flow problem. We have used the ADCP to measure time series of the fluid particle velocities in a range of positions between the bottom and the trough. Since the ADCP is not possible to calibrate, the same measurement coordinate should be used at all positions. This was not done in the experiments and some uncertainty is connected to the measurements at the upper three positions near the trough.

A more extended statistical analysis could be used to analyse the ADCP data. Fourier analysis could also be used to extract a possible peak fluid speed. The problem of measuring the time series is that generally it is difficult to extract the slowly varying movement of the current from the rapidly varying movements of the fluid particles. Even near the bottom of the flume the rapidly varying movements of fluid particles are present.

Analytical models could be made to estimate the wave-induced current. One exercise which was suggested by the main supervisor was, to study a regular wave on top of a stationary horizontal current which is inhomogenous in the vertical coordinate, and find out how the dispersion relation for the regular wave depends on the vertical current profile.

One possibility could also be to create a numerical model of the current-induced velocity by using the above analytical description with a combination of conservation and momentum equations, finite element/volume methods and the radiation stress. CFD could also be used, but is probably, depending on the resolution, limited to shorter time periods.

The peak wave period $T_p = 0.92$ s from series 1 in the recent experiments. By using the number of peak wave periods used for the spectral estimate in the numerical simulations in Krogstad and Trulsen (2010) the time period used for the laboratory spectral estimate should be $T = 170T_p = 156.4$ s. This is significantly less than the actual time period of 260 s which was used for the laboratory spectral estimate. The time period used for the laboratory spectral estimate could therefore have been reduced more significantly and this would also have reduced the CPU time for computing the (k, ω) -spectra. A time reduction, and use of the latest part of the measured time series, could also have been more convenient for the analysis of the wave-induced current which probably needs time to setup and is weaker in the beginning of the measured time series. Thus, some uncertainty of the achieved estimate for the wave-induced current could have been removed by removing more of the start of the time series.

10 References

- Barbarit A, Clément A (2006) Optimal latching control of a wave energy device in regular and irregular waves. *Appl Ocean Res* 28:77-91
- Barrick E (1986) The role of the gravity-wave dispersion relation in HF radar measurements of the sea surface. *IEEE J Oceanic Eng* 11:286-292
- Clauss GF, Kosleck S, Testa D, Hessner K (2008) Forecast of critical situations in short-crested seas. In Proceedings of ASME 27th International Conference on Offshore Mechanics and Arctic Engineering
- Donelan MA, Hamilton J, Hui WH (1985) Directional spectra of wind-generated waves. *Philos Trans R Soc A* 315:509-562
- Dysthe K (1979) Note on a modification to the nonlinear Schrödinger equation for application to deep water waves. *Philos Trans R Soc A* 369:105-114
- Forristall, GZ (2000) Wave crest distributions: Observations and Second-Order Theory. *J of Phys Ocean* 30:1931-1943
- Goda Y (2000) Random seas and design of maritime structures. World Scientific, Singapore.
- Grue J, Clamond D, Huseby M, Jensen A (2003) Kinematics of extreme waves in deep water. *Appl Ocean Res* 25:355-366
- Hara T, Karachintsev AV (2003) Observation of nonlinear effects in ocean surface wave frequency spectra. *J Phys Oceanogr* 33:422-430
- Hasselmann K (1962) On the nonlinear energy transfer in a gravity-wave spectrum. Part 1. General theory. *J Fluid Mech* 12:481-500
- Hasselmann K (1963a) On the nonlinear energy transfer in a gravity-wave spectrum. Part 2. Conservation theorems, wave-particle analogy, irreversibility. *J Fluid Mech* 15:273-281
- Hasselmann K (1963b) On the nonlinear energy transfer in a gravity-wave spectrum. Part 3. Computation of the energy flux and swell-sea interaction for a Neumann spectrum *J Fluid Mech* 15:385-398
- Hasselmann K, Barnett TP, Bouws E, Carlson H, Cartwright DE, Enke K, Ewing JA, Gienapp H, Hasselmann DE, Kruseman P, Meerburg A, Miller P, Olbers DJ, Richter K, Sell W, Walden H (1973) Measurements of wind-wave growth and swell decay during the Joint North Sea Wave Project (JONSWAP) *Deut Hydrogr Z A*(8) 12 p.95
- Huseby M, Grue J (2000) An experimental investigation of higher-harmonic wave forces on a vertical cylinder. *J Fluid Mech* 414:75-103
- Johnson DH, Dudgeon DE (1993) Array Signal Processing, Concepts and Techniques. Prentice Hall, New Jersey.
- Krogstad HE, Trulsen K (2010) Interpretations and observations of ocean wave spectra. *Ocean Dynamics* 60:973-991
- Kundu KP, Cohen IM (2008) Fluid Mechanics. Elsevier Academic Press, California.
- Lake BM, Yuen HC (1978) A new model for nonlinear wind waves. Part 1. Physical model and experimental evidence. *J Fluid Mech* 88:33-62

- Longuet-Higgins MS (1963) The effect of non-linearities on statistical distributions in the theory of sea waves. *J Fluid Mech* 17:459-480
- Longuet-Higgins MS, Stewart RW (1963) Changes in the form of short gravity waves and tidal currents. *J Fluid Mech* 8:565-583
- Masuda A, Kuo YY, Mitsuyasu H (1979) On the dispersion relation of random gravity waves. Part 1. Theoretical framework. *J Fluid Mech* 92:717-730
- Mitsuyasu H, Kuo YY, Masuda A, (1979) On the dispersion relation of random gravity waves. Part 2. An experiment. *J Fluid Mech* 92:731-749
- Newman JN (1977) Marine Hydrodynamics. The MIT Press, Cambridge Massachusetts.
- Nieto Borge JC, Rodríguez G, Hessner K, Izquierdo P (2004) Inversion of marine radar images for surface wave analysis. *J Atmos Ocean Tech* 21:1291-1300
- Nieto Borge JC, Hessner K, Jarabo-Amores P, de la Mata-Moya D (2008) Signal-to-noise ratio analysis to estimate ocean wave heights from X-band marine radar image time series. *IET Radar Sonar Navig* 2:35-41
- Nuttall A, Albert H (1981) Some windows with very good sidelobe behavior. *IEEE Trans on Acous and Signal Process* Vol. ASSP-29:84-91
- Phillips OM (1960) On the dynamics of unsteady gravity waves of finite amplitude. Part 1. *J Fluid Mech* 9:193-217
- Phillips OM (1961) On the dynamics of unsteady gravity-waves of finite amplitude. Part 2. *J Fluid Mech* 11:143-155
- Phillips OM (1981) The dispersion of short wavelets in the presence of a dominant long wave. *J Fluid Mech* 107:465-485
- Ramamonjiarisoa A, Coantic M (1976) Loi expérimental de dispersion des vagues produites par le vent sur une faible longueur d'action *C R Acad Sci B* 282:111-113
- Tucker MJ (1957) The analysis of finite-length records of fluctuating signals. *British J of Appl Phys* 8:137-142
- Tucker MJ, Pitt EG (2001) Waves in ocean engineering. Elsevier Science & Technology, Oxford.
- Wang DW, Hwang PA (2004) The dispersion relation of short wind waves from space-time wave measurements. *J Atmos Ocean Tech* 21:1936-1945
- Zakharov VE (1968) Stability of periodic waves of finite amplitude on the surface of a deep fluid. *J Appl Mech Tech Phys* 9:190-194

11 Appendix

A Theoretical framework

A.1 Linear wave theory

A.1.1 Obtaining c_1 , c_2 , $f(z)$ and ϕ

The velocity potential in equation (12) is obtained by assuming that x and z are separable variables such that,

$$\phi(x, z, t) = f(z) \sin(kx - \omega t). \quad (64)$$

Substitution of the separable form of the velocity potential in equation (64) into the Laplace equation (5) gives a second order ordinary differential equation with two unknown constants c_1 , and c_2 which are determined from the kinematic boundary conditions (8) and (6),

$$\begin{aligned} \frac{\partial^2 \phi}{\partial x^2} + \frac{\partial^2 \phi}{\partial z^2} = 0 &= \frac{\partial^2}{\partial x^2} [f(z) \sin(kx - \omega t)] + \frac{\partial^2}{\partial z^2} [f(z) \sin(kx - \omega t)] \\ &= -f(z)k^2 \sin(kx - \omega t) + f''(z) \sin(kx - \omega t) \\ &= f''(z) - k^2 f(z). \end{aligned} \quad (65)$$

(65) is a second order homogenous ordinary differential equation with a general solution that can be written on the form,

$$f(z) = c_1 \cosh kz + c_2 \sinh kz. \quad (66)$$

The separable form of the velocity potential (64) then becomes,

$$\phi(x, z) = [c_1 \cosh kz + c_2 \sinh kz] \sin(kx - \omega t) \quad (67)$$

where c_1 , and c_2 are constants that can be determined from the kinematic boundary conditions. The kinematic condition at the bottom $z = -h$ (8) gives,

$$\begin{aligned} \frac{\partial \phi}{\partial z} = 0 &= [kc_1 \sinh kz + kc_2 \cosh kz] \sin(kx - \omega t) \\ &= kc_1 \sinh -kh + kc_2 \cosh -kh \\ &= -kc_1 \sinh kh + kc_2 \cosh kh \\ &\Downarrow \\ c_1 &= c_2 \frac{\cosh kh}{\sinh kh}, \end{aligned} \quad (68)$$

and the kinematic condition at the linearized free surface $z = 0$ (6) gives,

$$\begin{aligned} \frac{\partial \eta}{\partial t} &= \frac{\partial \phi}{\partial z} \\ &\Downarrow \\ \omega a \sin(kx - \omega t) &= [kc_1 \sinh 0 + kc_2 \cosh 0] \sin(kx - \omega t) \\ &\Downarrow \\ c_2 &= \frac{a\omega}{k}, \end{aligned} \quad (69)$$

which gives,

$$c_1 = \frac{a\omega \cosh kh}{k \sinh kh}. \quad (70)$$

Substitution of (70), and (69) into (66) gives,

$$\begin{aligned}
f(z) &= \frac{a\omega}{k} \frac{\cosh kh}{\sinh kh} \cosh kz + \frac{a\omega}{k} \sinh kz \\
&= \frac{a\omega}{k} \left(\frac{\cosh kh \cosh kz + \sinh kz \sinh kh}{\sinh kh} \right) \\
&= \frac{a\omega}{k} \frac{\cosh k(z+h)}{\sinh kh}
\end{aligned} \tag{71}$$

which substituted into (64) gives the velocity potential (12),

$$\phi(x, z, t) = \frac{a\omega}{k} \frac{\cosh k(z+h)}{\sinh kh} \sin(kx - \omega t). \tag{72}$$

A.1.2 Obtaining the linear dispersion relation equation

The linear dispersion relation is obtained by substituting the velocity potential (12) and the regular wave solution (11) into the linearized dynamic boundary condition (7),

$$\begin{aligned}
\frac{\partial \phi}{\partial t} + g\eta &= 0 \\
&\Downarrow \\
-\frac{a\omega^2}{k} \frac{\cosh k(z+h)}{\sinh kh} \cos(kx - \omega t) + ga \cos(kx - \omega t) &= 0 \\
&\Downarrow \\
\frac{a\omega^2}{k} \frac{\cosh k(z+h)}{\sinh kh} &= ga \\
&\Downarrow_{z=0} \\
\omega^2 \frac{\cosh kh}{\sinh kh} &= gk \\
&\Downarrow \\
\omega^2 &= gk \tanh kh.
\end{aligned} \tag{73}$$

B Experimental arrangements

B.1 Early stage experimental arrangement

B.1.1 Modification of original input files

The original input files are time series in electrical Voltage $V_e(t)$ for the wave generator based on JONSWAP spectral energy distributions. The input files consists of $2^{14} = 16384$ elements. In Wavelab the scan rate, which is the number of elements given from a input file to the wave generator each second should be set to 50 Hz in accordance with the previous project Grue et al. (2003). This gives the length of the time series $T = 16384/50\text{Hz} = 327.68$ s, which for simplicity has been approximated to 330 s in chapter 3. Hypothetically a increased scan rate should give,

- steeper waves which as a consequence would increase the nonlinearity in the wave fields,
- shorter wave lengths and wave periods which would give a relative longer simultaneous coverage in space for the wave field such that the array would be utilized more optimally,
- shorter time series and less time consuming experiments.

When the scan rate was increased to over 50 Hz the wave generator refused to generate the input files. Different methods were then tried out next for modifying the original input files. These methods can be summarized in the following:

- Increasing the amplitude of the original input files with 0.1-1.8%.

- Try to make the original input files shorter by deleting every 2nd, 3rd, 4th, ... , 90th element.
- Point two in a combination with interpolation.

The wave generator generated the increasement of 1.7% of the original input file for series 1, but refused to generate the 1.8% increasement. All of the modified input files described in point two and three above were refused by the wave generator. The amplitude a_c and steepness ϵ of the wave field generated with the 1.7% increasement are presented in chapter 5. Later an analysis of the maximum value interval $\max\{dV_e(t)\}$, maximum velocity $\max\{dV_e(t)/dt\}$ and maximum acceleration $\max\{d^2V_e(t)/dt^2\}$ for each of the original input files were carried out to get an answer for what was the maximum allowed acceleration for the wave generator. The results are summarized in table 22 for all the six original input files and the 1.7% and 1.8% increasement of the input file for series 1.

Input file for;	$\max\{dV_e(t)\}$ [V]	$\max\{\frac{dV_e(t)}{dt}\}$ [V/s]	$\max\{\frac{d^2V_e(t)}{dt^2}\}$ [V/s ²]
Series 1	0.1512	7.5619	132.5680
Series 2	0.2026	10.1322	126.0018
Series 3	0.1526	7.6397	110.4315
Series 4	0.1107	5.5326	86.4518
Series 5	0.1245	6.2245	109.0980
Series 6	0.1277	6.3837	89.4255
Series 1, 1.7% increase	0.1538	7.6905	134.8225
Series 1, 1.8% increase	0.1540	7.6980	134.9525

Table 22: Input file velocities and accelerations.

The analysis showed from the 1.7% and 1.8% increasement that the maximum allowed acceleration for the wave generator probable was between 134.8000 and 134.9000 V/s² and that the input file for series 1 was the one of the original input files that provided the largest acceleration.

B.1.2 Calibration

The automatic programming procedure of the probes is easy to use, and from the only button on the sensor it is possible to program a 10 cm window centered from a chosen position within the sensing range. There are lights on the probes that indicate if the sensor is outside the minimum or maximum sensing range.

The calibration of the probes are done to test if the probes respond accurately on changes of position due to an object. This can simply be done by mounting a probe on a rod with a ruler above for instance a calm water surface, program the probe for a 10 cm window, raise the probe with +5 cm to the maximum limit of the window, and then stepwise, with for instance 1 cm for each step, lower the probe down to the minimum limit at -5 cm of the window, and measure the calm water surface at each step for, for instance 1s. The same procedure can then be done back again, from the minimum to the maximum limit of the window. Note that we have to make sure that the minimum and maximum limits of the window is within the sensing range of the probe.

Figure 68 shows the calibration curve for the calibration procedure mentioned above for one of the probes from the laboratory. The distance observed on the ruler was in accordance with the data from the probe, and the probe responded accurately on changes of position due to the calm water surface. Suprisingly, some of the available probes in the laboratory had opposite response curves than other probes, for the same calibration procedure as explained above, and we do not know the reason why this was the case. When these probes were used to measure the surface elevation the resulting time series became "up-side-down". This problem was solved by multiplying the time series with (-1) in Lab-View such that the time series were turned the right way. The aberration was reported to

the company. Some of the available new probes provided data with relatively large signal to noise ratios compared to older probes. The noise, shown in section 5.2 Filter, could be problematic if capillary waves should be measured. This aberration was also reported to the company.

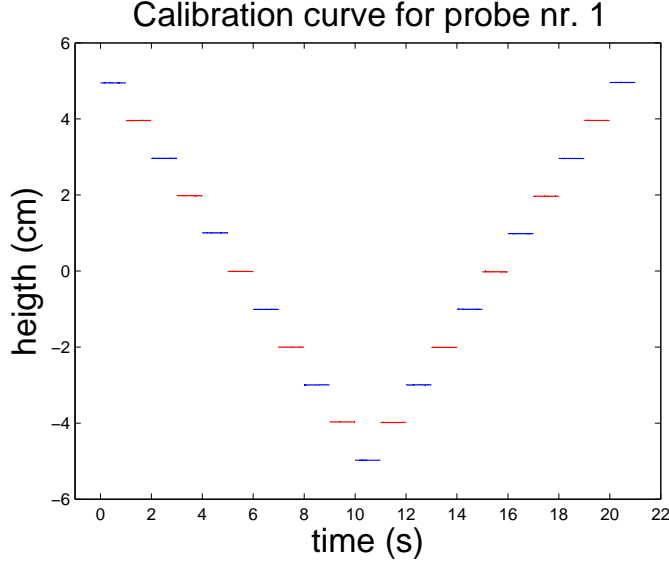


Figure 68: Calibration curve.

C Method of analysis

C.1 Discrete Fourier transform

C.1.1 Obtaining the DFT $\hat{\eta}$

To derive an expression for $\hat{\eta}_j$ we utilize the fundamental mathematical property that a system of complex exponential functions is an orthogonal system of functions, and take the l_2 inner product,

$$\langle f_n, g_n \rangle = \sum_{n=0}^{N-1} f_n g_n^* \quad (74)$$

of (30). * denotes the complex conjugate.

$$\begin{aligned} \langle \eta_n, e^{-i\omega_l t_n} \rangle &= \left\langle \sum_{j=0}^{N-1} \hat{\eta}_j e^{-i\omega_j t_n}, e^{-i\omega_l t_n} \right\rangle \\ &\Downarrow \\ \sum_{n=0}^{N-1} \eta_n e^{i\omega_l t_n} &= \sum_{n=0}^{N-1} \sum_{j=0}^{N-1} \hat{\eta}_j e^{-i\omega_j t_n} e^{i\omega_l t_n} \\ &= \sum_{j=0}^{N-1} \hat{\eta}_j \sum_{n=0}^{N-1} e^{i(\omega_l - \omega_j) t_n} \\ &= \sum_{j=0}^{N-1} \hat{\eta}_j N \delta_{l,j} \\ &= N \hat{\eta}_l, \end{aligned} \quad (75)$$

where,

$$\delta_{l,j} = \begin{cases} 1 & \text{if } l = j \\ 0 & \text{if } l \neq j \end{cases}$$

is the Kronecker delta function. (75) gives the DFT $\hat{\eta}$,

$$\hat{\eta}_j = \frac{1}{N} \sum_{n=0}^{N-1} \eta_n e^{i\omega_j t_n}. \quad (76)$$

D Surface elevation

D.1 Frequency spectra from series 1-6 on $h = 0.35$ m

At an early stage of the experimental work all the six different random wave time series and a wave time series from a modified input file were measured at a water depth of $h = 0.35$ m. The modified input file is a 1.7% increase of the original input file for series 1. The wave series generated from the modified input file has a similar angular frequency spectrum as series 1, and therefore only the angular frequency spectrum for series 1 is presented in this section.

The wave series were measured by the first developed synthetic array with $M = 24$ measurement positions over a short propagation length of $L = 1.2$ m, and with a spatial resolution of $\Delta x = 5$ cm. The intention of measuring all seven wave fields was to investigate which wave field that could provide the largest steepness ϵ , based on the characteristic amplitude $a_c = \sqrt{2\langle\eta^2\rangle}$ and the peak wavenumber k_p of the wave field. Given the peak angular frequencies ω_p from the angular frequency spectra in this section the peak wavenumbers k_p were estimated from the linear dispersion relation (13) by a numerical iteration.

Figure 69 and 70 shows the two-sided linear and logarithmic frequency spectra (plotted for only $\omega \geq 0$) from series 1 measured from all the $M = 24$ measurement positions in the synthetic array. The peak angular frequency is $\omega_p = 6.80$ rads⁻¹.

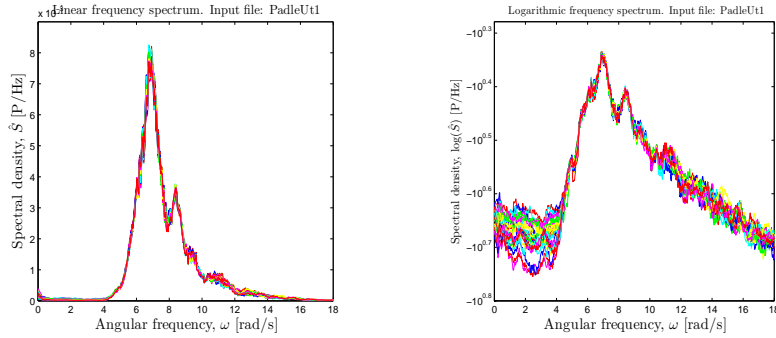


Figure 69: Linear frequency spectrum from series 1. **Figure 70:** Logarithmic frequency spectrum from series 1.

Figure 71 and 72 shows the linear and logarithmic frequency spectra from series 2. The peak angular frequency is $\omega_p = 5.60$ rads⁻¹.

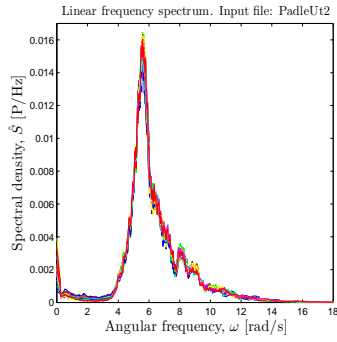


Figure 71: Linear frequency spectrum from series 2.

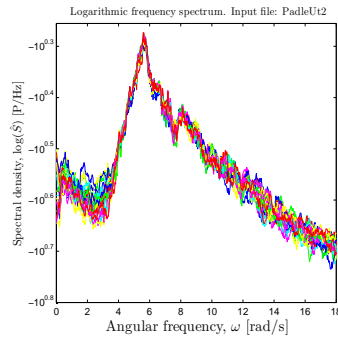


Figure 72: Logarithmic frequency spectrum from series 2.

Figure 73 and 74 shows the linear and logarithmic frequency spectra from series 3. The peak angular frequency is $\omega_p = 5.55 \text{ rads}^{-1}$.

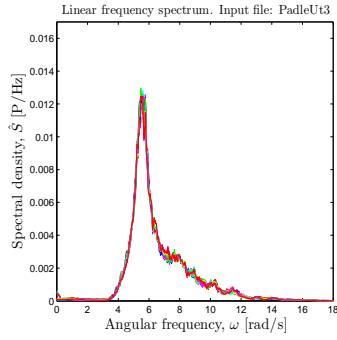


Figure 73: Linear frequency spectrum from series 3.

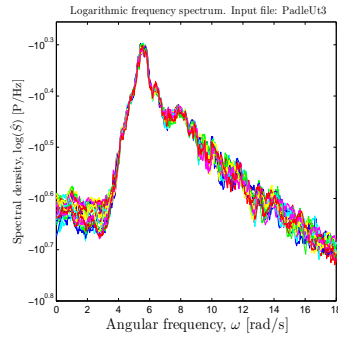


Figure 74: Logarithmic frequency spectrum from series 3.

Figure 75 and 76 shows the linear and logarithmic frequency spectra from series 4. The peak angular frequency is $\omega_p = 5.50 \text{ rads}^{-1}$.

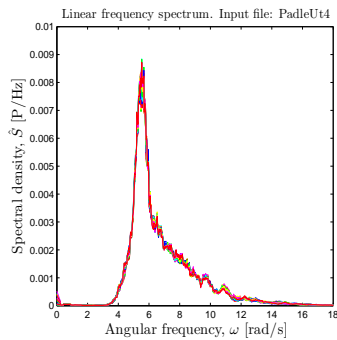


Figure 75: Linear frequency spectrum from series 4.

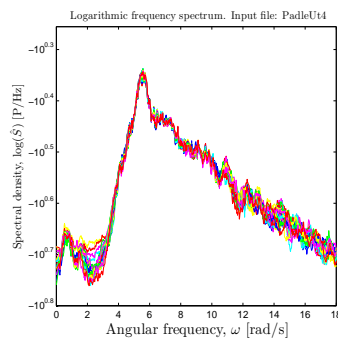


Figure 76: Logarithmic frequency spectrum from series 4.

Figure 77 and 78 shows the linear and logarithmic frequency spectra from series 5. The peak angular frequency is $\omega_p = 6.70 \text{ rads}^{-1}$.

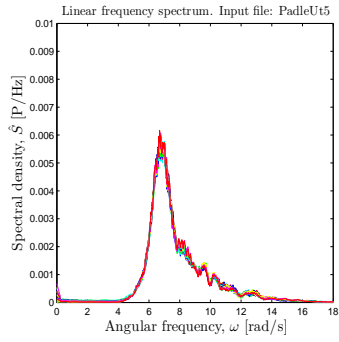


Figure 77: Linear frequency spectrum from series 5.

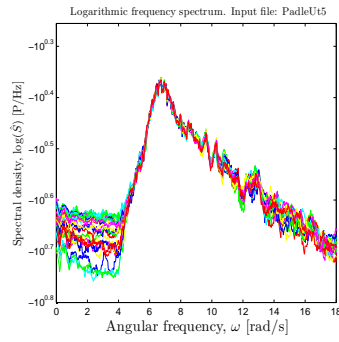


Figure 78: Logarithmic frequency spectrum from series 5.

Figure 79 and 80 shows the linear and logarithmic frequency spectra from series 6. The peak angular frequency is $\omega_p = 6.40 \text{ rads}^{-1}$.

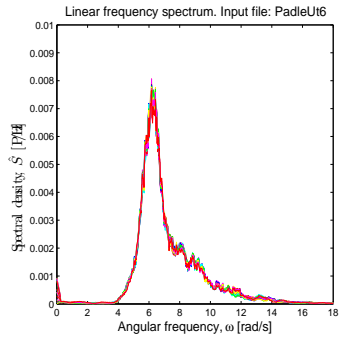


Figure 79: Linear frequency spectrum from series 6.

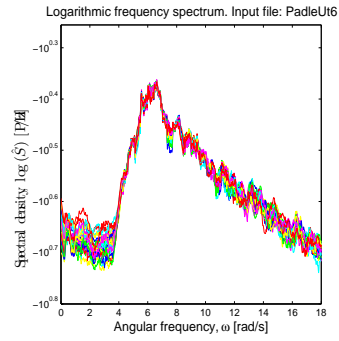


Figure 80: Logarithmic frequency spectrum from series 6.

D.2 Bandwidths from series 1-6 on $h = 0.35$ m

Figure 81 - 86 shows the linear angular frequency spectra estimated from series 1-6 on $h = 0.35$ m with the absorbing beach operational at the far end of the wave flume. All the frequency spectra are estimated from measurements at $D = 9.00$ m from the wave generator. The horizontal line $S_{max}/2$ is plotted in all figures. The figures were used to estimate the normalized bandwidth for series 1-6 on $h = 0.35$ m.

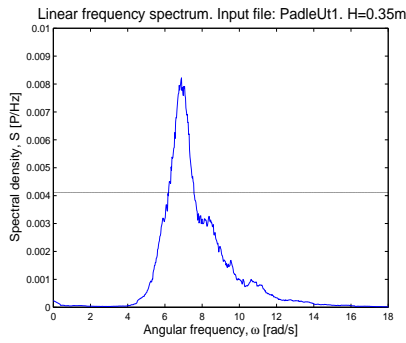


Figure 81: Series 1.

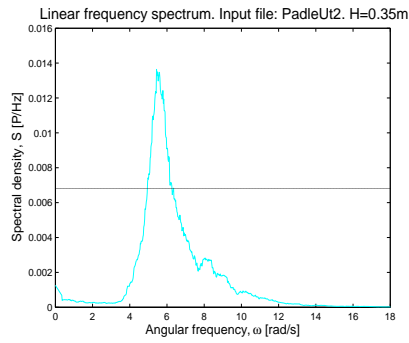


Figure 82: Series 2.

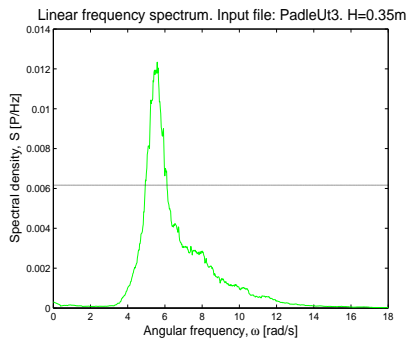


Figure 83: Series 3.

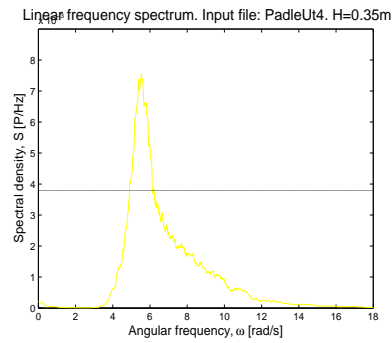


Figure 84: Series 4.

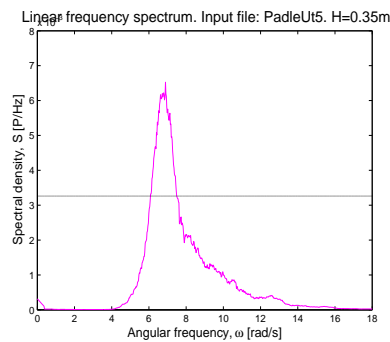


Figure 85: Series 5.

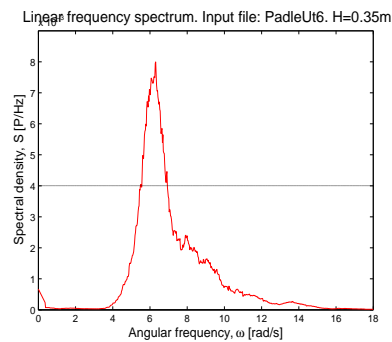


Figure 86: Series 6.

E The measured dispersion relations

E.1 $L = 1.2$ m and $M = 24$

E.1.1 (k, ω) -spectra measured from series 2-6

This appendix shows the logarithmic (k, ω) -spectra measured from series 2-6 and the modification of series 1.

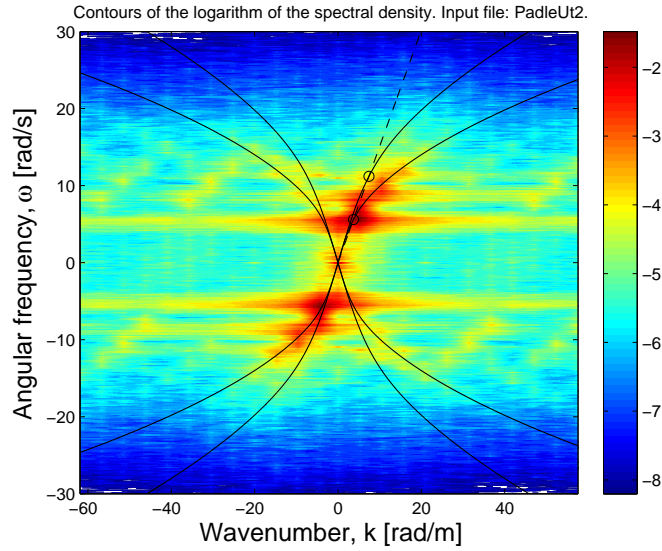


Figure 87: Logarithmic (k, ω) -spectra measured from series 2.

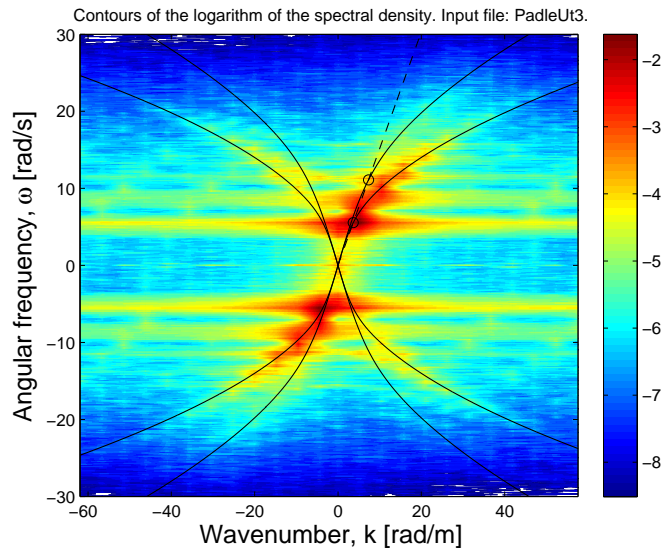


Figure 88: Logarithmic (k, ω) -spectra measured from series 3.

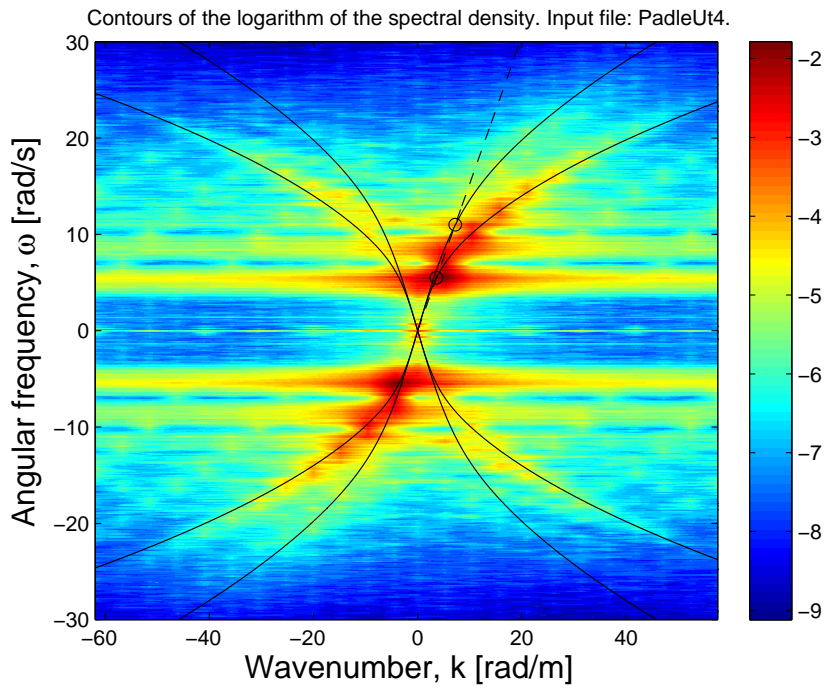


Figure 89: Logarithmic (k, ω) -spectra measured from series 4.

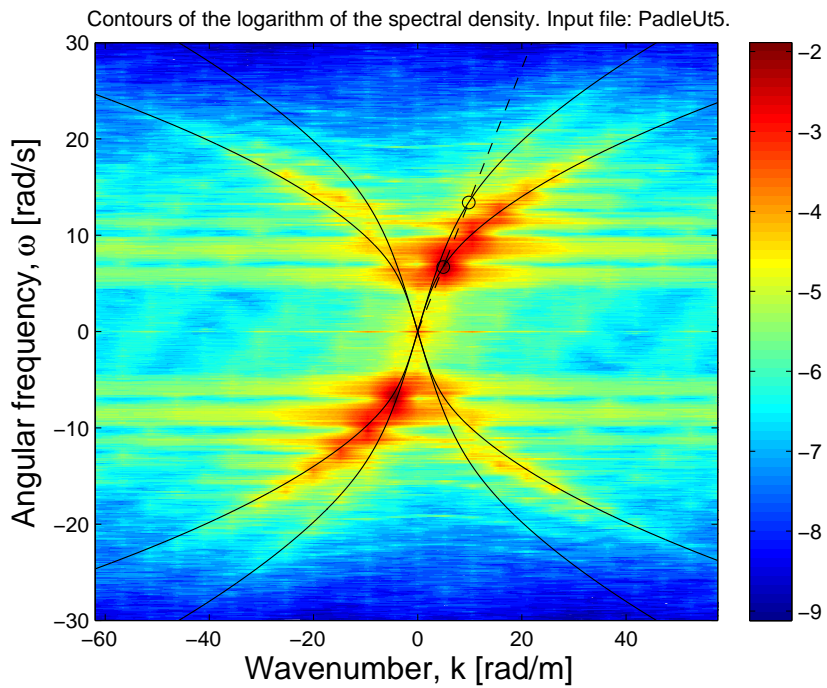


Figure 90: Logarithmic (k, ω) -spectra measured from series 5.

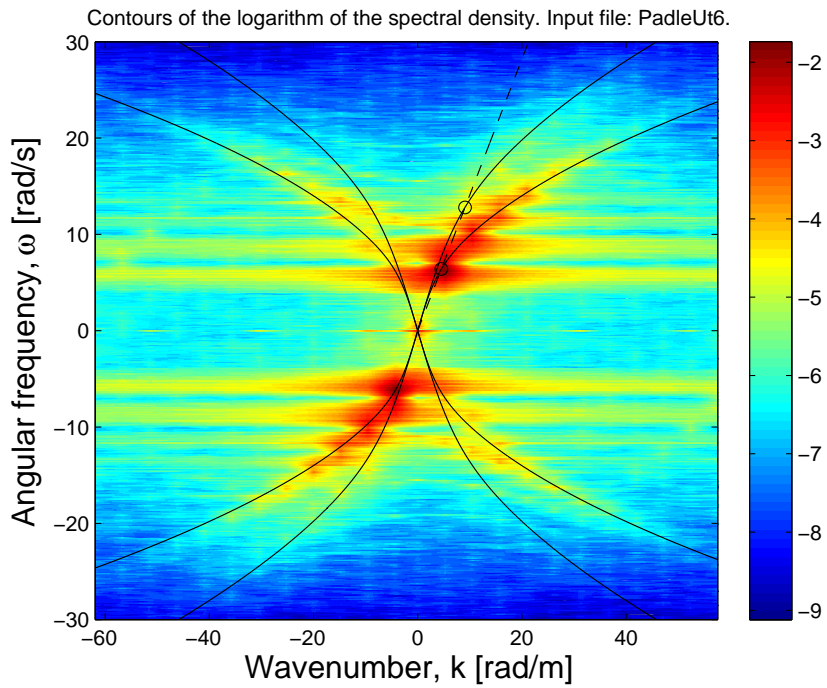


Figure 91: Logarithmic (k, ω) -spectra measured from series 6.

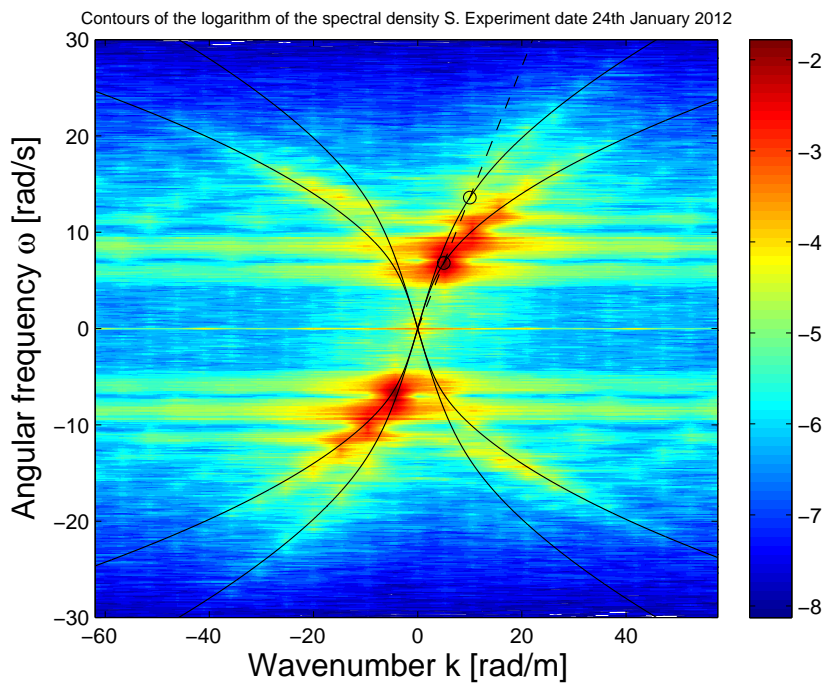


Figure 92: Logarithmic (k, ω) -spectra measured from the modified series 1.

E.1.2 The effect of space tapering in the (k, ω) -spectra

Different methods have been proposed for tapering in space. Since our space series only consists of 24 measurement points, conventional high resolution tapering methods may not be applicable since too few measurement points are represented for a gradual declination towards the end points.

Method 1

One space measurement with zeros is added after the other 24 measurements in space such that the last and the first measurements are closer to the declination position. After this the array is represented by 25 measurement points. The new length of the array is $L = 1.20 + 0.05 \text{ m} = 1.25 \text{ m}$. This also decreases Δk slightly, and gives a slightly better resolution along the wavenumber axis. The effect in the (k, ω) -spectrum is shown in figure 93.

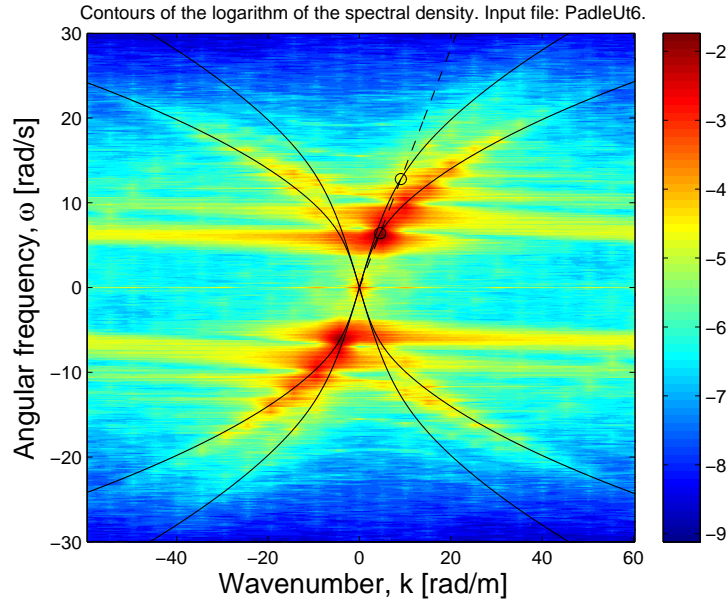


Figure 93: Method 1.

Method 2

In addition to adding a zero at the end of each space series, the first and the last surface elevation measurements are multiplied with $1/2$ in order to hopefully gain a more gradual declination towards zero. The 25 measurement positions are then represented by,

$$\left[\frac{1}{2} \eta_{0,n} \quad \eta_{1,n} \quad \eta_{2,n} \quad \dots \quad \eta_{21,n} \quad \eta_{22,n} \quad \frac{1}{2} \eta_{23,n} \quad \mathbf{0} \right]$$

The effect in the (k, ω) -spectrum is shown in figure 94.

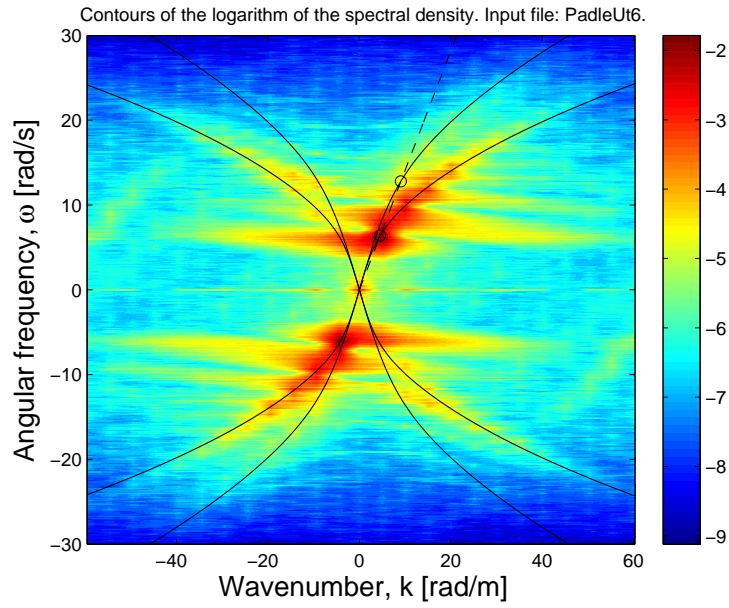


Figure 94: Method 2.

Method 3

Additional proposed method:

$$\left[\frac{1}{4}\eta_{0,n} \quad \frac{1}{2}\eta_{1,n} \quad \frac{3}{4}\eta_{2,n} \quad \eta_{3,n} \quad \dots \quad \eta_{20,n} \quad \frac{3}{4}\eta_{21,n} \quad \frac{1}{2}\eta_{22,n} \quad \frac{1}{4}\eta_{23,n} \quad \mathbf{0} \right]$$

The effect in the (k, ω) -spectrum is shown in figure 95.

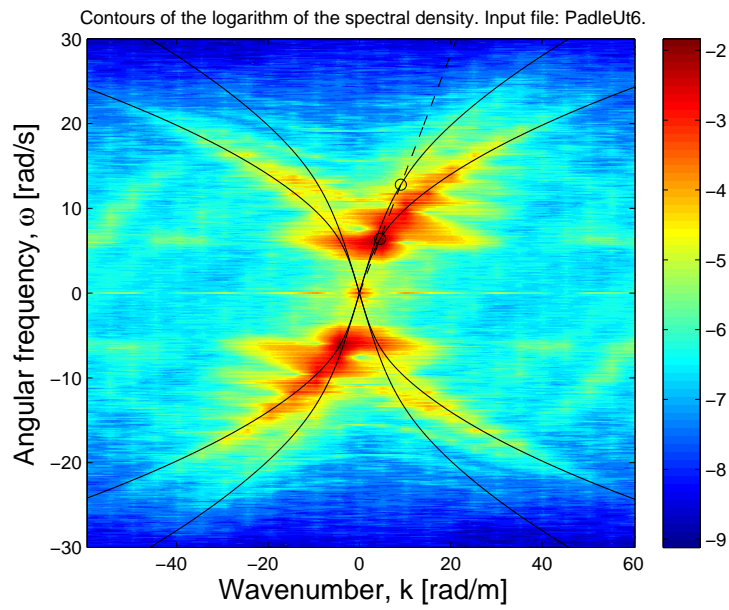


Figure 95: Method 3.

Method 4

Additional proposed method:

$$\left[\frac{1}{5}\eta_{0,n} \quad \frac{2}{5}\eta_{1,n} \quad \frac{3}{5}\eta_{2,n} \quad \frac{4}{5}\eta_{3,n} \quad \eta_{4,n} \quad \dots \quad \eta_{19,n} \quad \frac{4}{5}\eta_{20,n} \quad \frac{3}{5}\eta_{21,n} \quad \frac{2}{5}\eta_{22,n} \quad \frac{1}{5}\eta_{23,n} \quad \mathbf{0} \right]$$

The effect in the (k, ω) -spectrum is shown in figure 96.

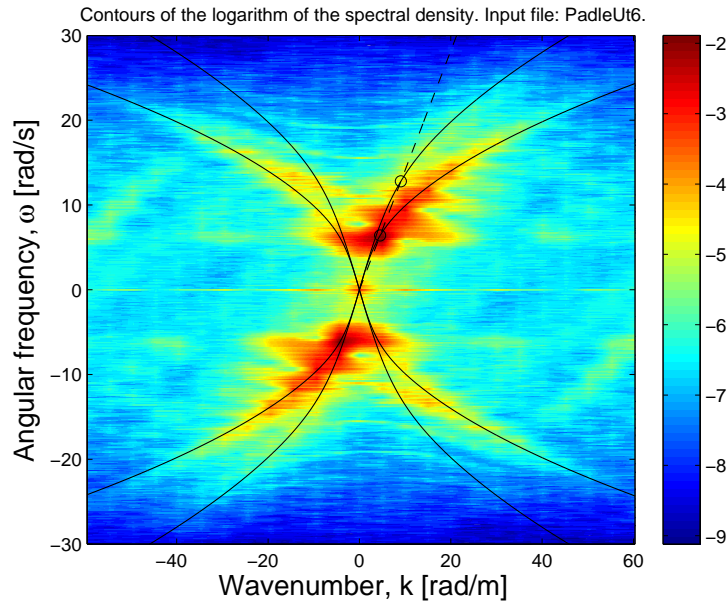


Figure 96: Method 4.

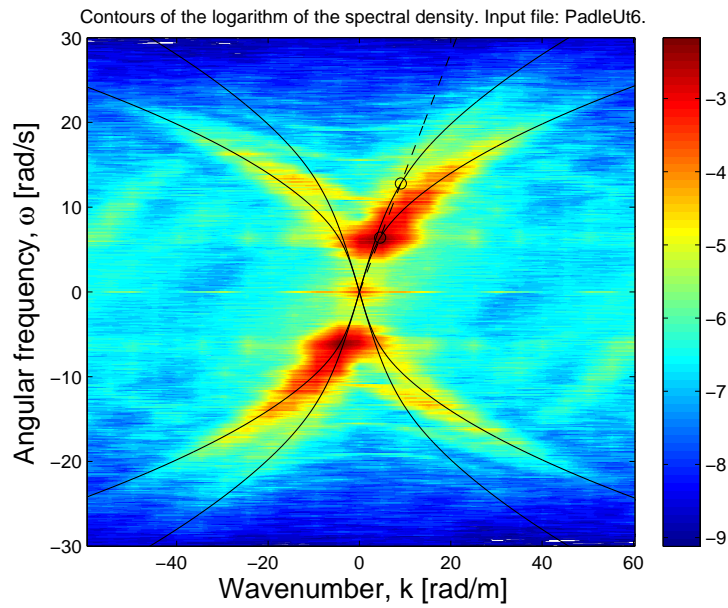


Figure 97: Method 5.

Method 5

Additional proposed method:

$$\left[\frac{1}{10}\eta_{0,n} \quad \frac{2}{10}\eta_{1,n} \quad \frac{3}{10}\eta_{2,n} \quad \frac{4}{10}\eta_{3,n} \quad \frac{5}{10}\eta_{4,n} \quad \frac{6}{10}\eta_{5,n} \quad \frac{7}{10}\eta_{6,n} \quad \frac{8}{10}\eta_{7,n} \quad \frac{9}{10}\eta_{8,n} \quad \eta_{9,n} \right. \\ \left. \dots \quad \eta_{14,n} \quad \frac{9}{10}\eta_{13,n} \quad \frac{8}{10}\eta_{16,n} \quad \frac{7}{10}\eta_{17,n} \quad \frac{6}{10}\eta_{18,n} \quad \frac{5}{10}\eta_{19,n} \quad \frac{4}{10}\eta_{20,n} \quad \frac{3}{10}\eta_{21,n} \quad \frac{2}{10}\eta_{22,n} \quad \frac{1}{10}\eta_{23,n} \quad \mathbf{0} \right]$$

The effect in the (k, ω) -spectrum is shown in figure 97.

Method 2, 3, 4 and 5 are similar to multiplying the space series with a tapering function based on a triangle window. Method 3, 4 and 5 might exaggerate the modification of the original data.

E.2 $L = 4.8$ m and $M = 96$

E.2.1 The entire (k, ω) -domain

Figure 98 shows the entire (k, ω) -domain for the contour plot in figure 47 in subsection 7.1.2, with 5 more contour levels than in figure 47. \circ is the peak point (k_p, ω_p) .

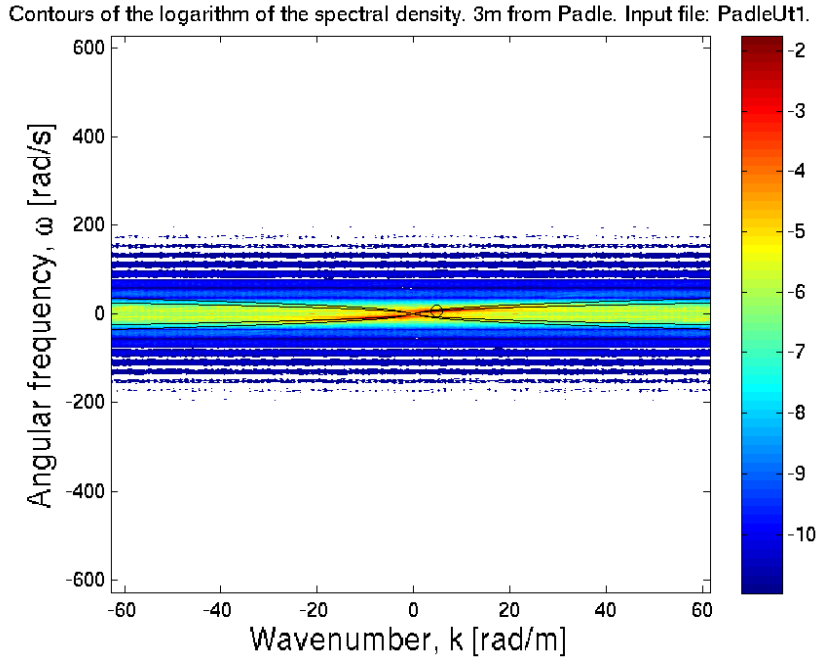


Figure 98: The whole (k, ω) -domain.

In figure 47 in subsection 7.1.2, the spectral energy density is plotted on 50 contour levels. Figure 98 shows the entire discretized (k, ω) -domain with $k \approx [-k_{M/2}, k_{M/2}] \text{ radm}^{-1}$, and $\omega \approx [-\omega_{N/2}, \omega_{N/2}] \text{ rads}^{-1}$, where $k_{M/2} \approx 61 \text{ radm}^{-1}$ is the Nyquist wavenumber and $\omega_{N/2} \approx 628 \text{ rads}^{-1}$ is the Nyquist angular frequency. Figure 99 is similar to figure 98 with $\omega = [-200, 200] \text{ rads}^{-1}$. As mentioned in subsection 7.1.1 the contour levels are defined on a self composed logarithmic scale which is based on only the scalar values around the maximum of $\log_{10} S(k, \omega)$ to reduce the CPU-time significantly. The CPU-time for producing each of the figures 98 and 99 is 2 hours and 52 minutes on a stationary computer at the University. The defined contour levels for the scalar values of $\log_{10} S(k, \omega) \approx [-2, -11]$ are plotted in figure 98 and 99. However if all the scalar values

for $\log_{10} S(k, \omega) \approx [-2, -21]$ would have been plotted, the CPU-time would increase significantly to the duration of days, and the domain around the peak would be dominated by red and orange colours. By reducing the amount of contour levels the peak intensities are easier to distinguish from the rest of the field, and as mentioned the CPU-time is reduced significantly.

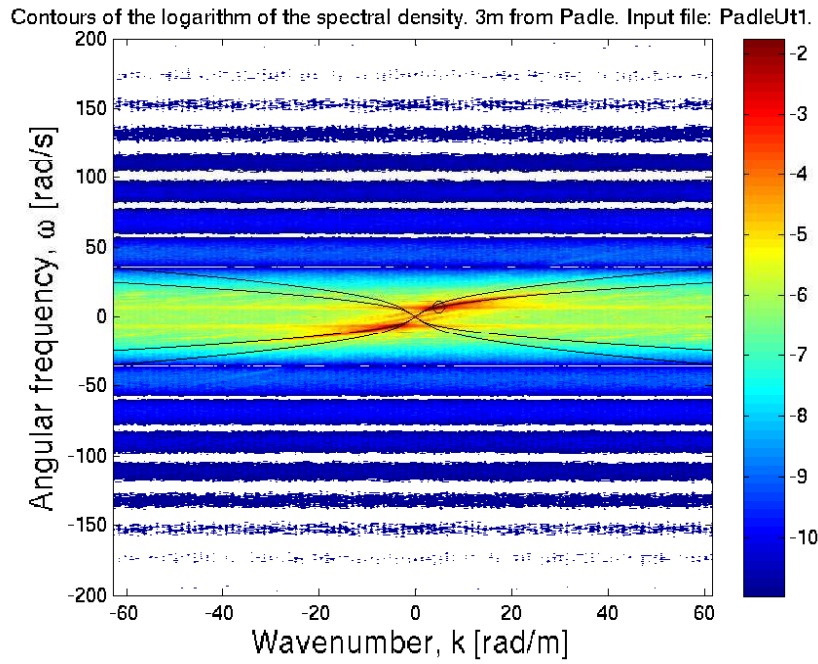


Figure 99: Parts of the whole (k, ω) -domain.

Figure 98 and 99 also shows that there is a periodicity in the spectral energy density distribution of the experimental data, and that local maxima of the spectral energy densities are distributed along horizontal lines in the (k, ω) -domain.

E.2.2 The effect of time tapering in the (k, ω) -spectra

Figure 100 and 101 shows the effect of tapering in space for the (k, ω) -spectrum in figure 47 subsection 7.1.2 when $N = 100$ elements at each end of the time series have been modified by the time tapering function as presented in section 5.5. The number of contour levels have been reduced as explained in the previous section. Figure 100 shows that the spectral leakage is most pronounced on the outer boundary of the plotted contour levels in the (k, ω) -spectra. The time tapering does not seem to affect the spectral distribution around the peak \circ significantly.

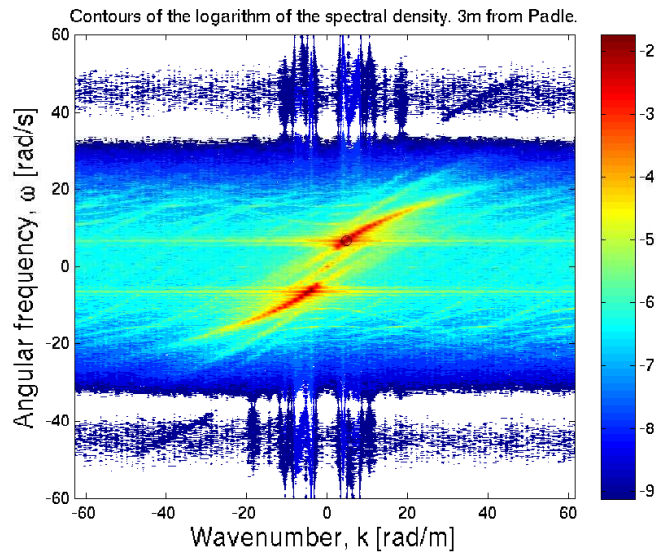


Figure 100: Without time tapering

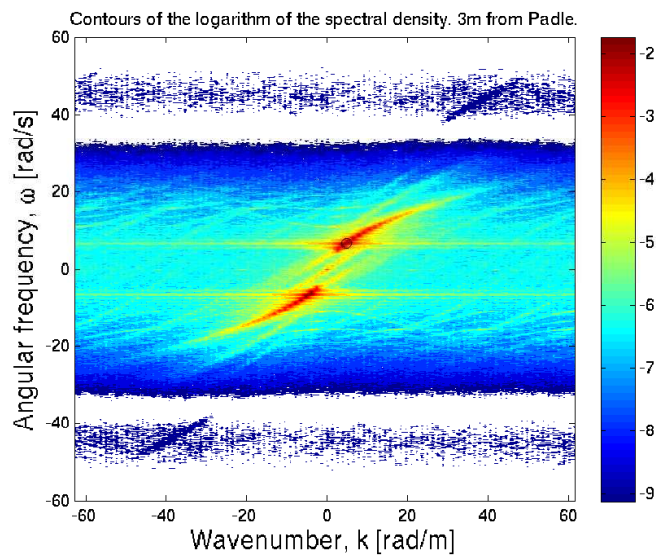


Figure 101: $N = 200$ elements time tapered

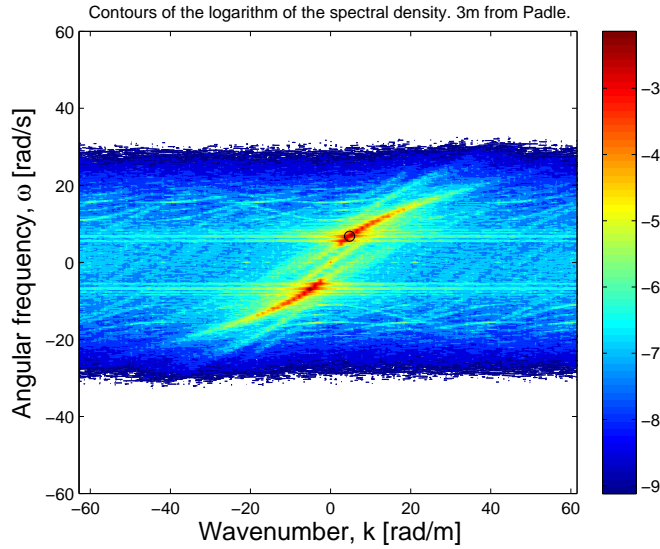


Figure 102: $N = 26000$ elements time tapered

Figure 102 shows the spectra when $N = 26000$ elements at each end of the time series have been modified by the time tapering function. This corresponds to multiplying the entire time series with the bell-shaped Nuttall window. The spectral distribution around the peak is affected and the horizontal distributions on the outer boundary are diminished.

E.2.3 The effect of space tapering in the (k, ω) -spectra

The (k, ω) -spectra in this section shows the effect of tapering in space for the (k, ω) -spectrum in figure 47 in subsection 7.1.2 by adding a zero to the end of the $M = 96$ element space series and by applying different end widths of the Nuttall window in the tapering function presented in section 5.6. Figure 103 shows the (k, ω) -spectrum (figure 47) without space tapering. In figure 104 a zero is added to the end of the space series.

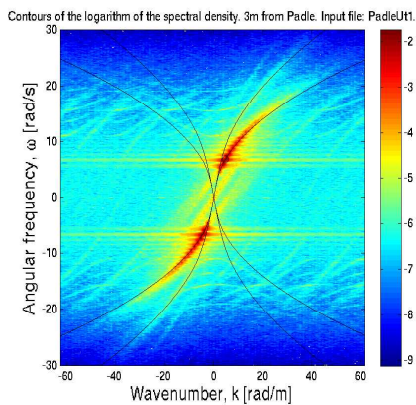


Figure 103: Without space tapering.

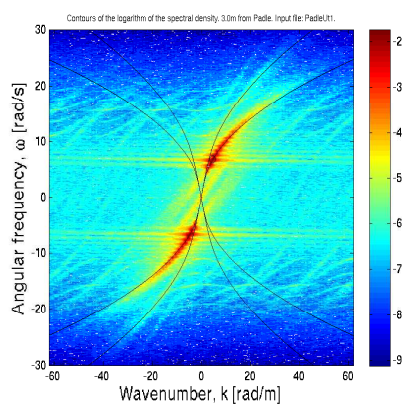


Figure 104: Zero added to the end of the space series.

In figure 105 a zero is added to the end of the space series. In addition: the first and the last element in the space series are multiplied by 0.5292 which instead of 0.5000 is a value which is generated from the Nuttall window. In figure 106 a zero is added to the

end of the space series. In addition: the first, second, second last, and the last element in the space series are multiplied by 0.1105, 0.7983, 0.7983, and 0.1105 respectively. The values are generated from the Nuttall window.

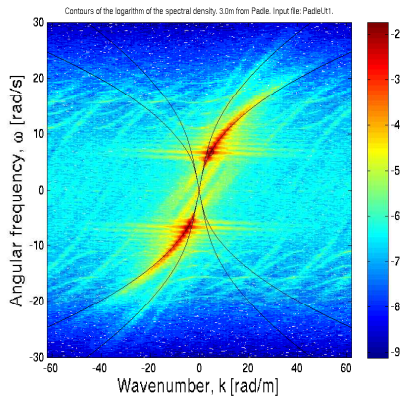


Figure 105: End width: one element.

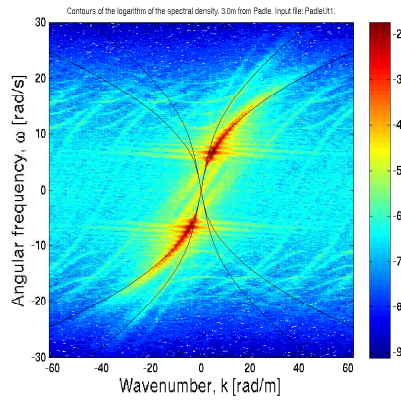


Figure 106: End width: two elements.

In figure 107 a zero is added to the end of the space series. In addition: the first, second, third, third last, second last, and the last element in the space series are multiplied by values generated from the Nuttall window. In figure 108 four elements at each end of the space series are modified by the tapering function based on the Nuttall window.

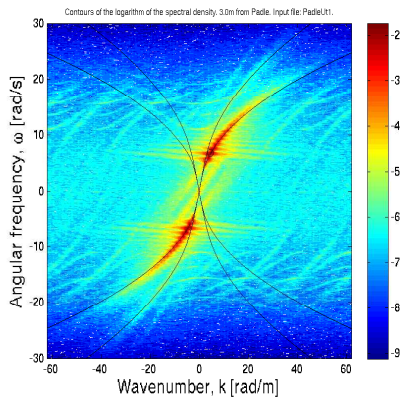


Figure 107: End width: three elements.

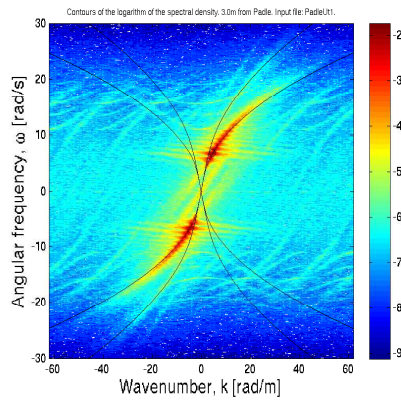


Figure 108: End width: four elements.

In figure 109 five elements at each end of the space series are modified by the tapering function based on the Nuttall window. In figure 110 six elements at each end of the space series are modified.

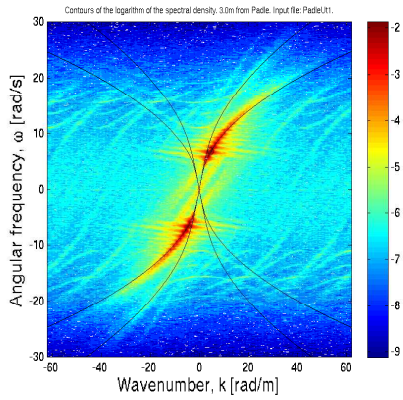


Figure 109: End width: five elements.

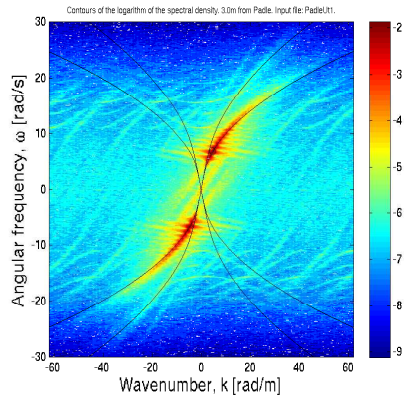


Figure 110: End width: six elements.

In figure 111 seven elements at each end of the space series are modified. In figure 112, eight elements at each end of the space series are modified.

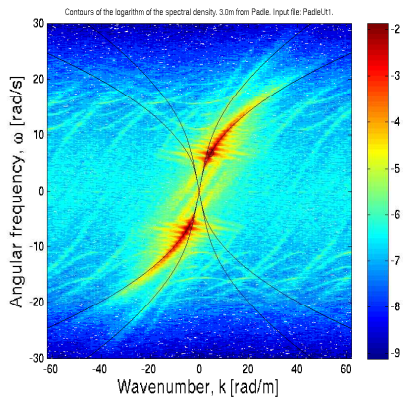


Figure 111: End width: seven elements.

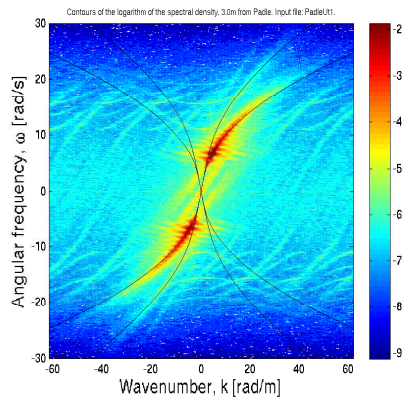


Figure 112: End width: eight elements.

In figure 113 nine elements at each end of the space series are modified. In figure 114 twenty elements at each end of the space series are modified.

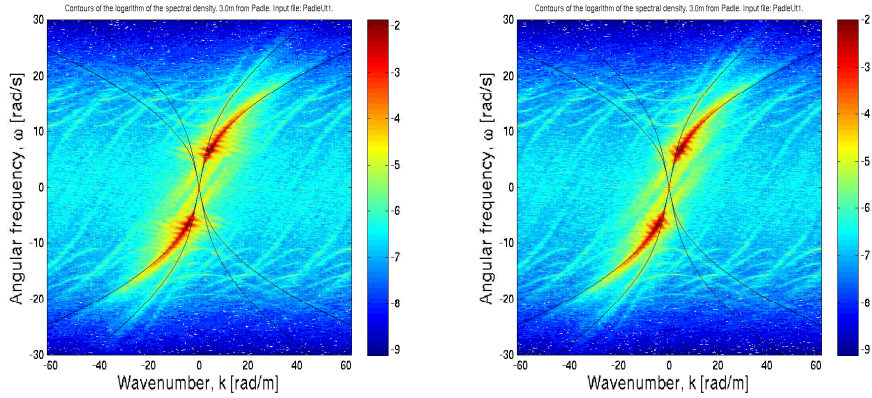


Figure 113: End width: nine elements. **Figure 114:** End width: twenty elements.

In figure 115 thirty elements at each end of the space series are modified.

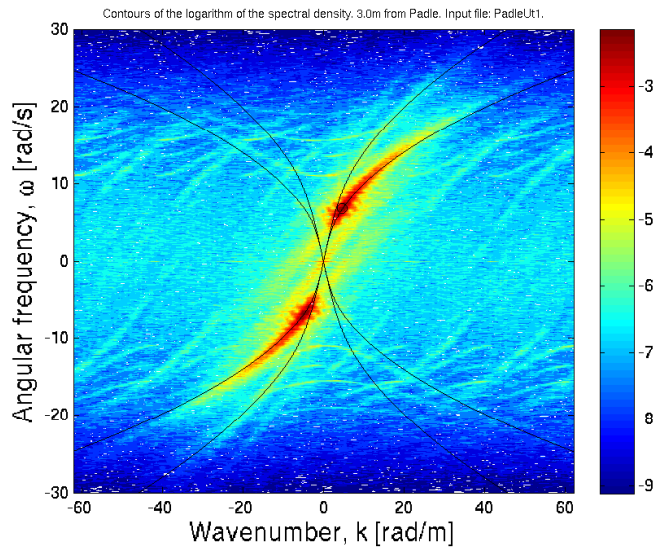


Figure 115: End width: thirty elements.

The space tapering in figure 115 might exaggerate the modification of the original data. Our strategi for the space tapering was to affect the original spectral energy density distribution as little as possible, and we chose to apply the tapering function corresponding to figure 109 where only five elements at each end of the space series have been modified.

E.3 $L = 19.2$ m and $M = 256$

E.3.1 The effect of a strong filter

Figure 116 and 117 shows the effect when a strong Savitzky-Golay filter is used to filter the surface elevation data applied for the spectral estimates shown in figure 53 and 61 in subsections 7.1.5 and 7.2.2. For the surface elevation the strong filter reduces the amplitudes of the waves but does not seem to affect the angular frequency distribution and the wave phases. Thus, the strong filter in practice reduces the magnitude of the spectral energy density in the spectra but does not affect the spectral energy density distribution.

With this example we intend to demonstrate that the relatively weak filter applied for the experimental data probably does not alter the spectral energy density distributions in the spectra significantly.

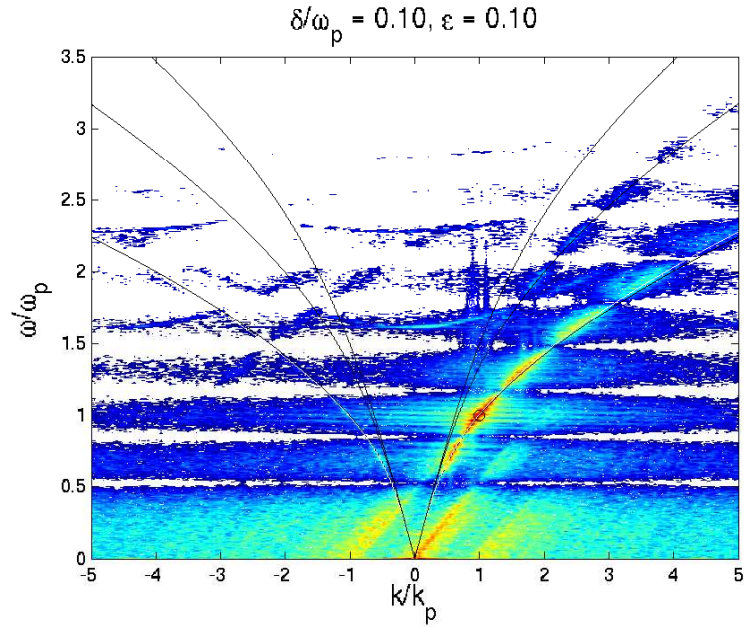


Figure 116: $L = 19.2$ m and $M = 256$. Strong filter applied.

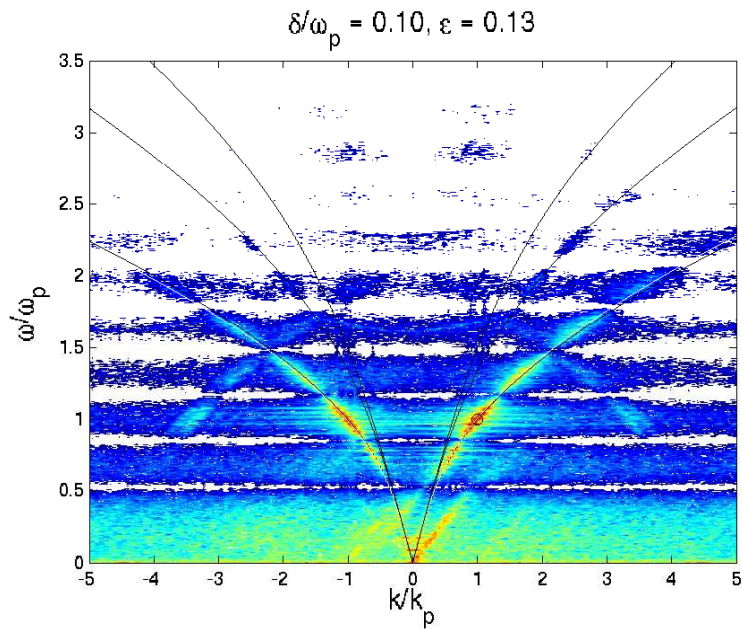


Figure 117: Reflecting wall. $L = 19.2$ m and $M = 256$. Strong filter applied.

List of Figures

1	Early stage experimental arrangement.	12
2	A stationary array and synthesis of a more dense array.	14
3	Later stage experimental arrangement.	15
4	The linear array, wave generator (end) and the wave field.	16
5	ADCP in horizontal position and bottom rack.	16
6	Example of an array with $M = 4$ elements.	18
7	Raw data.	23
8	Cubic interpolation.	23
9	Linear, cubic and spline interpolations.	24
10	Without filter.	25
11	With a Savitzky-Golay smoothing filter.	25
12	Startup waves.	26
13	Repeatability with absorbing beach.	27
14	With absorbing beach. Comparison with the raw data. P1 and P2.	28
15	With absorbing beach. Comparison with the raw data. P3 and P4.	28
16	Small difference in surface elevation measured by P4.	29
17	Repeatability with reflecting wall.	29
18	Measurement error by P1.	30
19	With reflecting wall. Comparison with the raw data. P1 and P2.	31
20	With reflecting wall. Comparison with the raw data. P3 and P4.	31
21	Blackman window.	32
22	Blackman-Harris window.	32
23	Nuttall window.	32
24	Illustration of the tapering function.	32
25	Actual tapering function applied to taper the time series.	32
26	Tapered start of $M = 96$ time series.	33
27	Tapered end of $M = 96$ time series.	33
28	The space tapering function.	34
29	Linear frequency spectrum with absorbing beach.	35
30	Linear frequency spectrum with reflecting wall.	35
31	Logarithmic frequency spectrum with absorbing beach.	35
32	Logarithmic frequency spectrum with reflecting wall.	35
33	Bandwidth from series 1 with absorbing beach.	37
34	Bandwidth from series 1 with reflecting wall.	38
35	Linear wavenumber spectrum with absorbing beach.	38
36	Linear wavenumber spectrum with reflecting wall.	38
37	Time series of u at $z = -52.5$ cm. With absorbing beach.	43
38	Arithmetic means of the mean speeds $\langle u \rangle$	44
39	Arithmetic means of the standard deviations $\langle \sigma \rangle$	45
40	Time series of u at $z = -52.5$ cm. With reflecting wall.	46
41	Arithmetic means of mean speeds $\langle u \rangle$	47
42	Arithmetic means of the standard deviations $\langle \sigma \rangle$	47
43	Linear (k, ω) -spectrum. $L = 1.2$ m and $M = 24$	50
44	Logarithmic (k, ω) -spectrum. $L = 1.2$ m and $M = 24$	50
45	Large interpolation error after 311 s of wave generation in series 2.	52
46	Absorbing beach at $h = 0.60$ m.	52
47	(k, ω) -spectrum. $L = 4.8$ m and $M = 96$. $D = 3.0$ m.	53
48	(k, ω) -spectrum. $L = 4.8$ m and $M = 96$. $D = 8.1$ m.	54
49	(k, ω) -spectrum. $L = 4.8$ m and $M = 96$. $D = 15.2$ m.	54
50	(k, ω) -spectrum. $L = 9.6$ m and $M = 192$. $u = 2$ cm/s.	56
51	Large interpolation errors. $L = 9.6$ m and $M = 192$	57
52	(k, ω) -spectrum. $L = 19.2$ m and $M = 128$. $u = 2$ cm/s.	58
53	(k, ω) -spectrum. $L = 19.2$ m and $M = 256$. $u = 1$ cm/s.	59
54	Reflecting beach.	61
55	(k, ω) -spectrum. Reflecting beach. $L = 4.8$ m and $M = 96$. $D = 3.0$ m.	61
56	(k, ω) -spectrum. Reflecting beach. $L = 4.8$ m and $M = 96$. $D = 8.1$ m.	62
57	(k, ω) -spectrum. Reflecting beach. $L = 4.8$ m and $M = 96$. $D = 15.2$ m.	62

58	Repetition errors in experiment at $D = 3.0$ m with reflecting beach.	63
59	Reflecting wall.	64
60	(k, ω) -spectrum. Reflecting wall. $L = 4.8$ m and $M = 96$. $D = 8.1$ m.	64
61	(k, ω) -spectrum. Reflecting wall. $L = 19.2$ m and $M = 256$. $u = 1$ cm/s.	66
62	No errors in Δx introduced.	69
63	3 mm error in Δx between the 1st and 2nd probe.	70
64	3 mm error in Δx between the 4th and 5th probe.	70
65	3 mm error in Δx between the 8th and 9th probe.	71
66	3 mm error in Δx between the 12th and 13th probe.	71
67	3 mm error in Δx between the measurement sub-procedures.	72
68	Calibration curve.	82
69	Linear frequency spectrum from series 1.	83
70	Logarithmic frequency spectrum from series 1.	83
71	Linear frequency spectrum from series 2.	84
72	Logarithmic frequency spectrum from series 2.	84
73	Linear frequency spectrum from series 3.	84
74	Logarithmic frequency spectrum from series 3.	84
75	Linear frequency spectrum from series 4.	84
76	Logarithmic frequency spectrum from series 4.	84
77	Linear frequency spectrum from series 5.	85
78	Logarithmic frequency spectrum from series 5.	85
79	Linear frequency spectrum from series 6.	85
80	Logarithmic frequency spectrum from series 6.	85
81	Series 1.	86
82	Series 2.	86
83	Series 3.	86
84	Series 4.	86
85	Series 5.	86
86	Series 6.	86
87	Logarithmic (k, ω) -spectra measured from series 2.	87
88	Logarithmic (k, ω) -spectra measured from series 3.	87
89	Logarithmic (k, ω) -spectra measured from series 4.	88
90	Logarithmic (k, ω) -spectra measured from series 5.	88
91	Logarithmic (k, ω) -spectra measured from series 6.	89
92	Logarithmic (k, ω) -spectra measured from the modified series 1.	89
93	Method 1.	90
94	Method 2.	91
95	Method 3.	91
96	Method 4.	92
97	Method 5.	92
98	The whole (k, ω) -domain.	93
99	Parts of the whole (k, ω) -domain.	94
100	Without time tapering	95
101	$N = 200$ elements time tapered	95
102	$N = 26000$ elements time tapered	96
103	Without space tapering.	96
104	Zero added to the end of the space series.	96
105	End width: one element.	97
106	End width: two elements.	97
107	End width: three elements.	97
108	End width: four elements.	97
109	End width: five elements.	98
110	End width: six elements.	98
111	End width: seven elements.	98
112	End width: eight elements.	98
113	End width: nine elements.	99
114	End width: twenty elements.	99
115	End width: thirty elements.	99

116	$L = 19.2$ m and $M = 256$. Strong filter applied.	100
117	Reflecting wall. $L = 19.2$ m and $M = 256$. Strong filter applied.	100

List of Tables

1	Repetition errors with absorbing beach.	27
2	Repetition errors with reflecting wall.	30
3	ω_p and k_p with absorbing beach.	36
4	δ and δ^* with absorbing beach.	37
5	a_c and ϵ with absorbing beach.	39
6	a_c and ϵ with reflecting wall.	39
7	Table of parameters for ϵ/δ^*	40
8	Arithmetic means of \bar{u} and σ . With absorbing beach.	44
9	Arithmetic means of \bar{u} and σ	46
10	Repetition errors. $L = 1.2$ m and $M = 24$	51
11	a_c and ϵ at $D = 3.0, 8.1$ and 15.2 m.	55
12	Repetition errors. $L = 4.8$ m and $M = 96$. With absorbing beach.	55
13	Repetition errors. $L = 9.6$ m and $M = 192$	56
14	Repetition errors. $L = 9.6$ m and $M = 192$	58
15	Repetition errors. $L = 19.2$ m and $M = 256$. Absorbing beach.	60
16	a_c and ϵ with reflecting beach.	63
17	Repetition errors. $L = 4.8$ m and $M = 96$. Reflecting beach.	63
18	a_c and ϵ with reflecting beach.	65
19	a_c and ϵ with reflecting wall.	65
20	Repetition errors. $L = 4.8$ m and $M = 96$. Reflecting wall.	65
21	Repetition errors. $L = 19.2$ m and $M = 256$. Reflecting wall.	67
22	Input file velocities and accelerations.	81